LIVING NANOCRYSTALS: SYNTHESIS OF PRECISELY DEFINED METAL OXIDE NANOCRYSTALS THROUGH A CONTINUOUS GROWTH PROCESS

by

ADAM WAYNE JANSONS

A DISSERTATION

Presented to the Department of Chemistry and Biochemistry
and the Graduate School of the University of Oregon
in partial fulfillment of the requirements
for the degree of
Doctor of Philosophy

December 2017

DISSERTATION APPROVAL PAGE

Student: Adam Wayne Jansons

Title: Living Nanocrystals: Synthesis of Precisely Defined Metal Oxide Nanocrystals Through a Continuous Growth Process

This dissertation has been accepted and approved in partial fulfillment of the requirements for the Doctor of Philosophy degree in the Department of Chemistry and Biochemistry by:

Darren W. Johnson	Chairperson
James E. Hutchison	Advisor
Shannon W. Boettcher	Core Member
Benjamin J. McMorran	Institutional Representative

and

Sara D. Hodges	Interim Vice Provost and Dean of the Graduate School

Original approval signatures are on file with the University of Oregon Graduate School.

Degree awarded December 2017

DISSERTATION ABSTRACT

Adam Wayne Jansons

Doctor of Philosophy

Department of Chemistry and Biochemistry

December 2017

Title: Living Nanocrystals: Synthesis of Precisely Define Metal Oxide Nanocrystals Through a Continuous Growth Process

Colloidal nanocrystals offer new and improved performance in applications as well as less environmental impact when compared to traditional device fabrication methods. The important properties that enable improved applications are a direct result of nanocrystal structure. While there have been many great advances in the production of colloidal nanocrystals over the past three decades, precise, atomic-level control of the size, composition, and structure of the inorganic core remains challenging. Rather than dictate these material aspects through traditional synthetic routes, this dissertation details the development and exploitation of a colloidal nanocrystal synthetic method inspired by polymerization reactions. Living polymerization reactions offer precise control of polymer size and structure and have tremendously advanced polymer science, allowing the intuitive production of polymers and block co-polymers of well-defined molecular weights. Similarly, living nanocrystal synthetic methods allow an enhanced level of structural control, granting the synthesis of binary, doped, and core/shell nanocrystals of well-defined size, composition, and structure. This improved control in turn grants enhanced nanocrystal property performance and deepens our understanding of structure/property relationships.

This dissertation defines living nanocrystal growth and demonstrates the potential of the living methods in the colloidal production of oxide nanocrystals. After a brief introduction, living growth is defined and discussed in the context of synthetic prerequisites, attributes, and outcomes. Living growth is also compared to more traditional colloidal nanocrystal synthetic methods. The following chapters then demonstrate the precise control living approaches offer in three separate studies; the first highlights sub-nanometer control of nanocrystal size from 2-22+ nm in diameter. Next the improvement in nanocrystal composition is illustrated using several transition metal dopants into an oxide nanocrystal matrix at near thermodynamically allowed compositions. Additionally, precise radial dopant placement is demonstrated, which has striking implications for material properties. The radial position of tin in tin-doped indium oxide nanocrystals and the resulting differences on the localized surface plasmon resonance are discussed. Finally, future opportunities are reviewed.

This dissertation includes previously published and unpublished co-authored material.

CURRICULUM VITAE

NAME OF AUTHOR: Adam Wayne Jansons

GRADUATE AND UNDERGRADUATE SCHOOLS ATTENDED:

University of Oregon, Eugene, OR
Western Washington University, Bellingham, WA

DEGREES AWARDED:

Doctor of Philosophy, Chemistry, 2017, University of Oregon
Master of Science, Chemistry, 2013, University of Oregon
Bachelor of Science, Chemistry, 2011, Western Washington University

AREAS OF SPECIAL INTEREST:

Materials Science
Nanomaterial Synthesis: Colloidal Nanocrystal Synthesis
Nanomaterial Characterization
Surface Characterization
Green Chemistry

PROFESSIONAL EXPERIENCE:

Graduate Research Assistant, Department of Chemistry, University of Oregon, 2012-2017

Graduate Teaching Assistant, Department of Chemistry, University of Oregon, 2012-2013

Production Associate, Thermo Fisher Scientific, Lafayette, CO, 2011-2012

Materials Intern, Infinite Power Solutions, Littleton, CO, 2009-2010

GRANTS, AWARDS, AND HONORS:

Julie and Rocky Dixon Graduate Student Innovation Award, The Graduate School, University of Oregon, 2016-2017

Eagle Scout, Boy Scouts of America, 2006

PUBLICATIONS:

Jansons, A. W.; Koskela, K. M.; Crockett, B. M.; Hutchison, J. E. Transition Metal-Doped Metal Oxide Nanocrystals: Efficient Substitutional Doping Through a Continuous Growth Process. *Chem. Mater.* **2017**, *29* (19), 8167–8176.

Crockett, B. M.; Jansons, A. W.; Koskela, K. M.; Johnson, D. W.; Hutchison, J. E. Radial Dopant Placement for Tuning Plasmonic Properties in Metal Oxide Nanocrystals. *ACS Nano* **2017**, *11* (8), 7719–7728.

Jansons, A. W.; Plummer, L. K.; Hutchison, J. E. Living Nanocrystals. *Chem. Mater.* **2017**, *29* (13), 5415–5425.

Jansons, A. W.; Hutchison, J. E. Continuous Growth of Metal Oxide Nanocrystals: Enhanced Control of Nanocrystal Size and Radial Dopant Distribution. *ACS Nano* **2016**, *10* (7), 6942–6951.

Merrill, D. R.; Moore, D. B.; Coffey, M. N.; Jansons, A. W.; Falmbigl, M.; Johnson, D. C. Synthesis and Characterization of Turbostratically Disordered $(BiSe)_{1.15}$ $TiSe_2$. *Semicond. Sci. Technol.* **2014**, *29* (6), 064004.

ACKNOWLEDGMENTS

I would like to first thank my advisor, Dr. Jim Hutchison for the opportunity to study in his lab, his scientific guidance, and for sharing his passions for science, beer, running, and the outdoors. During my time in graduate school not only have I have studied an immense amount of chemistry with his direction, but I have also learned much more about logically handling obstacles, motivating and managing people, and strategically working toward preferred outcomes. I am very thankful for the experience, and for the support and time he gives his students.

I would also like to thank and acknowledge my thesis committee — Dr. Darren Johnson, Dr. Shannon Boettcher, and Dr. Ben McMorran — for their continued support during graduate school. They, along with many other faculty, keep the chemistry (and other physical science) departments at the University of Oregon producing excellent research while remaining human in their approach. I think this is one of the many reasons students choose to study at the U of O.

While my co-authors on the studies in this dissertation are acknowledged in various chapters, I would like to acknowledge and thank them here as well. I am extremely grateful to have worked closely with two excellent graduate students, Brandon Crockett and Kenyon Plummer. Both are not only gifted scientists, but are fun and kind people to work and hang out with. Thank you both. I would also like to acknowledge and thank undergraduate student Kris Koskela. Thank you Kris for being an extremely hard worker, and a fun guy. Best of luck on your future endeavors, grad school and beyond. And while not an author on any of the work presented here, I would also like to acknowledge the most recent undergraduate student I have had the pleasure of working with, Makenna Pennel. Thank you Makenna for your hard work and help.

I would like to thank previous members of the Hutchlab for their support, and for helping make the lab what it is today — Dr. Rick Glover, Dr. Pat Haben, Dr. Ed Elliott, Dr. Zack Kennedy, Dr. Bev Smith, and Dr. Brandi Baldock. And of course I would like to thank the current members — Dr. Tatiana Zaikova, Samantha Young, Susan Cooper, Kenyon Plummer, Brandon Crockett, Brantly Fulton, Meredith Sharps, Jaclyn Kellon, Aurora Ginzburg, and our newest member, Tawney Knecht — for helping each other, doing excellent science, and for being great friends. Thank you all.

Materials research at the U of O critically depends on help from all of the staff in CAMCOR, including Josh Razink, Dr. Steve Golledge, Kurt Langworthy, and Steve Wiemholt. I am extremely grateful for their assistance in completing this work. I would also like to acknowledge the staff of the machine and electronics shop for all of their assistance — including John Boosinger, Kris Johnson, Jeffrey Garman, and Cliff Dax — as well as the staff of Science Stores, including Jennifer Jess and Clive Kittredge. Additionally I would like to acknowledge funding sources, including the National Science Foundation and the UO graduate school. CAMCOR is supported by grants from the W.M. Keck Foundation, M.J. Murdock Charitable Trust, ONAMI, the Air Force Research Laboratory, and the University of Oregon.

I would like to acknowledge my current and previous roommates, Luke Wheeler and Forrest Laskowski, for their support throughout grad school, and for making my experience more enjoyable. I would especially like to thank Luke and his family for housing me during these last several months.

I am not going to mention every graduate student who has assisted me with an experiment, helped analyze results, or been there with a beer after a hard day, because there are too many people to thank. The department, and especially the people that make up the materials research labs, have all been extremely helpful and kind to each other, and for that I am grateful. Thank you all for making this a good place to work.

I would like to thank both soccer teams, Specific Heat and Hot Rod, for keeping me active during stressful times, the beautiful nature of Oregon for providing so many great outdoor adventures, and the fine breweries in the state for providing places to celebrate success and defeat (I especially want to thank Brewers Union Local 180).

I want to thank Meredith Sharps and her family for their personal support, and thank Meri for being a great partner over the last 2+ years.

Lastly, and most important, I would like to thank my family for their continued love and constant support. My parents, John and Lynne, have always supported me and my endeavors often without much explanation from me. My sister and her family — Lauren, Aaron, Ethan, Felicity, and Sam — have brought me an immense amount of joy over the last 5 years. Thank you all, I truly would not be here without you.

To the teachers and mentors that dedicate their lives to helping others

TABLE OF CONTENTS

Chapter Page

Chapter Page

Chapter Page

LIST OF FIGURES

Figure Page

LIST OF TABLES

Table Page

LIST OF SCHEMES

Scheme Page

CHAPTER I

INTRODUCTION

Dissertation Introduction

Nanoparticles and nanocrystals hold promise as breakthrough materials for many exciting new applications because of their unique size-dependent properties. During the last several decades, new applications have been reported across nearly every technological sector, including human health,[1] electronics,[2,3] optics,[4,5] energy storage and production,[6] chemical catalysis,[7] and sensing.[8] New synthetic methods have been developed to gain access to nanomaterials needed for these applications, facilitating broader adoption.[9–17] Each new generation of applications demands higher performance nanomaterials, requiring more precise control over the structural features that dictate properties and performance – core size, composition, and surface chemistry. In many cases the pioneering synthetic methods used to discover new materials and applications don't offer the required level of precision. Thus, new applications drive the need for synthetic approaches that offer greater control of the atomic-scale structure and composition of the nanoparticle building blocks.

Some of the most transformative approaches to material synthesis are those that permit atomic level control over composition and structure. For example, vapor-phase synthetic

methods, e.g., atomic layer deposition and molecular beam epitaxy, achieve such resolution in the case of inorganic thin films.[18,19] Advances in vapor phase synthetic methods have afforded access to kinetically-stable compounds, in addition to traditional thermodynamically stable products, and greatly increased the number of structures and properties that can be obtained with a specific stoichiometry.[20,21] Such synthetic methods offer an invaluable approach to control the properties of solid-state materials for demanding applications. The same level of control in liquid phase colloids has been much slower to develop. Perhaps the two best liquid-phase examples from materials chemistry are biomineralization mechanisms[22] and polymerization reactions.[23]

There have been many advances in nanocrystal and nanoparticle synthesis during the last decade; however, most of the commonly employed synthetic methods offer far less structural control than the well-honed reactions employed for small molecule or polymer synthesis. Developing methods to synthesize nanomaterials with uniform core sizes and specific composition with intentionality and reproducibility will enable research on the interplay of size, composition, and structure, as well as facilitate the translation to commercial application. The challenge in gaining such control with colloidal nanocrystal syntheses is understandable and expected – a nanocrystal synthesis must manage the complexities of nucleation and growth in solution,[24] and is further burdened by size- and structure-dependent surface energies. One approach to addressing these challenges is to take inspiration from macromolecular strategies where precise synthetic methods have provided dramatically improved structural control.

The Hutchison group recently discovered a new synthetic method to produce metal oxide nanocrystals that is analogous to, and inspired by, living polymerization methods. It allows

unprecedented control over nanocrystal composition and structure. This dissertation discusses the concept of living nanocrystal growth and highlights how living approaches lead to enhanced control of core size, doped composition, and core/shell structure.

Dissertation Overview

Chapter II, and the first three paragraphs of this chapter, are from a Perspective recently published in Chemistry of Materials (Jansons, A. W.; Plummer, L. K.; Hutchison, J. E. Living Nanocrystals. *Chem. Mater.* **2017**, *29* (13), 5415–5425). Chapter II defines living growth for nanocrystals, compares living nanocrystal growth to living polymerization reactions, and outlines specific chemical prerequisites and synthetic attributes and outcomes for living growth. Additionally, living approaches are compared to other nanocrystal syntheses recently published in the literature, with an emphasis comparing living growth to more traditional seeded growth methods. Implications for the living synthesis of core/shell nanocrystals are discussed, and the chapter wraps up by highlighting future challenges critical to advancing our understanding of nanocrystal formation and monomer addition in these synthetic methods. The paper was conceptualized and written by myself, Kenyon Plummer, and Jim Hutchison. Figures were made by Kenyon Plummer and myself. The data briefly discussed in the chapter are expanded upon in subsequent chapters.

Chapter III demonstrates the unprecedented control over the inorganic core size possible with metal oxide nanocrystals using living growth approaches (previously published as Jansons, A. W.; Hutchison, J. E. Continuous Growth of Metal Oxide Nanocrystals: Enhanced Control of Nanocrystal Size and Radial Dopant Distribution. *ACS Nano* **2016**, *10* (7), 6942–6951). Using the slow addition of metal carboxylates into oleyl alcohol and

employing In_2O_3 nanocrystals as a model system, we utilized small-angle X-ray scattering (SAXS) and transmission electron microscopy (TEM) to study the oxide nanocrystal core size, size dispersity, and concentration as a function of metal precursor addition. We found that growth of the nanocrystals proceeds with little coalescence or ripening, and show that core size can be controlled with sub-nanometer precision over a range of 2-30+ nm. The nanocrystal core volume (and thus core molecular weight) increases linearly as a function of metal precursor addition. Growth can be stopped and started without passivation. These findings suggested strong parallels with living growth, because several synthetic attributes are consistent with living polymerization. I performed the experiments, and the article was conceived and written by Jim Hutchison and me.

Living growth approaches are not only advantageous for nanocrystal size control, but also precise control of composition. Chapter IV highlights the impressive control over doped oxide nanocrystal composition that is possible when slow, living growth approaches are utilized. We show that, for incorporation of a wide variety of first row transition metal dopants into an oxide matrix, dopant concentration can be precisely controlled through the slow addition of a mixed metal precursor. Final dopant concentrations in the nanocrystal match that of the mixed precursor, most metal dopants incorporate with > 90% efficacy, and the dopants are evenly distributed throughout the nanocrystal. Producing doped nanocrystals with precise composition and size without significant investment into synthetic optimization, as is possible with living growth, greatly aids in our ability to utilize the important properties of nanocrystals, and better understand their unique properties. The chapter is reprinted from a recently published article in Chemistry of Materials (Jansons, A. W.; Koskela, K. M.; Crockett, B. M.; Hutchison, J. E. Transition Metal-Doped Metal

Oxide Nanocrystals: Efficient Substitutional Doping Through a Continuous Growth Process. *Chem. Mater*. **2017**, *29* (19), 8167–8176.**)**. Experiments were performed by Kristopher Koskela, Brandon Crockett, and me. All four co-authors wrote the paper.

Important properties of nanocrystals not only depend on composition, but also on structure. Chapter V demonstrates the striking influence that the radial placement of dopants in doped oxide nanocrystals has on optical properties, namely the localized surface plasmon resonance (LSPR). LSPRs arise in heterovalently doped oxide nanocrystals due to the free electrons donated by the dopant atom. Living growth synthetic methods allow the intuitive production of doped structure (as discussed in chapter IV) as well as core/shell structure. Through the appropriate choice and addition order of metal precursors, we show that the radial position of tin dopants in indium oxide nanocrystals has the potential to precisely sculpt optoelectronic properties, beyond that of traditional colloidal methods. Radial tin distribution has a profound influence on LSPR activation (the number of electrons donated per tin dopant atom) as well as LSPR damping (proportional to LSPR linewidth). The article was previously published in ACS Nano (Crockett, B. M.; Jansons, A. W.; Koskela, K. M.; Johnson, D. W.; Hutchison, J. E. Radial Dopant Placement for Tuning Plasmonic Properties in Metal Oxide Nanocrystals. *ACS Nano* **2017**, *11* (8), 7719–7728). Experiments were performed by Brandon Crockett, Kristopher Koskela, and me. The paper was written by Brandon Crockett, Jim Hutchison, Darren Johnson, and me.

Finally, chapter VI offers some concluding remarks regarding living nanocrystal growth, with an eye toward future opportunities. Portions of this chapter are reprinted from Jansons, A. W.; Plummer, L. K.; Hutchison, J. E. Living Nanocrystals. *Chem. Mater.* **2017**,

29 (13), 5415–5425. Copyright 2017. As already stated above, all three authors conceptualized and wrote the article.

The work presented in this dissertation is a small sampling of the core size, composition, and structural control possible via living growth approaches. While there is much to learn mechanistically that will aid in understanding the chemistry involved, many new nanocrystal structures and compositions can already be synthesized and await further study.

CHAPTER II

LIVING NANOCRYSTALS

This chapter was previoulsy published as Jansons, A. W.; Plummer, L. K.; Hutchison, J. E. Living Nanocrystals. *Chem. Mater.* **2017**, *29* (13), 5415–5425.

Living Synthetic Approaches to Macromolecules, including Nanocrystals

The discovery and development of living polymerization made it possible to control polymer structure and molecular weight and to understand how each of these influences physical properties, including viscosity, glass transition temperature, and osmotic pressure of polymer solutions.[1,2] Understanding these properties led to, among other things, the development of thermoplastics, non-leaking battery solvents, and an understanding of important biological phenomena.[2] Living growth approaches forever changed polymer science.[2,3]

In living polymerizations, the same number of polymer chains remain present during propagation (growth) steps, chains propagate at the same rate, and chains do not self-terminate (stay living), which allows for the simple production of advanced structures through the addition of a chemically different reactive monomer.[4] Irreversible chain addition reactions, which prevent monomers from detaching from existing chains and reactive sites that prevent random chain termination are also key features of living

polymerization.[2] An important hallmark of a living process is a linear correlation between the molecular weight of a polymer and the extent of monomer conversion—a phenomenon that allows predictable control of molecular weight with very fine resolution (**Figure 2.1**). Furthermore, monomer consumption is often near 100%, which contributes to the high level of predictability and control.

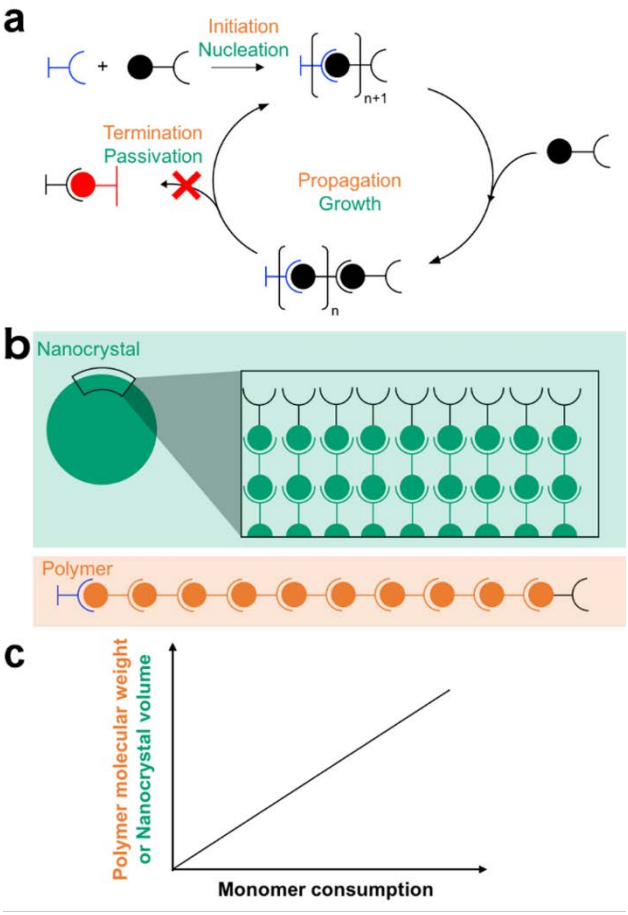

Figure 2.1. (**a**) The reaction cycle shows the general steps of a living process either for polymerization (orange lettering) or nanocrystal growth (green lettering). Starting materials initiate (or nucleate) to form species with a reactive site. Addition of monomer to this reactive site results in the generation of another reactive site (referred to as propagation or growth). In a living system, growth is indefinite, and proceeds without termination or passivation. (**b**) Examples of a nanocrystal (green) or polymer (orange) that would result from the general scheme in **a**. (**c**) A growth curve for a polymer or nanocrystal. Living growth is characterized by a linear correlation between monomer consumption and polymer molecular weight (for polymers), or a linear correlation between monomer consumption and nanocrystal volume (for nanocrystals).

Analogies between polymers and nanocrystals have been described.[5–7] Indeed, synthetic polymers and nanoparticles share many characteristics: not only do the properties of both materials depend on their size (or molecular weight) and composition, they are also characterized and described in much the same way: by type, average size, and polydispersity. The terminology of polymer chemistry and nanoparticle chemistry has many parallels (**Table 2.1**). A *living* approach to nanocrystal synthesis might possess attributes similar to living polymerization: it could produce product with low size dispersions, support further growth with additional monomer (i.e. not be limited in size), and result in high yields (i.e., precursor/monomer should be nearly completely consumed). Growth could be controlled precisely (e.g., layer-by-layer) in an intuitive manner involving living growth on the surface rather than undesirable processes, such as new nucleation, ripening, or coalescence, that (often) lead to a loss of synthetic control. Such living growth processes would offer a deliberate approach to assembling complex nanoscale structures.

Despite the analogies between polymers and nanocrystals, an important difference is the organic/inorganic interface. In the inorganic systems, surface chemistry will play an important role in any living growth process. Most nanocrystals are stabilized by surfactants (or ligands) during the growth process. If the ligands are too weakly bound, the nanocrystal will be prone to coalescence, whereas ligands bound too strongly will impede growth. Having proper surface reactivity, with labile surfactants and maintenance of reactive (living) sites for monomer addition, allows propagation of growth on the particle surface. Alternatively, a surface that is too stable, with strongly bound surfactants

and/or the absence of reactive sites will not be conducive to epitaxial growth. As a result, any growth ensues via heterogeneous nucleation consequently forming polycrystalline nanoparticles, or monomer will accumulate in solution, ultimately leading to new nucleation events and a dispersion of sizes.

Table 2.1. Analogous concepts and terminology between polymers and nanoparticles.

	Polymer synthesis	**Nanoparticle synthesis**
Analogous Terminology	Chain	Particle
	Initiation	Nucleation
	Propagation	Growth
	Chain termination	Particle passivation
	Block copolymer	Core/shell particle
	Random copolymer	Doped particle
Similar Terminology	Size	
	Dispersity	

Given the transformative nature of living polymerization methods, and the striking similarities between nanocrystals and polymers, obvious questions arise: do nanocrystal synthetic methods exist today that share the important attributes of living polymerization? How can one identify existing synthetic methods as living, or develop living synthetic methods for nanocrystals? If living approaches exist, to what degree can they be leveraged for improved composition and structural control? Below we analyze common methods of nanocrystal synthesis with a lens towards identifying living processes, and defining their synthetic prerequisites, behaviors, and outcomes.

The Hunt for Living Growth Methods

Currently many liquid-phase synthetic methods exist for the production of nanocrystals, including (but not limited to) aqueous reduction, aqueous sol-gel, non-aqueous sol-gel,

hydrothermal/solvothermal, thermal decomposition, and hot-injection.[8–12] Of those commonly employed for the production of monodisperse oxide nanocrystals, methods that take place in high-boiling organic solvents, including heat-up and hot-injection methods, are utilized the most.[13] Under these conditions, the key requirements for the production of uniform nanoparticles are thought to be the separation between nucleation and growth phases as outlined by LaMer[14] and the management of aggregation or Ostwald ripening (or "defocusing" events).[15]

At first glance, seeded growth methods mirror living growth processes.[5,16–22] Seeded growth techniques are applicable for a wide variety of semiconducting and metallic structures and have been successfully utilized to tune nanocrystal size for decades, sometimes with fine resolution.[16] In these methods, growth might take place through either heterogeneous nucleation on the particle surface or through discrete monomer addition to surface reactive sites, but the details are typically unknown. If a seeded growth synthesis is "living", one would expect the addition of more monomer to result in a *predictable* increase in core size (i.e., proceed with no aggregation, ripening, or new nucleation). In the majority of seeded growth literature, the number of particles present during the growth stage(s) or the expected size increase with precursor addition is not reported (with few exceptions[17,23]). Living syntheses should produce single crystal, homoepitaxial nanocrystals, which suggests monomer adds to a reactive surface instead of heterogeneous nucleation on the particle surface. It is often unclear in the seeded growth literature whether particles are single crystals. A recent study on the magnetic properties of iron oxide found that nanocrystals obtained from seeded growth methods produced strained regions in the nanocrystal, leading to anomalous magnetic properties.[24] Finally, in living growth,

monomer addition onto a crystal is an irreversible reaction, thus the rate of dissolution of monomer from the crystal surface should be negligible. As a result, no change in particle size or dispersion is expected upon annealing. **Table 2.2** outlines the prerequisites, synthetic attributes, and outcomes of living nanocrystal syntheses.

Slow addition of reagent to preformed seeds can result in monodisperse nanocrystals of metals, oxides, and semiconductors.[23,25–28] Some of these may be living growth processes, although it is difficult to know because predictions about expected nanocrystal sizes are not typically given, and size sorting processes (like size selective precipitation) are frequently utilized. The need for size selection implies that new nucleation has occurred during the growth process.

The Huber group found that size of iron oxide nanoparticles could be controlled predictably with sub-nanometer precision through the slow addition (3 mL/hr) of iron carboxylate into hot docosane and oleic acid.[25] Using small-angle X-ray scattering analysis (SAXS), following a period of rapid growth of particle to about 10 nm, they showed a linear correlation between nanocrystal volume and precursor addition (expected for living processes, **Figure 2.1**), and were able to grow nanocrystals to "arbitrarily large sizes." The reaction presumably proceeds through a type of thermal decomposition mechanism given that the reaction temperature (350˚C) is well above the thermal decomposition point of the iron oleate precursor (onset ~200-240˚C).[29] The study is a tremendous advance in the synthesis and size control of iron oxide nanocrystals. However, there is still much to learn about this growth process: Is new monomer being incorporated by surface reaction(s), or is heterogeneous nucleation the cause for the observed growth behavior? Further, is there particle ripening upon annealing?

Table 2.2. Connection between prerequisites, synthetic attributes, and outcomes for living growth nanocrystal synthesis.

Prerequisites	Synthetic attributes	Outcomes
• Maintenance of reactive surface (no surface passivation) • Constant number of growing species • Non-reversible monomer addition	• Predictable, linear growth of core molecular weight (volume) with monomer consumed • Addition of more monomer results in further growth • No ripening upon annealing • High yield	• Highly tunable size with narrow dispersity • High level of control over structure & composition • Single crystal particles

Our group recently discovered a synthetic route that embodies the attributes of a living growth process outlined in **Table 2.2**. Slow addition of metal carboxylates into oleyl alcohol at temperatures below the thermal decomposition point of the precursor affords a large variety of metal oxide nanocrystals (including In_2O_3, γ-Fe_2O_3, Mn_3O_4, CoO, and ZnO).[30] The reaction proceeds via the esterification of metal oleates to produce metal hydroxides, which then condense onto the particle surface (**Figure 2.2**). We were initially surprised by several aspects of this synthesis. It seemed particularly unusual that the *slow* addition of reagents produced single crystalline, monodisperse nanocrystals in very high yield (often >90%). One would normally expect the addition of more metal precursor to result in the new nucleation of nanocrystals, which would significantly increase the size distribution. Because the method produces monodisperse nanocrystals, we sought to understand the growth mechanism.

Using In_2O_3 as a model system, and a combination of transmission electron microscopy (TEM) and SAXS, we investigated how nanocrystal size, size dispersion, and shape evolved as a function of metal precursor addition. With SAXS, we could also investigate the number of nanocrystals present in solution. We found that nanocrystal

volume grows linearly with the amount of precursor added (**Figure 2.2**) and the number of nanocrystals present during this time is constant. These findings suggest that growth proceeds through a living process.[31] Even more extraordinary, the nanocrystals can be left in reaction solution at elevated temperatures for hours without a change in the average size or size dispersion and are susceptible to further predictable growth upon addition of monomer after this "annealing" period. Since the publication of this finding we have reliably made nanocrystals from three to more than 30 nm in diameter in gram quantities and have yet to find a maximum size that can be produced. We believe this growth mechanism is sustained by hydroxyls continually present on the nanocrystal surface and reactive hydroxyls produced via the esterification of metal oleates with oleyl alcohol (**Figure 2.2**).

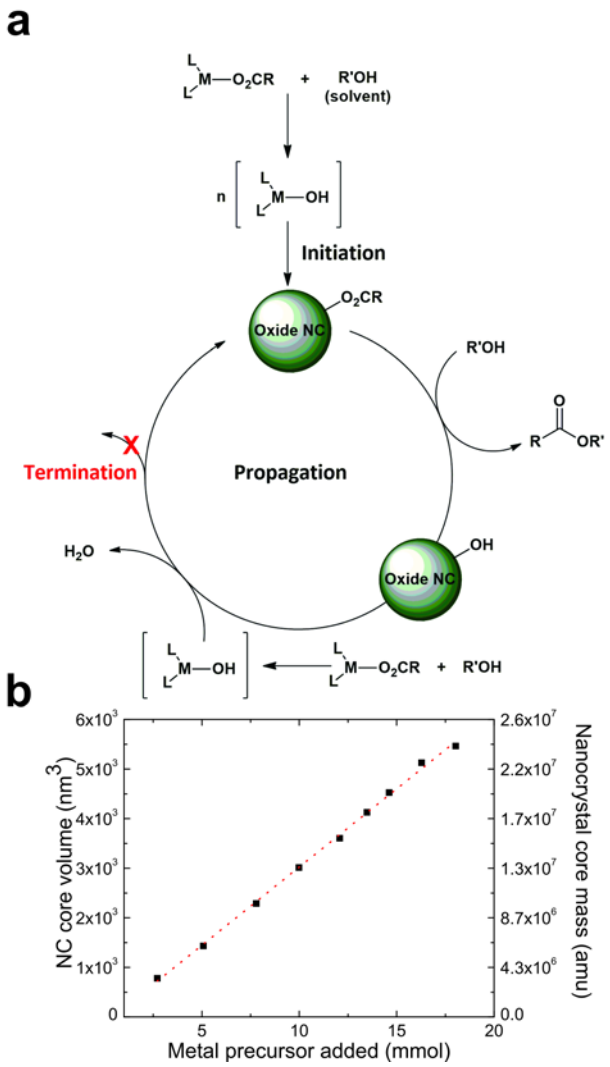

Figure 2.2. (**a**) Schematic representation of our living growth synthesis of metal oxide nanocrystals. Slow addition of metal oleate promotes metal hydroxide formation leading to initiation of nanocrystal growth. Nanocrystals continue to grow during propagation as additional monomer is added. Metal hydroxyls on the nanocrystal surface support a living growth mechanism. (**b**) SAXS data taken during the synthesis of In_2O_3 nanocrystals. We found a linear correlation ($R^2 = 0.998$) between the nanocrystal core volume (e.g. core molecular mass) and the amount of metal precursor added to the reaction flask. Analogous to a living polymerization reactions, this synthetic method allows access to particle sizes with sub-nanometer precision, as well as the logical preparation of more complex structures and compositions, including doped and core/shell nanocrystals. Adapted with permission from reference 31. Copyright 2016 American Chemical Society.

Our findings from these initial studies pointed towards a growth mechanism for metal oxide nanocrystals that we believe has unmatched potential. Drawing analogies to

polymer chemistry (**Table 2.1**), we ventured to apply these ideas to living nanocrystal growth and harness the attributes of living growth to produce structures and compositions previously impossible to synthesize. In the following sections, we describe three tests of the potential of our living growth system, highlighting the advantages and significance of this new approach.

Leveraging Living Methods to Achieve Advanced Structural Control

Increasing Doping Efficacy

Doping, or the intentional introduction of extrinsic defects, is a common way to impart new electronic, optical, or magnetic properties within inorganic materials and is critical for the development of high-performance applications of these materials. Doping bulk materials, via diffusion or ion implantation, is now commonplace and essential to the electronics industry. Doping methods for colloidal nanocrystals, however, are much less developed. Excellent recent reviews on the subject can be found in the literature.[32–34] Not surprisingly, because of the high energy required to substitute dopant atoms within the host framework of a nanocrystal, dopants are often excluded to the surface, form new clusters or secondary phases, or are not incorporated into the crystal at all.[35] Because of the inherently small number of atoms in a nanocrystal, small changes in the number of dopant atoms can result in the drastic alteration of properties. As a result, it is imperative that the concentrations of dopants be predictably controlled within a material. Living growth methods for nanocrystal synthesis should enhance the extent of structural control one can gain over nanocrystal composition and structure, particularly dopant distribution.

A key prerequisite to effective doping in nanocrystal synthesis is matching host and dopant precursor reaction rates in order to successfully incorporate and substitute dopant

atoms into a host lattice.[32] Reliable incorporation of dopant atoms can be extremely challenging using traditional approaches. In thermal decomposition reactions for instance, precursor reactivity must be considered and estimated in order to achieve even modest doping efficiencies. As an extreme example, the synthesis of Mn-doped ZnS nanorods at 1.6 atomic % required a 20 molar % Mn precursor solution (an incorporation efficacy of only 8%).[36] While such low efficacy could be improved greatly by altering the choice of the reagents, finding the appropriate precursor given the synthetic conditions can be a challenge. An improvement in dopant incorporation efficiency seems to have emerged thanks to the recent utilization of so called "nonaqueous sol-gel" routes to produce doped nanocrystals.[12,37–41] These mechanisms rely on defined molecular transformations, rather than thermal decomposition, to arrive at the final doped product. In general, utilization of predictable chemistries to produce metal-oxygen bond formation, facilitated by ester, amide, or ether formation, can simplify the choices of appropriate metal precursors, and allow for higher doping efficiency. However, just as in thermal decomposition reactions, if both dopant and host precursor do not catalyze bond formation at the same rate, then the desired doped product may not be formed.[37,41]

We hypothesized that utilization of our *slow* injection, living growth method[30] would allow for more effective dopant incorporation as differences in metal-catalyzed esterification rate would be overcome by the slow nature of precursor addition. Additionally, rather than carefully selecting metal precursors based on perceived reactivity, we chose to use metal oleates in desired molar ratios. We doped In_2O_3 with Mn, Fe, Co, Cu, and Zn ions, each with nominal concentrations of 5, 10, and 20 molar % dopant (**Figure 2.3**).[42] The dopant incorporation in Cu: In_2O_3 nanocrystals matched that of the precursor

with ~70% efficacy, while the incorporation in Mn, Fe, Co, and Zn: In_2O_3 nanocrystals doped with an impressive >90% efficacy, as measured my inductively coupled plasma optical emission spectroscopy (ICP-OES). Powder X-ray diffraction (XRD) confirm that the nanocrystals are bcc-In_2O_3 (**Figure 2.3**), and by using Reitveld analysis can confirm the decrease in lattice constant with increasing dopant concentration, as expected when smaller dopant cations replace larger In^{3+} cations. The nanocrystals are formed with small size dispersions, and the mean size of the nanocrystal can be altered with same level of precision as undoped nanocrystals (**Figure 2.2**).[31] We find agreement in dopant concentration of the entire sample (using ICP-OES) to the nanocrystal surface dopant concentration (using X-ray photoelectron spectroscopy, XPS). This indicates that the dopants are not surface segregated but distributed homogeneously throughout the sample. While host and dopant cation size will invariably play a role into incorporation efficiencies, we demonstrate that higher incorporation is possible if synthetic methods operate with living attributes. We anticipate this discovery will pave the way for further studies utilizing doped nanocrystals, including the controlled introduction of multiple dopants into single nanocrystals. Co-doped systems have the potential to simultaneously control multiple properties, and/or act synergistically with one another to enhance a single property.[43–45] Controlling the radial placement of dopants or the introduction of dopants into core or shell of a core/shell heterostructure, as we discuss below, allow an even greater level of structural control.

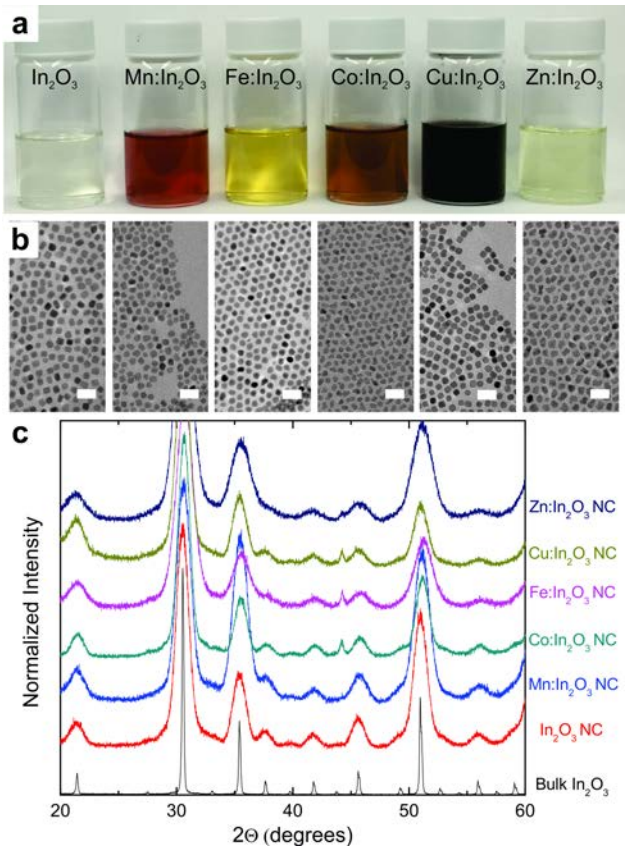

Figure 2.3. (**a**) A picture of doped oxide nanocrystals that have been purified and suspended in hexanes. The vials, from the left to right, correspond to undoped In_2O_3, Mn: In_2O_3, Co: In_2O_3, Fe: In_2O_3, Cu: In_2O_3, and Zn: In_2O_3 all doped at 10 atomic %. (**b**) Corresponding TEM images of samples from each solution, directly beneath the vials in (**a**). Scale bars are 20 nm. (**c**) Powder X-ray diffractograms from each of the samples. All diffraction patterns match the bcc-In_2O_3 crystal structure.

Intentionally Modifying the Radial Position of Dopant Atoms Within Nanocrystals

Unique properties can be harnessed in materials when synthetic methods can alter structure on the atomic scale. An excellent example of this is the drastic difference in properties that arise between doped nanocrystals that have the same composition but different radial placement of dopants within the nanocrystal. One might logically expect this is due to the different chemical environments of surface vs. buried inner atoms. Sometimes these properties can provide useful insight. For instance, different electronic absorption features between tetrahedral surface-bound dopants and tetrahedral

substitutional dopants aided in understanding the growth mechanism of doped ZnO.[46] Controlling the specific placement of dopants *with intention* however, has been difficult, and prevailing colloidal nanocrystal synthetic methods provide very little opportunity to produce structures with deliberate dopant placement. Nanocrystals produced in a living manner on the other hand, with layer-by-layer control over composition, would allow the precise placement of dopant atoms within a nanocrystal, thereby granting the synthetic chemist an enhanced level of mastery over important properties.

One important property that arises in many doped oxide nanocrystals is the near-IR or IR localized surface plasmon resonance absorption (LSPR). LSPRs arise in many heterovalent doped-oxide nanocrystal because extrinsic defects contribute free electrons into the conduction band of the material and oscillate at a particular frequency. These materials have become an area of active research interest because of their potential in chemical sensing, biology, electronics, and energy production.[47–53] Key metrics of LSPRs are quality factor ($LSPR_{max}$ energy divided by the linewidth of the LSPR) and dopant activation (the number of free electrons in the nanocrystal divided by the number of dopant atoms).

It has been found empirically that different synthetic methods for doped oxide nanocrystals lead to differences in the radial position of dopants. Different reactivities of the metal precursors and ligand types presumably influence the extent and timing of dopant incorporation. In a striking example that demonstrates the large influence the radial placement of dopant atoms has on material properties, the Milliron group investigated two different synthetic methods for Sn-doped indium oxide (ITO) nanocrystals.[54] They found that one method produces homogeneously-doped ITO and the other produces surface-

doped ITO. They attributed the large difference in the LSPR response to the radial distribution of dopants. While the synthetic methods utilized for that study produced doped nanocrystals with varying radial distribution of dopants, such distributions were not the intended outcome of the original synthetic methods.[55,56] Furthermore, these synthetic methods do not allow for independent control of dopant concentration, the radial distribution of dopants, and nanocrystal size.

We recently demonstrated that utilizing our slow injection approach,[30,31] one can intentionally tune the optical properties of ITO nanocrystals through precise control over the radial distribution of dopants.[57] We synthesized ITO/In_2O_3 core/shell (core-localized dopant), In_2O_3/ITO core/shell (surface-localized dopant), and homogeneously-doped ITO nanocrystals and investigated the differences in LSPR response (**Figure 2.4**). Using a combination of elemental analysis by both ICP-OES (that yields composition information about the entire nanocrystal sample) and surface analysis by XPS, we confirmed the radial locations of the dopants in each of the three cases. Because the synthetic method operates with living attributes, production of the nanocrystals was a simple, one-pot reaction that did not require purification in between precursor addition(s) (**Figure 2.4**).

We followed LSPR response as a function of doped or undoped shell thickness, and showed that core-localized doped nanocrystals have significantly higher dopant activations and quality factors. We confirmed that these large differences between the nanocrystals are due to the presence of defect-free zones in either the core or shell of a nanocrystal, in addition to inactive dopants on the surface of the nanocrystal. Because small, sub-nanometer shells can be grown onto the core nanocrystal using our approach, we showed

that it was possible to activate surface dopants through the addition of a small, sub-nanometer undoped shell to a doped surface.

Using a living approach allows significantly enhanced control over $LSPR_{max}$ and quality factor and allows one to rationally sculpt optical properties for specific application. Undoubtedly, the importance of enhanced command over the radial placement of dopant atoms will extend beyond that of ITO. We expect that radial dopant placement will become standard consideration for understanding the many properties of doped nanocrystal systems, and anticipate the development of further living syntheses that offer opportunity to control catalytic, magnetic, electronic, and other important physical properties.

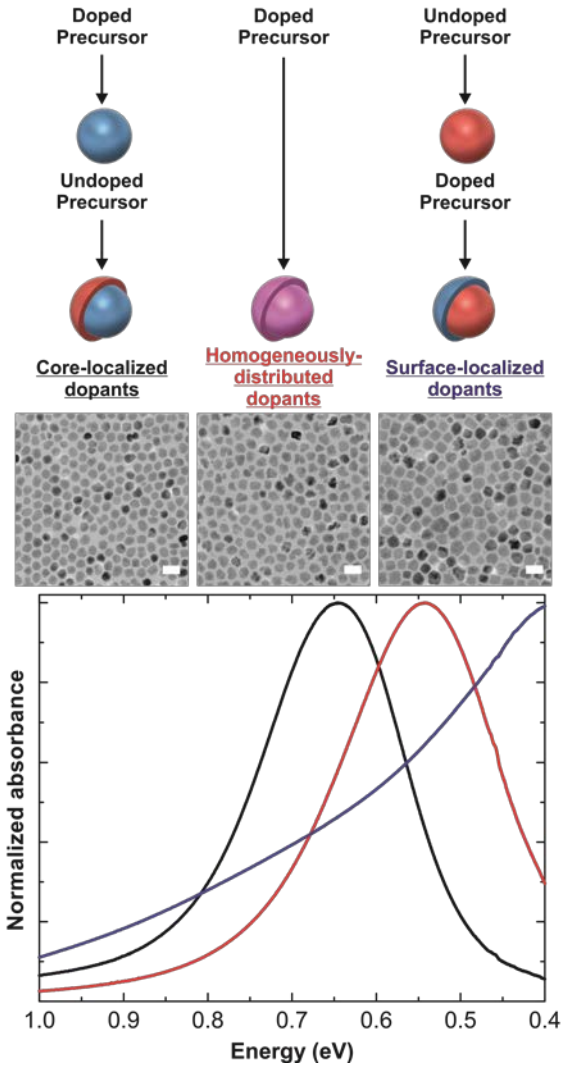

Figure 2.4. Using a living approach, the radial position of dopants can be controlled intuitively through the addition of doped or undoped precursor, represented by the top reaction schemes. No purification of the nanocrystals is necessary between precursor additions and particles can be synthesized in one pot. We synthesized ITO nanocrystals with varying radial placement of dopants that were between 10.2-12.8 nm in diameter, containing the same concentration of Sn (within 0.5 atomic %). Below the top scheme are TEM images corresponding to (from left to right) core-localized, homogeneously distributed, and surface-localized dopants. Scale bars are 20 nm. As shown in the bottom plot, core-localized ITO nanocrystals (black trace), ITO with homogeneously distributed dopants (red trace), and surface-localized ITO nanocrystals (blue trace) have drastically different LSPR line shape and maxima. Core-localized dopants have higher quality factors and activations.

Implications of Living Synthetic Methods for Core/shell Nanocrystal Growth

Core/shell nanoparticles are hybrid nanostructures in which an inorganic core of one material is surrounded by a different material.[58] Core/shell particles are generally of interest to impart advantageous properties of the multiple materials they comprise or improve the existing properties of one or both components. For example, this approach has been invaluable to quantum dot research in which quantum yields and photoluminescent stability of semiconductor nanoparticles are greatly improved by passivating its surface trap states with a different semiconducting material.[59–61] However, current colloidal syntheses for creating the core/shell structure are hampered by several limitations. These limitations include undesirable homogeneous nucleation of shell material, incomplete surface coverage on the core, and non-epitaxial or amorphous growth.[59]

Widely used and robust synthetic schemes have been discovered and applied to core-shell synthesis. Two of the most common are the Stöber method used to synthesize silica shells,[61] and adaptations of the successive ion layer adsorption reaction (SILAR) method used to produce quantum dots.[62–64] In the SILAR method, layers of cations and anions are added sequentially to build one atomic layer at a time, typically with purification steps between each. Additionally, careful calculations to determine the amount of anion or cation precursor (often less than one monolayer per addition) are necessary in order to avoid new nucleation events.[62,64] As a result, growing shells is tedious. In the Stöber method, a tetra-alkoxy silane precursor is hydrolyzed then condensed onto existing particles. The method has been adapted for the synthesis of other oxide shell materials, including TiO_2, ZrO_2 and SnO_2.[58] In general, the shells are

amorphous and often do not fully passivate the core. Though there are some examples of core/shell syntheses comprising different metal oxides,[65–67] there isn't a general, tunable synthetic strategy to do so.

We anticipate that living growth methods will immensely aid in the successful synthesis of a variety of core/shell particles and produce structures with advantageous magnetic, electronic, catalytic, and optical properties. This is a result of the living nature of the synthesis method. Because the core surface remains reactive through the formation of active functional groups and there is high yield in precursor consumption, sequential additions of different metal precursor will suffice in creating an abrupt change from core to shell material. Such a procedure is intuitive and simple, eliminating the need for rigorous purification and quantification of shell precursor. The nature of regenerating a reactive surface holds several advantages to shell growth. Precursors of different metal salts will favor condensation onto these sites rather than new homogeneous nucleation. Condensation of metal precursor will tend towards epitaxial growth because growth onto cores is not a heterogeneous nucleation event. Furthermore, because we anticipate the growth will not be promoted by heterogeneous nucleation, growth should occur over the entire particle surface rather than creating islets or dimer-like species.

Indeed, our group has published preliminary results of successful core/shell growth. The synthesis of γ-Fe_2O_3/MnO and ZnO/β-Ga_2O_3 core/shell particles with the slow injection synthesis displayed epitaxial and uniform growth of shell material around core.[30] We expect that growing sequential shell materials on one another utilizing a living method will be possible, and will maintain the same level of composition control as described above. Given the amount of precursor added and the size of a particle, it

follows that one can calculate the required amount of precursor material to yield a shell of desired thickness.

Bridge to Chapter III

Now that living nanocrystal synthetic methods have been defined and the fine structural control possible with such approaches has been briefly discussed, the following chapters expand upon data presented in Figures 2.2-2.4. Chapter III serves as the first report on living nanocrystal growth, demonstrating precise and predictable size and composition control of oxide nanocrystals. The synthetic method illustrates all of the analogous characteristics observed in living polymerization reactions. Since the publication of chapter III, we have made oxide nanocrystals as large as 30 nm, expanding the maximum size demonstrated in the following chapter.

CHAPTER III

CONTINUOUS GROWTH OF METAL OXIDE NANOCRYSTALS: ENHANCED CONTROL OF NANOCRYSTAL SIZE AND RADIAL DOPANT DISTRIBUTION

This chapter was previously published as Jansons, A. W.; Hutchison, J. E. Continuous Growth of Metal Oxide Nanocrystals: Enhanced Control of Nanocrystal Size and Radial Dopant Distribution. *ACS Nano* **2016**, *10* (7), 6942–6951.

Introduction

A wide range of nanocrystal syntheses have been developed in recent years that provide size control of uniform populations of nanoparticles.[1,2] For semiconducting nanocrystals, the traditional heat-up and hot-injection methods often achieve this by modifying the kinetics and thermodynamics of nucleation, principally through the level of supersaturation, reaction temperature, choice of stabilizing ligands, and alteration of precursor conversion kinetics.[3–7] The mechanisms involved are based on classic LaMer theory,[8] and more quantitative models.[9,10] Even with these advancements in our understanding of nanocrystal formation, selecting appropriate synthetic conditions for a desired nanocrystal structure remains challenging.

In addition to modifying the rate of nucleation, “multiple injection” or “seeded growth” strategies have been used to synthesize nanocrystals with varying degrees of size control. Seeded growth strategies, whereby preformed nanoparticles are mixed with metal

precursors and surfactants in optimized ratios, has shown success in both metal and oxide nanocrystal syntheses.[11–16] Secondary rapid-injection of precursors and surfactants into the original reaction solution can also be used to grow both semiconducting nanocrystals and nanowires,[17–19] however the above methods are often limited in their size control and size resolution control. Because the detailed mechanisms of growth in many of the previous approaches involve complex processes, such as ripening and aggregation, seeded growth or "dynamic injection" strategies often require careful selection of reaction conditions so as not to induce new nucleation or product formation with unreacted precursor. Strategies include isolating (and often purifying) the nanocrystal seeds, lowering the reaction temperature for shell growth, and carefully selecting the shell-forming precursor.

An ideal nanocrystal synthetic method would allow for a continuous, layer by layer construction of a nanoparticle at the sub-nanometer level, similar to the "living metal-polymer" idea first conceptualized by Watzky *et al.*[20] A continuous growth synthetic method applicable for a wide variety of inorganic nanomaterials would allow precise and predictable structural control analogous to that provided by living polymerization in macromolecular chemistry. Several groups have recently acknowledged the importance of more generalizable synthetic methods for assembling complex nanomaterials,[21] and suggest the utility of polymer-like control in nanowire and quantum dot syntheses.[20,22–24] To achieve such control requires a system in which no new nucleation takes place during growth, the number of growing species remains constant, and intermediate nanocrystal cores do not passivate. An ideal synthesis would permit epitaxial growth of core/shell structures and the seamless control of concentration gradients within doped nanocrystals.

Such approaches would offer precision and control of the internal nanostructures and sizes, which dictate the properties of nanocrystal cores.

Recently, several synthetic approaches have been reported that employ slow addition of precursor to extend the growth of nanocrystals and demonstrate some of the potential benefits of continuous growth process.[25–27] We previously showed that slow addition of metal oleates into hot oleyl alcohol produced monodispersed nanocrystals for a variety of binary oxides.[28] The catalytic esterification reactions that lead to nanocrystal formation seemed ideal to examine whether these syntheses could be used to carry out continuous growth of binary oxide nanocrystals and, potentially, to control the radial placement of dopant atoms in the oxide matrix. To this end we examined the growth process for indium oxide nanocrystals during slow addition of precursor under conditions where thermal decomposition of the precursor does not occur. We show that this process shares attributes common to living growth in polymers, yielding nanocrystals with predictable sizes and compositions over a range of three to over 22 nm in diameter. The surfaces of the nanocrystals retain their reactivity, and thus are amenable to further growth of either the core material or even doped material. The continuous growth process permits the synthesis of core/shell nanocrystals with custom radial dopant compositions that, in turn, allow predictable tuning of the energy of the localized surface plasmon resonance. The continuous, controlled growth process offers an intuitive approach to precise and predictable size control of metal oxide nanocrystals.

Results and Discussion

Previously we showed that *slow* addition of a metal oleate to oleyl alcohol at elevated temperatures (> 200 ^{o}C) yields crystalline nanoparticles for a variety of binary metal oxides

at temperatures below the thermal decomposition point of the precursors.[28] It was also possible to produce core/shell nanocrystals using this method. Spectroscopic studies reveal the production of an ester, oleyl oleate, during the synthesis, resulting in the formation of a metal hydroxyl species. As the concentration of M-OH species increases, condensation eventually occurs to form metal oxide nanoparticles stabilized primarily by oleic acid (Scheme 3.1). Metal hydroxide condensation is accompanied by the production of water, observed both in the reaction flask and by ^{1}H NMR spectroscopy.

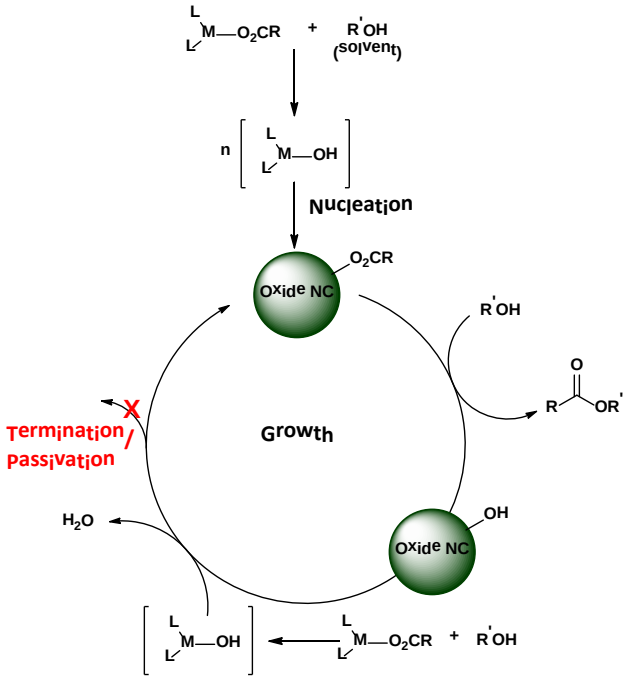

Scheme 3.1. Overview of the continuous, controlled growth synthesis of metal oxide nanocrystals. Slow addition of metal oleate promotes rapid metal hydroxide formation leading to initiation of nanocrystal growth. Nanocrystals continue to grow as additional precursor is added. Metal hydroxyls on the nanocrystal surface support a continuous growth process in which particle size is not limited.

Although a variety of binary and doped oxide nanocrystals have recently been produced through esterification of metal carboxylates in long-chain alcohols (including In_2O_3, γ-

Fe_2O_3, Mn_3O_4, CoO, and ZnO),[28–32] little is known about their growth mechanism. We chose to investigate indium oxide in detail because of our interest in the optical and electronic properties of these nanocrystals as a function of nanocrystal size and tin doping level. Indium oxide nanocrystals were synthesized through the dropwise addition (0.3 mL/min) of indium oleate solution into oleyl alcohol at 290 °C. Small aliquots were taken and quenched by rapid cooling to room temperature. Purified samples were characterized by small-angle X-ray scattering (SAXS). Transmission electron microscopy (TEM) images were also collected and offer complementary size and size dispersion information to SAXS that serve to validate the generated SAXS models.[33] We were able to monitor nanocrystal size, size dispersion, and concentration with SAXS (Fig. 3.1) and validate this data using TEM (Fig. 3.2).

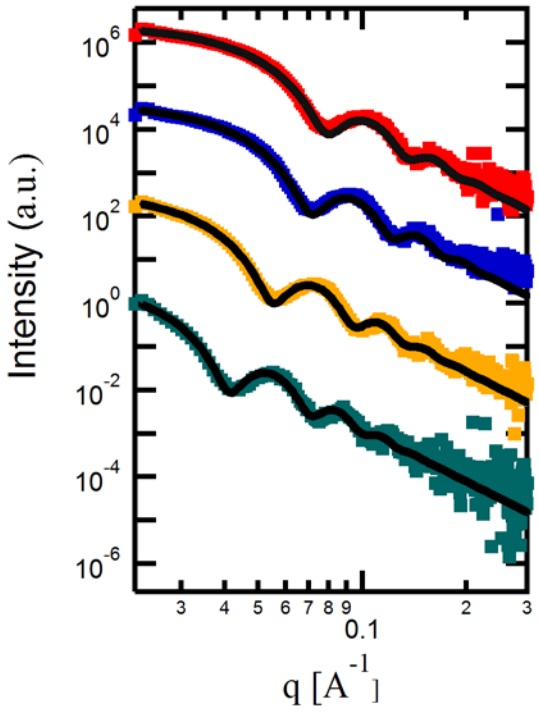

Figure 3.1. Representative small-angle X-ray scattering data. Colored dots represent raw SAXS data collected, and the black lines represent fits to the data. Modeled sizes of nanocrystals from top to bottom are 11.4 nm, 12.7 nm, 16.4 nm, and 21.9 nm.

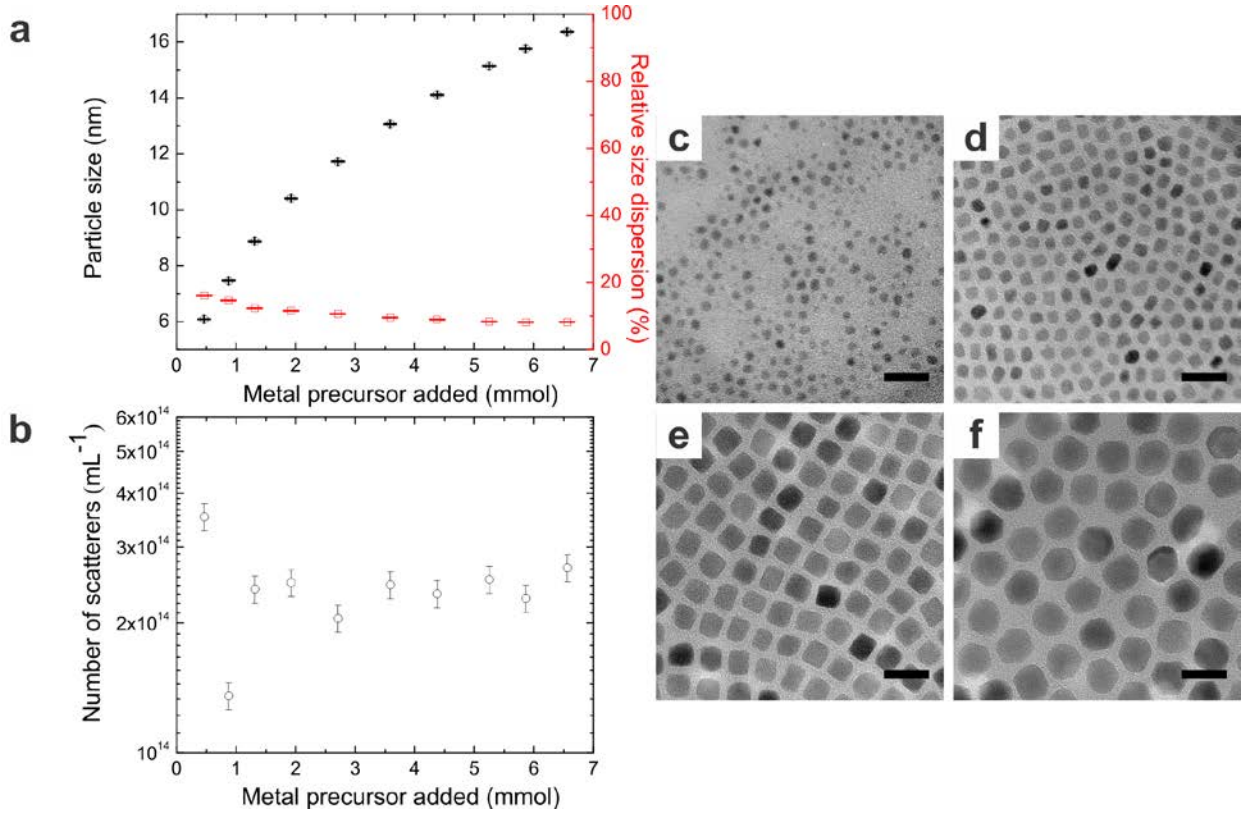

Figure 3.2. SAXS and TEM data from a typical slow-injection synthesis of indium oxide nanocrystals. Nanocrystal aliquots were quenched and the size, size dispersion, and concentration evaluated. (a) Average particle size and relative dispersity (1σ) from SAXS as a function of metal precursor added to the reaction. Since the same volume of solution was taken out of the reaction flask for each aliquot, the number of particles (or scatterers) could be calculated and compared over the entire synthesis period, as shown in b. (c) TEM image of 3 nm particles after 0.2 mmol indium addition. (d-f) TEM images of 6.1 nm, 11.7 nm, and 16.4 nm particles (corresponding to first, fifth, and last points in 2a, respectively). Scale bars are 20 nm.

This initial study showed continuous nanocrystal growth as a result of further precursor addition. (Fig. 3.2a). No nanoparticles were observed immediately after metal precursor addition began, however crystalline particles were detected in the reaction solution after the addition of 0.2 mmol of metal (Fig. 3.2c). Based upon the SAXS data (Fig. 3.2a) and corresponding TEM images in Fig. 3.2c-f, the particle size increased steadily from 6-16 nm as more metal precursor was added. The relative size dispersity decreased over this

addition, and at core sizes greater than 8 nm, the particles became monodisperse, as revealed by both SAXS and TEM (1σ by SAXS = 7-8%). The absolute dispersity for this dataset (plotted in Fig. A1) remains essentially constant after the addition of 2 mmol of precursor, suggesting that processes such as ripening and size focusing are not occurring during the later stages of the growth process. The size dispersion was even smaller by TEM, 1σ = ~5% (see Fig. A2 for TEM size analysis).

SAXS analysis revealed that the number of particles in the reaction vessel remained nearly constant through the entire precursor addition (Fig. 3.2b), suggesting that little coalescence and ripening occurs, and no additional nucleation begins. Further, if precursor addition was stopped at any point during the synthesis and the solution left under synthesis conditions for several hours, nanocrystals did not change shape or size during that time (see below and Fig. A6). When precursor addition resumes, growth continues as expected. These attributes are consistent with a continuous growth process analogous to that found in living polymer chemistry.[34]

If the nanocrystal cores remain reactive, there should be no upper limit to the nanocrystal size that can be produced. Under standard synthetic conditions, we were initially unable to grow nanocrystals larger than 16 nm (Fig. 3.2a). Because alcohol is consumed during nanocrystal growth, we hypothesized that this may be due to the consumption of all the alcohol initially in the reaction vessel. By adding more alcohol to the reaction flask during the synthesis, larger nanocrystals were obtained. SAXS and TEM analysis (Fig. 3.3) confirm the synthesis of monodisperse nanocrystals up to 22 nm in diameter. We expect that larger sizes are possible through the continued addition of precursor, assuming enough alcohol is present to continue esterification. For a typical batch, over 3.0 g of monodisperse

22 nm nanocrystals were obtained as a solid powder (see Figs. A3 and A4 for further SAXS analysis and a picture of gram quantities of the product).

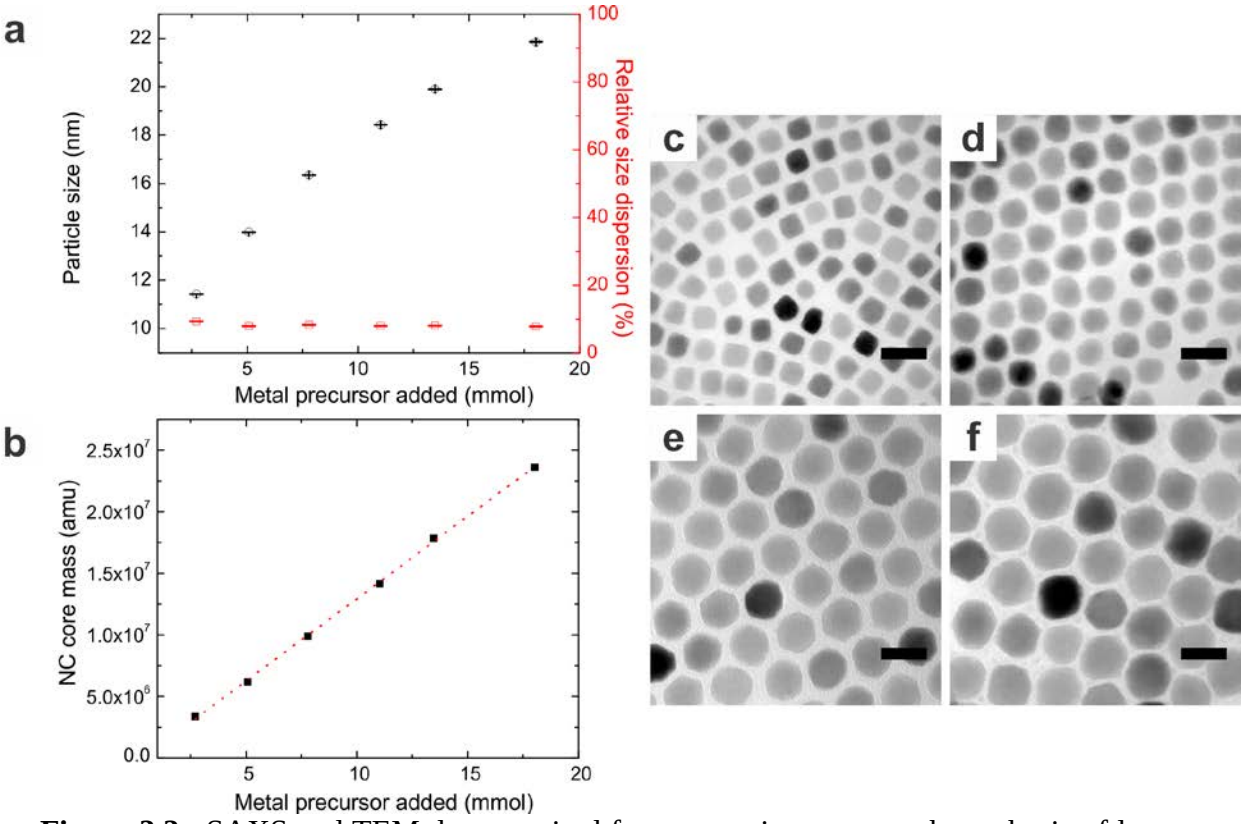

Figure 3.3. SAXS and TEM data acquired from a continuous growth synthesis of larger nanocrystals. To produce nanocrystals larger than 16 nm, additional reactant (alcohol) was added to the vessel to ensure esterification of metal carboxylate would continue. (a) Particle diameter from SAXS as a function of metal precursor added displays the growing nanocrystal size with precursor addition, while maintaining < 10% size dispersion. (b) SAXS data re-plotted as particle core mass *versus* added precursor, showing a linear correlation ($R^2 = 0.998$) between core mass and monomer conversion. (c-f) TEM images of 11.4, 13.9, 18.4, and 21.9 nm nanocrystals, corresponding to the first, second, fourth, and last data point in a, respectively. Scale bars are 20 nm.

Nanocrystal growth utilizing this slow-injection approach exhibits several signatures that are common to living polymerizations. First, as mentioned above, precursor addition can be halted, left at reaction temperature (or room temperature), and restarted without any change to particle size or size dispersion (see Fig. A6 and Methods section). Second, we

observed a linear correlation (Fig. 3.3b) between the average molecular weight of a nanocrystal core and the addition of metal precursor up to a molecular mass of at least 25 million. In typical living polymerizations, because the number of growing chains is constant, a linear correlation between monomer conversion and polymer molecular weight is observed.

We suspected that the surface hydroxyl groups are responsible for sustaining nanocrystal growth (or, alternatively, terminate growth if the hydroxyls become passivated or dehydrate to an oxo species) as shown in Scheme 3.1. To test this hypothesis, we investigated whether nanocrystal growth can be sustained in their absence by eliminating the hydroxyls through reaction with a long-chain silane reagent. To this end, we synthesized 10.4 nm In_2O_3 nanocrystals. Half of these nanocrystals were treated with trimethoxy(octadecyl)silane. A TEM of the silane-treated, purified product is shown in Fig. 3.4a, along with an EDX and XPS spectra indicating the presence of silicon (Fig. A5). No discernable changes in the size or disparity of the nanocrystals were observed during silanization. When additional metal precursor was added to the silane-coated particles, significant changes in morphology and polydispersity of the sample were observed (Fig. 3.4b). The anisotropy of the grown nanocrystals, along with the presence of two populations of nanocrystals (one much smaller than the original), imply that growth on existing cores was hindered and new nucleation occurred. When additional precursor was added to the untreated nanocrystals, growth continued as expected, producing larger,

monodisperse nanocrystals. (Fig. 3.4c). These results suggest that continuous growth occurs through monomer addition to the surface hydroxyl groups

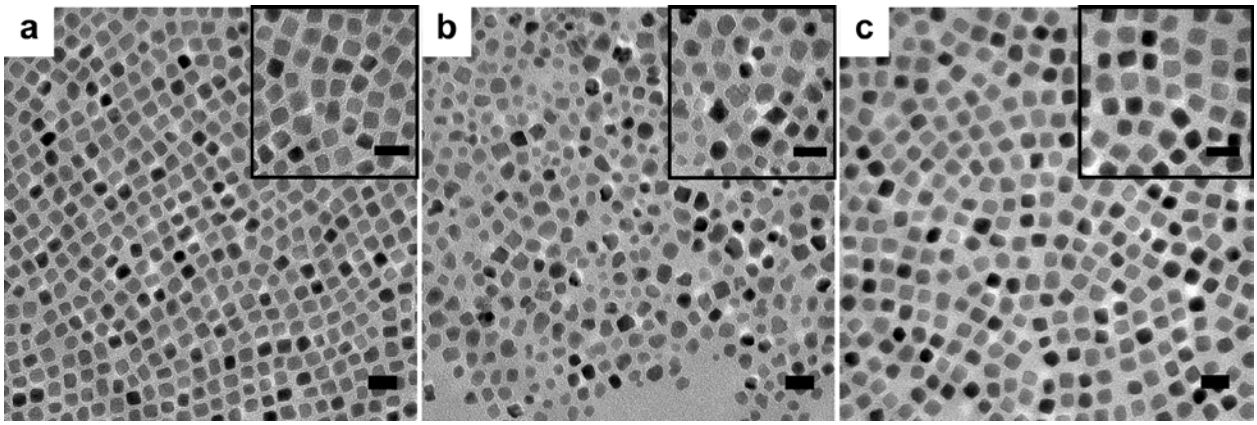

Figure. 3.4. TEM images assessing nanocrystal growth in the presence and absence of a long-chain silane. The silane reacts with surface hydroxyls of the nanocrystals. (a) Washed particles after treatment with the coupling agent (10.4 nm by SAXS). An EDX and XPS spectra (Fig. A5) shows the presence of silicon. (b) After addition of 0.5 mmol metal precursor under standard synthetic conditions, particle growth is suppressed and two populations of nanocrystals are present, indicating that growth is inhibited and new nucleation has occurred. (c) The experiment performed under the same conditions as those in b, without the addition of the coupling agent. Particles are 11.3 nm by SAXS, suggesting that growth is not suppressed and nanocrystals continue to grow. All scale bars are 20 nm.

During the growth process, we observed striking morphology changes in the nanocrystals as a function of core size by low-resolution TEM (Fig. 3.2 and 3.3). Because key properties of nanomaterials depend upon shape and facets, in addition to the core size,[35] we investigated select samples with HRTEM (Fig. 3.5). The nanocrystals are single crystals at all core sizes, indicating that growth occurs epitaxially at the particle surface. At smaller sizes, the nanocrystals appear cubic passivated by {001} facets, while at larger sizes the [011] and [012] planes dominate the cuboctahedra. This shape change suggests that the {001} facets are growing at a faster rate than other planes,[35] and as a result the nanocrystals become mostly passivated by the slower growing planes. As previously detailed,[28,36] {001}

facets of In_2O_3 become more stable when passivated by water or hydroxide, indicating that growth proceeds by hydroxide condensation.

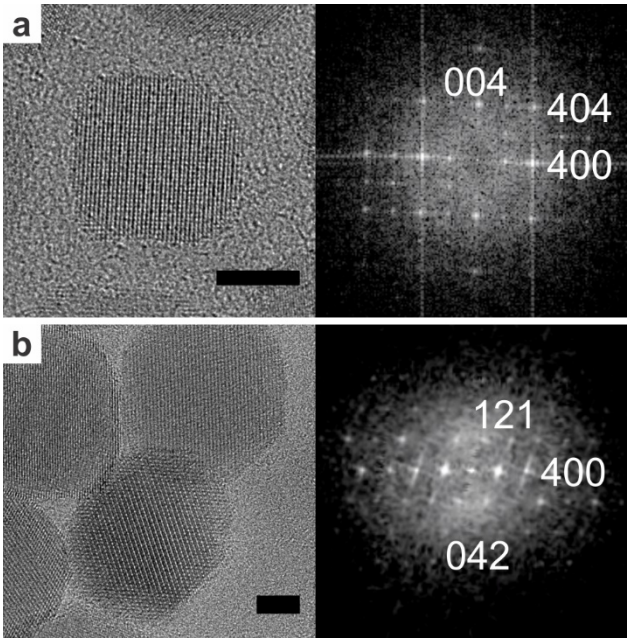

Figure 3.5. HRTEM and FFT images of representative nanocrystals. Smaller particles (a) have a truncated cubic morphology and are passivated by {001} planes. The FFT on the right displays the [010] zone axis. b. Larger particles appear octahedral. The FFT on the right displays the [012] zone axis. All particles are single crystals. Scale bars are 5 nm.

The fact that the surface hydroxyls remain active throughout the synthesis allows easy and logical preparation of more complex structures, specifically core/shell nanocrystals.[37,38] We examined this aspect of the growth method by producing a series of Sn-doped In_2O_3 (ITO) nanocrystals with a shell of In_2O_3 (ITO/In_2O_3 core/shell nanocrystals). To produce doped nanocrystals using more traditional methods (*i.e.* thermal decomposition or hot-injection), the reactivity of the host and dopant precursor must be determined empirically and carefully balanced to control dopant density.[39] Our slow-injection approach using metal oleates as precursors allows effective incorporation of dopants that is easily controlled by simply varying their feed ratios.

An ITO core was synthesized by slow addition of a mixture of indium and tin precursors into oleyl alcohol. At the end of this addition, the core reached 6.3 nm, and additional indium oleate was added to grow the shell. No purification was necessary before shell growth. SAXS and TEM data on core/shell particles of varying shell thickness are presented in Fig. 3.6.

Particle	Total precursor added (mmol)	Particle size (nm)	% Polydispersity	TEM image
ITO core	0.5	6.3	15.7	a
ITO/In_2O_3 core/shell	1.0	7.4	12.5	b
ITO/In_2O_3 core/shell	2.0	9.4	10.6	c
ITO/In_2O_3 core/shell	4.0	12.8	12.0	d

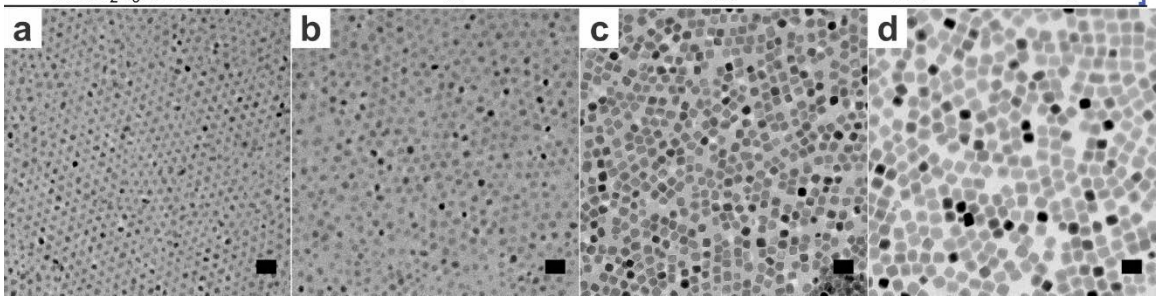

Figure 3.6. SAXS data from ITO/In_2O_3 core/shell nanocrystals, with corresponding TEM images. The table displays the particle size and size dispersion from SAXS. By TEM, all nanocrystal sizes have a sub-10% size distribution. The slightly higher percent polydispersity found by SAXS is likely the result of differing degrees of shape anisotropy in the sample. Because SAXS is a scattering based method of analysis, small shape anisotropies can contribute to a larger modeled polydispersity. Dopant-induced shape modulation is commonly reported in literature, and anisotropies could be caused from dopant-induced crystallographic disorder or changes in ligand bonding. All scale bars are 20 nm.

X-ray photoelectron spectroscopy (XPS) was used to monitor shell growth and radial distribution of the tin atoms. Fig. 3.7a shows decreasing Sn 3d peaks as more indium precursor is added to the nanocrystals. The sampling depth (3λ) for the In and Sn 3d XPS peaks was calculated to be ~5 nm within the nanocrystal core.[40] Additional attenuation of these signals occurs in the ligand shell. As the In_2O_3 shell thickness increases from 0.6 – 3.3 nm, the intensity of the Sn 3d peaks steadily decrease, suggesting that the dopant (tin)

is being confined to the nanocrystal core as the In_2O_3 shell is grown. For the 12.8 nm ITO/In_2O_3 nanocrystals (Figs. 3.6d and 3.7, green trace) no Sn 3d peaks are present in the XPS spectrum, indicating the nanocrystal does not contain tin in the shell of the material. If tin were re-distributing itself in the nanocrystal homogeneously, one would expect a little over 1 at. % tin present, which is easily detectable in this measurement. Two other features of the XPS spectra support these conclusions. First, the In 3d peaks narrow as In_2O_3 is grown, suggesting that undoped In_2O_3 dominates the signal produced in the outer portions of the nanocrystals. Second, the systematic decreases in the baseline intensity at binding energies > 455 eV (attributed to inelastic scattering of In 3d photoelectrons) suggests that the depth sampled contains higher concentrations of indium sampled as the shell thickness increases.[41]

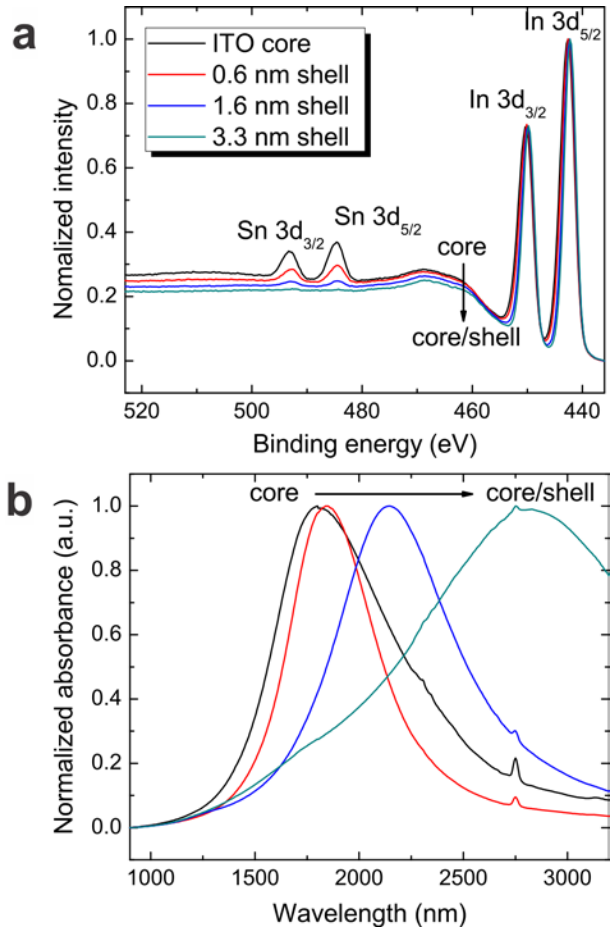

Figure. 3.7. XPS and NIR absorbance of ITO/In_2O_3 core/shell nanocrystals with varying thickness of In_2O_3. (a) The XPS spectra show a decreasing intensity of the Sn 3d peaks of the core, decreasing intensity of the inelastic binding region, and a smaller width of the In 3d peaks consistent with thicker In_2O_3 shells. (b) Near-infrared (NIR) spectra of ITO and core/shell nanocrystals display LSPR peaks that are shifted to longer wavelength as the concentration of tin in the crystal decreases, indicating a decreasing free electron concentration in the crystal.

We measured the near-infrared absorbance spectra of the core/shell nanocrystals to assess the role of dopant distribution on the optoelectronic properties of the nanocrystals. Heterovalently doped metal oxide nanocrystals have been identified as important non-noble metal plasmonic materials, which have been an area of recent active research.[42–44] The localized surface plasmon resonance (LSPR) of these materials can be tuned based on the free electron concentrations. In Fig. 3.7b, we find the LSPR red-shift with increasing shell (In_2O_3) thickness, as would be expected with decreasing Sn-dopant concentration.

The wavelength of the LSPR can be tuned over a range of more than 1,000 nm simply by increasing the thickness of the oxide shell. If In_2O_3 were not growing on the existing crystals and instead were nucleating independently, one would not observe the same red-shift of the LSPR, but would instead observe a superposition of ITO and In_2O_3 spectra.[45] This synthetic method has the potential to yield more information regarding the LSPR response to the dopant distribution within a nanocrystal as well as the degree of LSPR modulation.[46]

In an effort to evaluate the ease with which dopants can be intentionally placed in different radial positions in a nanocrystal, we aimed to synthesize In_2O_3/ITO/In_2O_3 core/shell/shell nanocrystals. First, 8.9 nm In_2O_3 nanocrystals were synthesized as described above. The reaction mixture was then stirred at synthesis temperature for three hours. SAXS analysis of aliquots taken over this time show no further growth or aggregation (Fig. A6). Next, a 90:10 In/Sn oleate mixture was slowly added to the reaction mixture, and the particles were grown to reach 10.4 nm. Finally, additional indium oleate was slowly injected to reach a final diameter of 13.6 nm (see Fig. A7 for TEM images). XPS spectra of aliquots taken for the In_2O_3 core, In_2O_3/ITO core/shell, and In_2O_3/ITO/In_2O_3 core/shell/shell nanocrystals are shown in Fig. 3.8. The Sn 3d peaks grow in upon addition of the ITO shell, and decrease after the In_2O_3 shell is added. The increase in the inelastic scattering of the In 3d photoelectrons increases upon ITO shell addition and decreases when the In_2O_3 shell is added, as expected if the dopant atoms are localized in the inner shell.

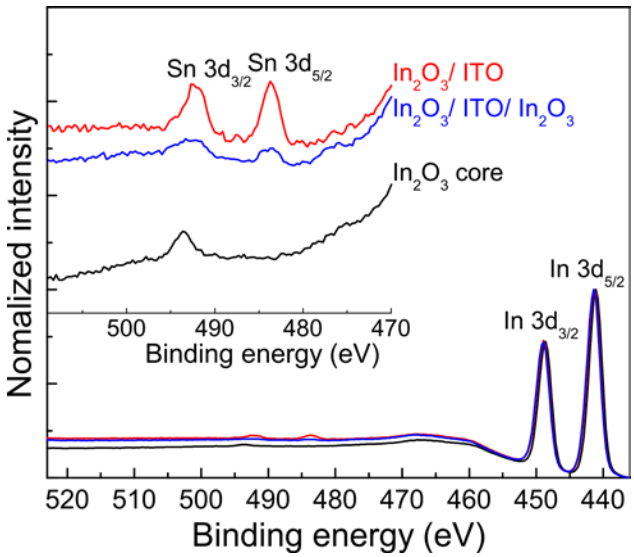

Figure. 3.8. XPS of In_2O_3 core, In_2O_3/ITO core/shell, and In_2O_3/ITO/In_2O_3 core/shell/shell nanocrystals. The core nanocrystals shows no presence of Sn 3d peaks (the peak at 494 in the spectrum of the core is a Na Auger peak from the mica substrate), while the core/shell and core/shell/shell nanocrystals show the presence of Sn. The decrease in the amplitude of the Sn 3d peaks and the decrease in inelastic scattering are both consistent with the core/shell/shell structure with the tin localized in the inner shell. Inset: zoomed-in view of the Sn 3d peaks between 510 and 470 eV.

Conclusion

We have demonstrated sub-nanometer control of core size and dopant distribution in indium oxide and tin-doped indium oxide nanocrystals *via* a slow-injection synthetic method. Rapid esterification, rather than thermal decomposition, produces reactive species that condense with active hydroxyl groups on the nanocrystal surface leading to continuous, controlled growth. The reactivity of the surface hydroxyl groups is important because if they become passivated, nucleation of new nanocrystals occurs rather than the growth of the existing cores. The method possesses several of the beneficial attributes of living growth processes common in polymer chemistry: (i) the number of growing nanocrystals remains constant, (ii) the size distribution of the nanocrystal cores remains low throughout the process, (iii) the molecular weight of the nanocrystal core scales

linearly with the amount of precursor added and (iv) the growth can be stopped and restarted making it convenient to grow shells of differing compositions.

This approach allows the synthesis of rationally-designed core/shell materials with predictable dopant densities and desired shell and core sizes. We utilized this method to synthesize ITO/In_2O_3 core/shell nanocrystals, as well as In_2O_3/ITO/In_2O_3 core/shell/shell nanocrystals. The similar reactivities of the matrix and dopant precursors under esterification conditions means that dopant concentration is easily controlled through the ratio of precursors used. Under the conditions employed for synthesis, dopants don't redistribute throughout the nanocrystals. Convenient access to semiconductor nanocrystals with deliberately controlled radial distributions of dopant ions will permit studies to probe how such distributions influence the optical and electronic properties of these materials.

Slow-injection syntheses that produce reactive species through controlled reactions, (such as the esterification process described here), hold promise to produce a wide range of mixed metal oxide and doped metal oxide nanocrystals with desired dimensions and composition profiles. Chemistries that generate a reactive nanocrystal surface and produce controlled mixtures of reactive species that condense with the surface groups would, more generally, allow more controlled syntheses of nanocrystals with specific overall or local compositions. Such methods would serve as a springboard for the development of other types of nanomaterials, in addition to oxide nanocrystals.

Materials and Methods

Materials

Indium(III) acetate (99.99%), oleic acid (90% technical grade), tin(IV) acetate, and trimethoxy(octadecyl)silane (90% technical grade) were purchased from Sigma-Aldrich and used as received. Oleyl alcohol (80-85% technical grade) was purchased from Alfa Aesar and used as received. A flow meter purchased from Cole-Parmer was used to monitor nitrogen flow (model 03216-10).

Characterization of Indium Oxide Nanocrystals

Small-angle X-ray scattering (SAXS) analysis was done on a lab-scale SAXS (SAXSess, Anton Paar, Austria). The system was attached to an X-ray generator equipped with a X-ray tube (Cu Kα X-rays with wavelength $\lambda = 0.154$ nm) operating at 40 kV and 50 mA. The scattered X-ray intensities were measured with a charge-coupled device (CCD) detector (Roper Scientific, Germany). The raw data was processed with SAXSquant software (version 2.0). Scattering curves were averaged over 50 individual curves for various acquisition times (2-40s). Curve fitting was done using Irena macros for IGOR (V. 6.3).[33] Select samples were analyzed with a NIST SANS data reduction software.[47] The SAXS was calibrated to absolute intensity using 18.2 MΩ water as a standard, and all data was normalized to the same exposure time. The number of scatterers were calculated dividing the volume fraction by the volume of one particle. We were concerned that a SAXS model generated from a spherical form factor might produce inaccuracies because particle shapes ranged from truncated cubic to cuboctahedral. However, generated SAXS patterns will be directly proportional to a nanocrystals' core volume, and when the

appropriate form factor is used to for analysis, we find negligible (< 5%) differences in the modeled volume.

Transmission electron microscopy **(**TEM) images and electron diffraction patterns were collected on 400 mesh Cu grids (Ted Pella, Redding, CA) using a Tecnai Spirit TEM (FEI, Hillsboro, OR) operating at 120 kV equipped with a Bruker EDS detector. HRTEM images were collected on a 300 kV C_s image corrected FEI Titan (S)TEM. Samples were prepared by drop-casting a toluene solution directly onto a copper grid, or by dipping the grid into a dilute solution of particles. Images were analyzed using ImageJ software, and following procedures outlined in literature.[48] Over 300 nanoparticles were measured for each data point.

X-ray photoelectron spectroscopy (XPS) was acquired using a Thermo Scientific ESCALAB 250 X-ray photoelectron spectrometer using monochromatic Al Kα X-ray source at 20 kV. 20 scans were collected on each sample over a binding energy of 436-523 eV to observe the In and Sn 3d peaks. Samples were prepared by drop-casting a hexane solution of nanocrystals on mica substrates.

NIR absorbance measurements were collected on a PerkinElmer Lambda 1050 UV/Vis/NIR spectrometer. Samples were prepared at concentrations of 0.5 mg/mL in carbon tetrachloride.

Synthesis of Indium Oxide Nanocrystals

Indium(III) acetate (2.198 g, 7.5 mmol) was added to 15 mL oleic acid and kept at 150 ^{o}C for several hours under N_2 to produce an indium oleate solution with a concentration of 0.5 mmol indium/mL oleic acid. The indium oleate solution obtained was then added dropwise to 13.0 mL of oleyl alcohol heated to 290 ^{o}C in a 100.0 mL three-neck flask. The metal oleate solution was added using a 20 mL syringe and syringe pump at a rate of 0.35 mL/min. During addition, N_2 was flowing through the flask at a rate of 130 cc/min. All three necks of the flask were capped with septa, and three 16-gauge purge needles were placed in one of the necks to prevent pressure buildup. A small amount of kimwipe® was placed in the purge needles to prevent solvent loss.

For the synthesis of larger nanocrystals, the presence of more than 13.0 mL oleyl alcohol was necessary to continue esterification and growth the nanocrystals. After the addition of 10 mL indium oleate solution, the syringe of indium oleate was removed and 10 mL of oleyl alcohol was added dropwise at a rate of 0.2 mL/min. Once the alcohol was added, additional metal oleate precursor was added at 0.35 mL/min. The cycle continued once more (see supplementary information Figure 3.2) for the synthesis of 22 nm particles.

To gain insight into the growth mechanism during the synthesis, 0.1 mL aliquots were taken from the reaction solution using a dry 1.0 mL glass syringe. Collection of the aliquot out of the hot reaction vessel rapidly cooled the solution and quenched particle growth. The nanocrystals were precipitated with 12 mL ethanol. The solid was collected by centrifugation at 7300 rpm and washed once more with 12 mL ethanol. After collection, the final nanocrystals were dissolved in toluene.

Termination of Surface Hydroxyl Groups with a Trialkoxysilane During In_2O_3 Growth

In_2O_3 nanocrystals were synthesized at 290 ^oC as described above to produce nanocrystals that are 10.4 nm by SAXS. At this point, the reaction mixture was cooled to room temperature. After the nanocrystals had settled to the bottom of the flask, ~8 mLs of the supernatant (oleyl alcohol and ester) were decanted. This reduces the amount of oleyl alcohol that is available to react with the silane reagent. The remaining nanocrystals were heated to 150 ^oC. 8 mLs of trimethoxy(octadecyl)silane was added dropwise (0.2 mL/min), and the reaction was then left at 150 ^oC for one hour. Next, the flask was cooled to room temperature and the original decanted solution was added back to the flask. The contents of the flask were then re-heated to 290 ^oC. An aliquot was taken at this point for analysis.

To investigate the effects of the silane treatment, an additional 0.5 mmol metal precursor was added to the nanocrystals under synthesis conditions. A second aliquot was taken at this point (Fig. 3.4b).

As a control to evaluate the growth in the absence of silane, the same experimental procedure described above was performed without addition of trimethoxy(octadecyl)silane. That product is shown in Fig. 3.4c.

Each aliquot was precipitated with 12 mL ethanol. The solid was collected by centrifugation at 7300 rpm and washed once more with 12 mL ethanol. Final nanocrystals were dispersed in hexanes for SAXS analysis and deposited on a TEM grid for imaging.

Synthesis of ITO/In_2O_3 Core/shell nanocrystal

The synthesis is very similar to that described above, using the same reaction temperature and nitrogen flow rate. Indium oleate precursor was previously prepared by mixing indium acetate and oleic acid as described above. In a different vial, a 10% Sn-doped indium

oleate solution (ITO precursor) was prepared by mixing tin(IV) acetate and indium(III) acetate in a 1:9 molar ratio. Oleic acid was added to yield a final solution with a concentration of 0.5 mmol/mL oleic acid. Both precursor solutions were left at 150 ^{o}C for several hour under N_2.

The ITO precursor solution was first added dropwise into 13.0 mL of oleyl alcohol at 290 ^{o}C using a 20.0 mL syringe and syringe pump at a rate of 0.35 mL/min. An aliquot of the solution was collected at this point.

After growth of the ITO cores, the ITO precursor syringe was removed from the syringe pump and replaced with a syringe filled with the indium oleate precursor. As described above, the precursor was added to the flask using a 20.0 mL syringe and syringe pump at a rate of 0.35 mL/min. Aliquots were taken after the addition of 0.5, 1.0, and 2.0 mmol of indium precursor was added. All aliquots were precipitated twice with 12 mL ethanol, collected by centrifugation, and dissolved in hexanes.

Synthesis of In_2O_3/ITO/In_2O_3 core/shell nanocrystals.

The synthesis is very similar to that described above, using the same reaction temperature and nitrogen flow rate. Indium oleate precursor was previously prepared by mixing indium acetate and oleic acid as described above. In a different vial, a 10% Sn-doped indium oleate solution (ITO precursor) was prepared by mixing tin(IV) acetate and indium(III) acetate in a 1:9 molar ratio. Oleic acid was added to yield a final solution with a concentration of 0.5 mmol/mL oleic acid. Both precursor solutions were left at 150 ^{o}C for several hour under N_2.

The indium precursor solution was first added dropwise into 13.0 mL of oleyl alcohol at 290 ^{o}C using a 20.0 mL syringe and syringe pump at a rate of 0.35 mL/min to grow 8.9 nm

indium oxide nanocrystals. The nanocrystals were then left in the reaction solution at 290 ^{o}C for three hours (SAXS data shown in Fig. A6). After three hours, the ITO precursor was added dropwise into the reaction solution at a rate of .35 mL/min, until the nanocrystals reached 10.4 nm. An aliquot was taken after this addition for TEM and XPS analysis. Subsequently, the same indium oleate precursor described above was slowly added (0.35 mL/min) into the reaction solution to yield nanocrystals with a final core size of 13.6 nm. XPS spectra from these particles are shown in Fig. 3.8, TEM images of the In_2O_3 core, In_2O_3/ITO core/shell, and In_2O_3/ITO/In_2O_3 core/shell/shell nanocrystals can be found in Fig. A7.

Bridge to Chapter IV

Chapter III showcased the fine core size control possible via the slow addition of metal carboxylates into oleyl alcohol. Chapter IV highlights how utilization of the slow addition approach results in fine control of core composition. Many exciting properties that arise in semiconducting and oxide nanocrystals are due to the incorporation of dopant cations into specific crystal structures, as demonstrated above with ITO nanocrystals. While doping methods are now well developed for bulk structures, incorporating dopants into nanocrystals is much more challenging. Often, syntheses for doped structures must be optimized by careful selection of host and dopant precursors and reaction conditions to form a doped product. Syntheses are rarely applicable for a large variety of dopants, and thus rigorous optimization is required for each new desired composition. Further, nominal dopant concentrations in precursors do not end up in the final isolated nanocrystal, a measure of “doping efficacy,” making the production of precision nanomaterials extremely difficult. Even if a doped nanostructure is produced,

uncontrollable and subtle structural differences in the particle, like the radial location of dopants, may have unintentional and detrimental consequences.

In chapter IV we show that using the slow addition, living approach allows dopant incorporation for a wide variety of transition-metal dopants at large, near thermodynamically allowed dopant concentrations (as high as 20 atomic %), and with extremely high doping efficacy (> 90% for most guest cations). Further, because the method utilizes the layer-by-layer growth of oxide nanomaterials with controlled composition in each layer, incorporated dopant cations are homogeneously distributed throughout the nanocrystal. The chapter demonstrates that living approaches can provide access to novel doped nanocrystals wherein the electronic, catalytic, magnetic, and optoelectronic properties can be controlled with unprecedented precision simply by the precursor feed ratios, and with little-to-no precursor optimization. This greatly decreases the synthetic burden required to produce doped compositions, and will pave the way for future discovery and optimization of dopant-induced properties.

CHAPTER IV

TRANSITION METAL-DOPED METAL OXIDE NANOCRYSTALS: EFFICIENT SUBSTITUTIONAL DOPING THROUGH A CONTINUOUS GROWTH PROCESS

This chapter was previously published as Jansons, A. W.; Koskela, K. M.; Crockett, B. M.; Hutchison, J. E. Transition Metal-Doped Metal Oxide Nanocrystals: Efficient Substitutional Doping Through a Continuous Growth Process. *Chem. Mater.* **2017**, *29* (19), 8167–8176.

Introduction

The intentional introduction of defects into host structures is the foundation for useful properties that are utilized today in many important applications. This approach has long been used in bulk materials to alter the electronic, magnetic, and physical structure of semiconductors,[1,2] and is essential to the modern microelectronics industry. Similarly in nanocrystals, the introduction of defects through dopant incorporation imparts interesting properties that we are beginning to understand and harness in applications.[3–6] Exciting recent discoveries of magnetic,[7–12] luminescent,[13–21] catalytic,[22–24] and optoelectronic[25–31] properties of nanocrystals have been investigated as a result of nanocrystal doping. These properties can be further enhanced if advanced synthetic strategies are developed.[32,33]

While many synthetic approaches for the production of doped oxide nanocrystals have been established,[34–45] several challenges remain. Producing doped nanocrystals with precise control of nanocrystal size, composition, and internal structure remains a large

barrier to broader adoption and further technological advancement.[4] Doped nanocrystals are notorious for "self-purification," i.e., the exclusion of dopants from the host lattice—an argument that is often justified by considering the thermodynamics of impurity formation.[46,47] Thermodynamics are also cited when considering that dopant incorporation levels in nanocrystals have traditionally been well below the solid solubility limits found in bulk analogs and rarely contain > 10 atomic % dopant. The argument falls short however, when considering that kinetics rather than thermodynamics controls this process at the nanoscale.[48,49] It is widely believed that substitutional doping can only be obtained if dopants can find their way onto the surface of the nanocrystal for long enough that they become surrounded by host monomer overgrowth.[46,48,50,51] Thus, consideration of the nanocrystal surface chemistry—including size, shape, ligands, and functional groups—becomes extremely important for effective dopant incorporation.

In the many cases where kinetics controls the efficacy of dopant incorporation, considering both host and dopant precursor reactivity is critical for doped product formation.[50] If a balance between reaction rates is not met and the host precursor forms reactive monomer faster than dopant precursor, then dopant incorporation could be low or absent. Conversely, if dopant precursor formation kinetics are faster than the host, new crystal phases are produced that contain primarily the dopant element. Even if conditions are favorable for uniform doping at nucleation, dopant incorporation is known to be dependent on specific crystal facets and/or ligand environment,[49] which may not be constant as crystal growth continues. Therefore, the majority of doped-nanocrystal synthetic methods attempt to obtain this balance through careful, and often tedious, trial

and error selection of precursors and synthetic conditions in order to match precursor reactivity rates and subsequently form a substitutionally-doped nanocrystal.

Production of a doped structure, however, is not the final measure of success. Different synthetic methods can produce equivalent composition yet yield nanocrystals with undesirable variations in radial dopant locations. These small structural differences may drastically affect properties.[52,53] In addition, some synthetic methods give rise to large variations in the number of dopants per nanocrystal within an ensemble, beyond that predicted by Poisson statistics.[54] Here again, variations in composition can drastically influence the desired properties.[32] Besides composition and structure, control of nanocrystal size becomes an additional challenge because the properties of nanomaterials are size dependent. Synthetic approaches are usually developed to control size or produce a desired composition but generally not both. This is because the introduction of dopants disrupts the thermodynamics of nucleation,[54] making it difficult to control both dopant incorporation and size with desired precision.

Exploration of new synthetic approaches to doped nanocrystals to complement rapid-injection or thermal decomposition reactions may be valuable given the significant challenges in producing and controlling the composition, structure, and size. Rather than precipitation reactions, which trap dopants in a crystalline matrix, we hypothesized that the use of reactive surface functional groups could facilitate the incorporation of transition metal dopants into a host oxide lattice. An ideal synthetic method would allow the layer-by-layer growth of nanomaterials with precise control over the composition in each layer, thus allowing enhanced control over both overall nanocrystal composition and radial structure. Ideally, such a method would be amenable to a wide variety of dopants, and

would facilitate the predictable incorporation of dopants at levels near thermodynamically-predicted solid solubilities.

A number of authors have highlighted the need to carefully choose the right precursors (often a metal alkylcarboxylate) to effectively form the desired doped product.[40,50,55] Without the appropriate precursors, host and dopant precursors reactivities may not be sufficiently matched. We thought that using a slower, layer-by-layer nanocrystal growth process would facilitate more even incorporation of dopant atoms while preventing coalescence or ripening.[56,57] Thus, carefully choosing metal precursors may not be necessary, and for this reason we chose to simply use metal oleates for both host and dopant precursors. Further, the slow addition of precursor allows particle growth to occur with constant concentration of dopant in each added layer, ensuring that dopant atoms are homogeneously distributed radially throughout the structure.

Herein we report the synthesis of substitutionally doped Mn, Fe, Co, Cu, and Zn-doped In_2O_3 nanocrystals at 5, 10, and 20 atomic percent. We find that dopant incorporation efficacy is nearly quantitative, which allows the logical preparation of highly-doped nanocrystaline structures. With the exception of the Cu-doped nanocrystals, which we found to temporarily incorporate into the oxide lattice before surface segregation, the dopant cations are homogeneously-distributed throughout the nanocrystal without surface or core localization. As a wide bandgap oxide, In_2O_3 allows ligand field transitions to be observed in visible energies, allowing one to probe the optical properties resulting from doping. The observed electronic transitions of first row transition metal dopants in the In_2O_3 structure indicate that dopants lie in octahedral geometries, which is consistent with substitutional incorporation of the cations. The slow, controlled growth of oxide

nanocrystals made possible by this synthetic method makes it possible to precisely control the internal nanocrystal structure and composition.

Results and Discussion

An alternative approach to traditional thermal decomposition reactions are the use of so called nonaqueous sol-gel reactions to synthesize doped oxide nanocrystals.[27,35,37,40,41,50,55,58,59] These reactions rely on predictable principles from organic chemistry to arrive at reactive monomer.[60] Using an esterification-based mechanism, we recently showed that a variety of binary oxide nanocrystals, including In_2O_3, γ-Fe_2O_3, Mn_3O_4, CoO, and ZnO, could be obtained through the slow addition of metal carboxylate into long-chain alcohol at elevated temperatures.[59] Particle growth is facilitated by the production of reactive metal hydroxyl groups, which subsequently condense with hydroxyls on the particle surface. Because the method relies on metal-catalyzed esterification and not thermal decomposition, we thought this approach could be used to precisely control dopant incorporation into oxide nanocrystals simply by tuning precursor molar ratios. Further, we hypothesized that we may be able to access dopant concentrations higher than those typically reported for semiconducting nanocrystals, owing to the kinetic control provided by the living growth process. If this growth process supports continuous growth by both matrix and dopant precursors, we would expect dopant incorporation efficacies near 100%, well beyond those typically found for the production of doped oxide nanocrystals.

Previous studies using the slow-addition of metal carboxylates into oleyl alcohol had shown that the method is amenable to the production of Sn-doped In_2O_3 (ITO) nanocrystals with very high dopant efficacies, and produced nanocrystal product in high

yield.[53,56,59] Because Sn and In are similar in size and reactivity, synthesizing ITO with controlled composition was interesting, but not surprising. We sought to investigate the incorporation of transition metal cations to determine how differing sizes of cations influence their incorporation into the oxide lattice..

Using In_2O_3 as a model oxide system, we synthesized Mn: In_2O_3, Fe: In_2O_3, Co: In_2O_3, Cu: In_2O_3, and Zn: In_2O_3 nanocrystals at nominal dopant concentrations of 5, 10, and 20 atomic %. Indium oxide was chosen as an appropriate model system because of its importance as a transparent electrode,[61] its emergence as a model system for the study of unique optoelectronic properties including near-IR localized surface plasmon resonances (LSPRs),[62] and its role as a host material for dilute magnetic oxides.[63] During synthesis, we kept the total metal content in the precursor at one mmol as a convenient point of comparison. Synthesizing larger particle sizes with sub-nanometer precision and producing larger quantities of product is possible simply by adding more precursor.[53,56] The transition metal dopants used have a range in effective ionic radii from 69 pm (for octahedrally coordinated Fe^{3+}) to 88 pm (for Zn^{2+}),[64] allowing us to probe the influence of cation size on dopant incorporation efficacy. The radius of In^{3+} in the In_2O_3 host matrix is 94 pm.[64]

After the addition of the metal oleate precursor, nanocrystals were purified by multiple precipitations with an anti-solvent (ethanol) and collected by centrifugation. No size selection processes were used. Size, size dispersion, and shape were determined by small-angle X-ray scattering (SAXS) and transmission electron microscopy (TEM). Figure 4.1 displays TEM images of the doped nanocrystals at each dopant concentration. SAXS results (Table 4.1) corroborate nanocrystal size and size dispersion data from TEM. Several

anticipated outcomes become apparent from these data. First, the presence of a dopant cation influences the mean size of nanocrystal produced based upon the addition of one mmol of total metal (host + dopant) precursor. Compared to undoped In_2O_3 nanocrystals, the addition of dopant cations produce a smaller mean size of nanocrystals, with higher dopant concentration in the precursor leading to a further decrease in the mean size of the product. The influence of dopant cations on the driving force for homogeneous nucleation has been discussed,[54] and a similar trend in mean size with the presence of dopants has been observed.[65] As expected, more dopant cations on the surface of the nanocrystal leads to a slower initial growth rate of the initial formed nuclei allowing new nucleation to occur. Previous authors have similarly attributed the change in doped nanocrystal size to a thermodynamic barrier of growth onto doped nanocrystals because surface dopants modify the surface energy of the nanocrystal.[65,66] Eventually, with the accumulation of more monomer and now more nuclei in solution, growth can continue on the doped particles.

Increasing the dopant content in the precursor also increases the shape anisotropy of the formed nanocrystals, which is reflected in the polydispersity measurements by SAXS shown in Table 4.1. Since only metal oleates and oleyl alcohol are present in each of the reaction mixtures, we can confirm that shape changes are only due to the dopant cations and not additional coordinating reagents or changes in reaction conditions. Nanocrystal shape changes with dopant addition are well documented in literature,[27,41,50,67] and it is possible that dopants may alter the ligand-metal binding energies as well alter the surface energies of specific crystallographic facets, leading to anisotropic growth. Unraveling the precise mechanism with which the dopants lead to the varying morphologies is beyond the scope of this work. However, it is worth pointing out that while some dopants, like Fe,

seem to only slightly change the particle morphology, other dopants, like Mn and Co, drastically alter size and shape of the formed nanocrystals at higher concentration.

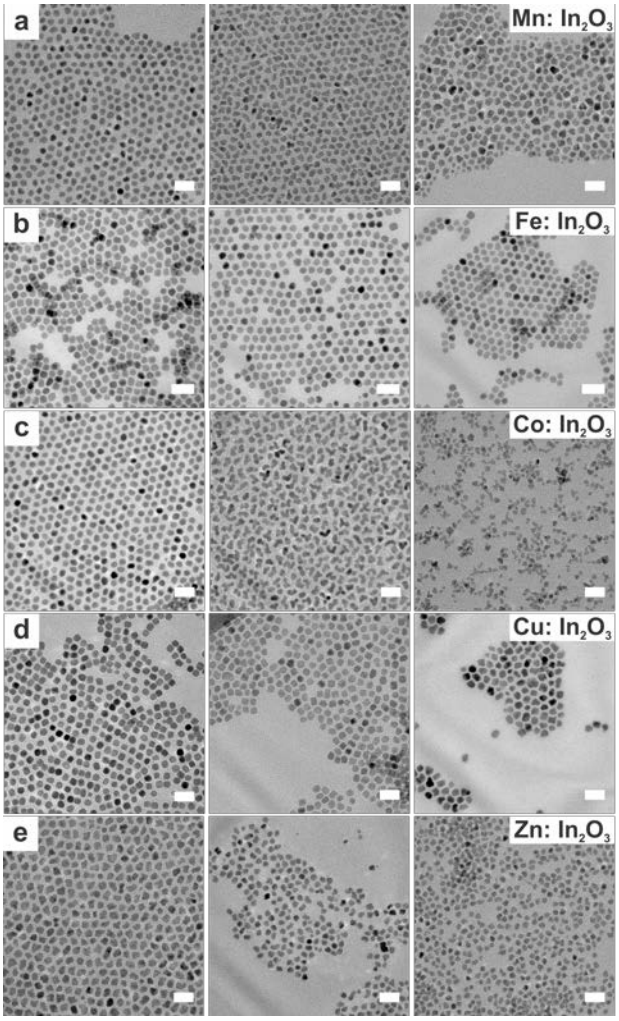

Figure 4.1. TEM images taken of doped In_2O_3 nanocrystals at varying molar dopant ratios. Scale bars are 20 nm. The nominal dopant percent in the precursor increases from left to right, 5% dopant on the left, 10% center, and 20% right. Panel **a**) displays Mn: In_2O_3, **b**) Fe: In_2O_3, **c**) Co: In_2O_3, **d**) Cu: In_2O_3, and **e**) Zn: In_2O_3

Table 4.1. Doped nanocrystal size and size dispersion from SAXS.

Dopant	*Nominal dopant % in precursor*	*Size (nm)*	*% Polydispersity*
undoped In_2O_3	0	8.2	10.7
Mn	5	7.3	12.0
Mn	10	6.3	17.5
Mn	20	5.0	27.1
Fe	5	7.4	12.3
Fe	10	7.1	12.2
Fe	20	6.0	14.8
Co	5	7.2	10.1
Co	10	6.6	32.5
Co	20	4.8	41.5
Cu	5	7.9	9.9
Cu	10	7.9	10.6
Cu	20	7.2	14.5
Zn	5	7.5	16.1
Zn	10	6.1	14.1
Zn	20	5.8	14.6

The compositions of the nanocrystals were determined by inductively coupled plasma optical emission spectroscopy (ICP-OES). After purification, the nanocrystals were dissolved in nitric acid and diluted for elemental analysis. Table 4.2 compares the precise nominal dopant concentration in the added precursor with the dopant concentration found in the purified nanocrystals. As displayed, most dopants incorporate with > 90% efficacy, even at dopant concentrations as high as 20%. Interestingly, in many of the higher doped samples, efficacies surpass 100%, indicating that indium monomer is disproportionally excluded from the growing nanocrystals. For the Cu: In_2O_3 nanocrystals, the efficacy of incorporation of the dopant is much lower compared to the other dopants. We will discuss the copper samples separately later in this discussion.

Table 4.2. Dopant concentrations in purified nanocrystals compared to the precursor composition, and the resulting dopant incorporation efficacy.

Dopant	*Precise nominal dopant concentration (atomic %)*	*Nanocrystal dopant concentration (atomic %, ICP-OES)**	*Dopant incorporation efficacy (%)*
Mn	4.9	4.8	98
Mn	9.8	9.0	92
Mn	20.2	21.3	105
Fe	5.1	4.9	96
Fe	9.9	9.1	92
Fe	19.8	20.4	103
Co	5.4	4.9	91
Co	10.4	10.1	97
Co	20.3	20.8	102
Cu	5.2	4.8	92
Cu	10.9	7.3	67
Cu	20.4	15.6	76
Zn	6.0	5.9	98
Zn	12.3	11.5	93
Zn	20.5	19.9	97

*Concentrations determined by ICP-OES have standard deviations of ≤ 0.05 atomic %

We also utilized X-ray photoelectron spectroscopy (XPS) on selected doped samples to complement the measurements carried out with ICP-OES (see Figure B1 for example XPS spectra). XPS yields elemental information from the surface of the nanocrystals. At the binding energies investigated, XPS samples a depth of ~3 nm in In_2O_3.[68] This sampling depth does not take into account the organic ligand shell, but scattering of signal due to the organic ligands is less than the inorganic core. Using XPS, along with complementary elemental analysis by ICP-OES, allows one to probe the radial distribution of dopant atoms in the nanocrystal, which is a small yet extremely important detail that is often overlooked in the characterization of doped nanocrystals. We integrated the In $3d_{5/2}$ peaks and the transition metal dopant $2p_{3/2}$ peaks to assess the dopant concentration near the nanocrystal

surface. The fact that the values for dopant concentration found near the surface (by XPS) match those found for bulk measurements (by ICP-OES) (Table 4.3) suggests that dopants are homogeneously distributed throughout the nanocrystal, and not surface segregated. We could not obtain accurate elemental information by XPS from the Fe: In_2O_3 samples, as the Fe 2p peaks, which have the highest sensitivity factor, are buried by a large In 3p loss feature. The Fe 3p peaks do not have a sensitivity factor high enough to accurately quantify Fe content on the surface. In some cases where the nanocrystals are small (< 6 nm), it may be possible that XPS is sampling more than half the nanocrystal. In this case, the combination of ICP-OES and XPS might not appropriately assess the radial dopant position and both techniques would yield similar compositions. While this is a possibility for some of the nanocrystals investigated in Table 4.3, it is apparent from the data for the largest nanocrystals that dopants are not segregating at the surface or forming amorphous clusters on the surface, as this scenario would lead to stronger dopant signal.

Table 4.3. Comparison of dopant concentrations in the purified nanocrystals by ICP-OES and XPS.

Dopant	*Nominal dopant concentration (atomic %)*	*Dopant atomic % (ICP-OES)*	*Dopant atomic % (XPS)**
Mn	9.8	9.0	9.6
Co	10.4	10.1	11.2
Zn	6.0	5.9	5.1
Zn	12.3	11.5	11.7
Zn	20.5	19.9	20.1

*Concentrations determined by XPS have a standard deviation of ≤ 0.2 atomic %

In order to confirm that the dopant atoms are substitutionally incorporating into the In_2O_3 lattice, we studied structural changes of the nanocrystals with X-ray diffraction (XRD). For all dopant cations at all concentrations investigated we found no evidence of secondary

phases or crystalline phases other than cubic bixbyite In_2O_3 (Figure 4.2). This finding contrasts with previous reports that identified the corundum-type crystal structure for doped In_2O_3 nanocrystals at certain dopant concentrations or crystal sizes.[69,70] Further inspection of the XRD patterns in Figure 4.2 reveals small shifts and changes in intensity for the diffraction peaks as the dopant concentration is increased. These variations are most evident in the (222), (400), and (440) reflections. The influence on the other diffraction peaks are harder to discern given the broadening due to small crystallite size. Increased broadening at higher dopant concentrations is the result of smaller crystallite sizes, confirmed by SAXS and TEM data (Figure 4.1 & Table 4.1).

Using Rietveld analysis[71] (Figure B2), we extracted the cubic lattice constant *a* for each of the doped nanocrystal samples. Figure 4.3 plots the extracted lattice constants as a function of dopant concentration found by ICP-OES. The lattice constant of the undoped In_2O_3 nanocrystals matches that of bulk In_2O_3, both 10.117 Å (JCPDS no. 06-0416). As displayed in Figure 4.3, the lattice constant decreases for all samples with incorporated dopant, and further decreases with additional dopant presence, as expected by Vegard's law.[72] Furthermore, the difference in slopes for each dopant qualitatively matches the expected trend when comparing octahedrally coordinated ionic radii of the specific cations used as precursors. From the literature,[64] we find the trend in octahedrally coordinated ionic radii of cations: Fe^{3+} (69 pm) < Co^{2+} (79 pm) < Mn^{2+} (81 pm) < Zn^{2+} (88 pm) < In^{3+} (94 pm). It has previously been shown in oxide nanocrystals that a decreasing crystallite size leads to an increase in the crystalline lattice constant.[73] The fact that we observe a *decreased* lattice constant (Figure 4.3) despite the decreasing crystallite size for doped

products (Figure 4.1 and Table 4.1) strongly suggests that the cations are substitutionally doping for In^{3+} cations.

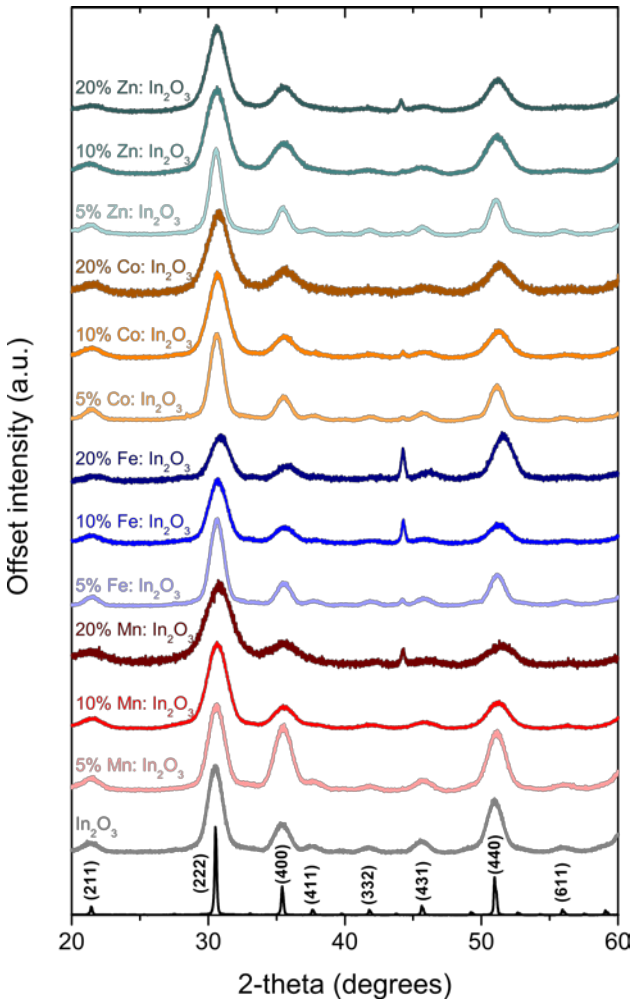

Figure 4.2. X-ray diffraction patterns of bulk (black, bottom trace), undoped (grey trace), and Mn, Fe, Co, and Zn doped indium oxide nanocrystals at 5, 10, and 20% dopant concentrations. The peak present at 43.5 ^{o} in some samples is due to the silicon substrate.

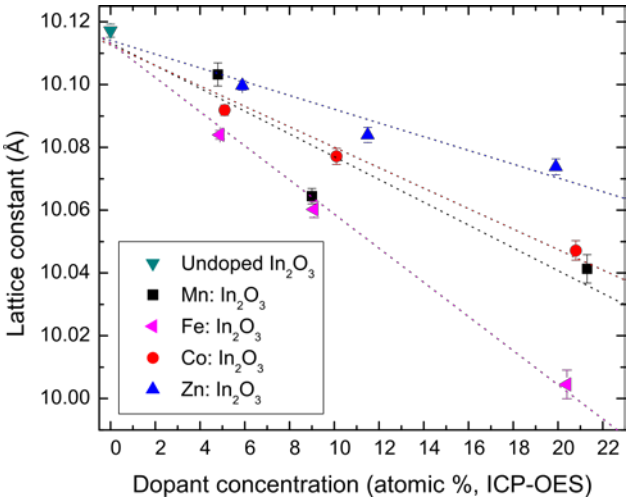

Figure 4.3. Lattice constants extracted through Reitveld analysis for doped and undoped nanocrystals plotted as a function of dopant concentration from ICP-OES. Predics decreases in lattice constant as a function of increased dopant incorporation suggest substitutional doping in the oxide nanocrystals.

Further evidence of substitutional doping can be found from electronic absorption spectroscopy. Figure 4.4 displays the absorbance spectra for the 10% doped nanocrystals at two concentrations. Spectra collected at low concentration (~0.05 mg/mL) make it possible to observe the band-edge absorption. Spectra collected at higher concentration (~10 mg/mL) can be used to identify ligand field transitions of the octahedrally coordinated metal centers. In the bixbyite structure, In^{3+} resides in two distinct six-coordinated sites within the lattice, the *b* and *d* sites.[39,70,74] Dopants with cation radii smaller than In^{3+} are thought to reside in the distorted octahedral *d* sites, with C_2 point group symmetry.[70,75] A solution of Mn: In_2O_3 nanocrystals suspended in hexanes at room temperature (Figure 4.4b) gives rise to a pink/red color, which, at first appearance, is characteristic of octahedrally coordinated Mn^{2+} complexes.[76] However, it is more likely these transitions arise from spin-allowed $^5E_g \rightarrow {}^5T_{2g}$ transitions of Mn^{3+}, as previously reported and discussed from a separate synthesis of Mn: In_2O_3 nanocrystals by Radovanovic *et al.*[70] The electronic spectra reported in their study qualitatively match the spectrum in Figure 4.4b.

They assigned this transition to a d^4 ion in a rhombic environment (which, as they point out, is structurally similar to the *d* site of a bixbyite lattice). In this environment, T_{2g} and E_g terms split further into A and B terms.[70,76] Given these considerations and previously discussed spectra,[70] we can assign the peaks at ~18,000 cm^{-1}, ~20,000 cm^{-1}, and ~22,000 cm^{-1} to the $^5B_g \rightarrow {}^5A_g$, $^5B_g \rightarrow {}^5B_g$, and $^5B_g \rightarrow {}^5A_g$ transitions, respectively. Figure 4.3f shows solutions of the 5, 10, and 20% Mn: In_2O_3 nanocrystals at the same concentration by mass (5 mg/mL), displaying the increasing intensity of the absorbance for the charge transfer and d-d transitions as the dopant concentration is increased.

Octahedrally coordinated Fe^{3+} cations generally exhibit much weaker d-d transitions than other d^5 systems, and therefore are not expected to appear in the absorbance spectrum shown in Figure 4.4c.[76] A previously reported synthesis and characterization of Fe: In_2O_3 nanocrystals assigns a similar peak at ~21,000 cm^{-1} to ligand-to-metal charge transfer transitions.[77] Elsewhere, Fe-doped In_2O_3 nanocrystals produced by a colloidal synthesis[78] were reported to have a color that qualitatively matches that of the solution in Figure 4.3c; however, no electronic absorbance data were reported. The absorbance spectrum of Co: In_2O_3 is displayed in Figure 4.4d. The broad absorption is similarly likely due to ligand-to-metal charge transfer. Comparing the spectrum in Figure 4.4d to previously reported Co^{2+} pseudooctahedral complexes,[76] a possible $^4T_{1g} \rightarrow {}^4T_{1g}(P)$ transition may be present at ~18,000 cm^{-1}. Co: In_2O_3 thin films showed similar absorption features, though their origin was not discussed.[79] As expected, undoped In_2O_3 (Figure 4.4a) and Zn: In_2O_3 (Figure 4.4e) do not give rise to any d-d transitions in the visible region (Zn^{2+} is a d^{10} metal center).

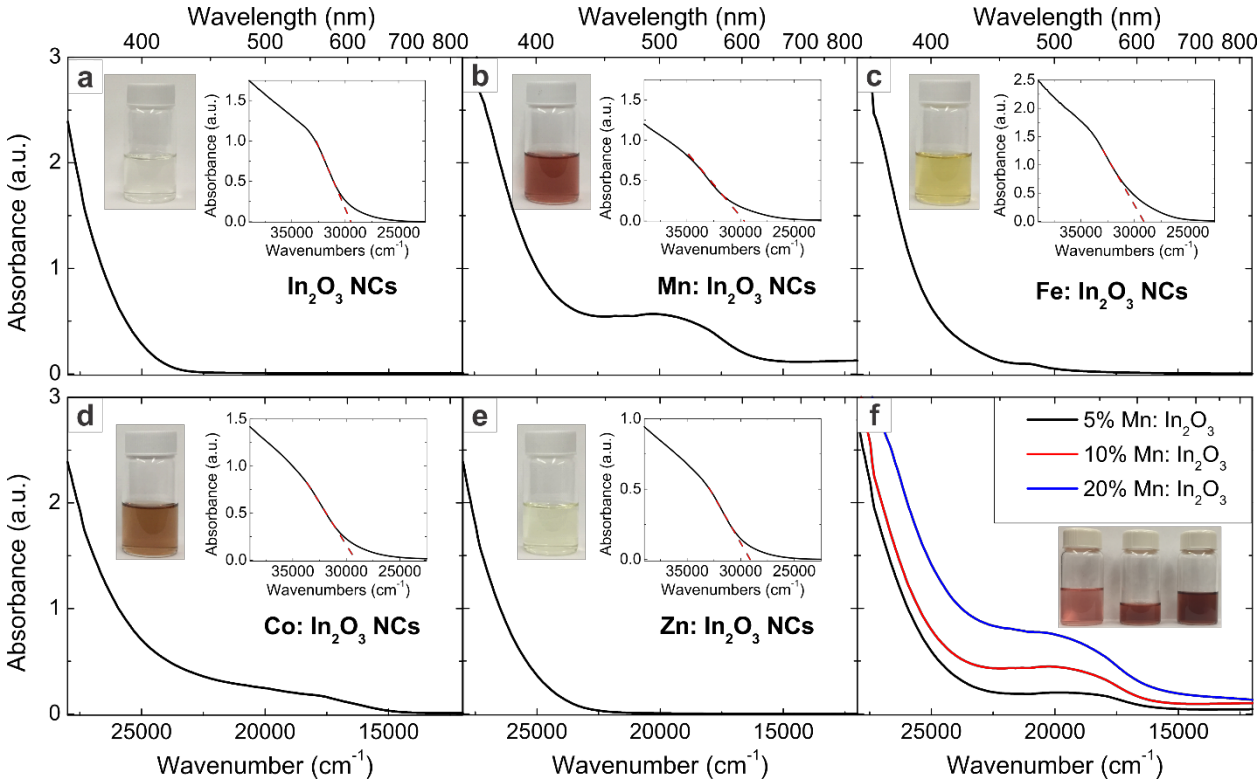

Figure 4.4. Electronic absorbance spectra collected on solutions of nanocrystals in hexanes at room temperature along with pictures of the solutions. Inset plots display spectra from dilute solutions (~0.05 mg/mL) of the nanocrystals that can be used to obtain band gap energy estimates. **a**) undoped In_2O_3 nanocrystals, **b**) Mn: In_2O_3, **c**) Fe: In_2O_3, **d**) Co: In_2O_3, and **e**) Zn: In_2O_3. **f**) absorbance spectra from solutions of 5, 10, and 20 atomic % doped Mn: In_2O_3 nanocrystals, all at constant concentration (5 mg/mL). The inset shows pictures of all three solutions, increasing in dopant concentration from left to right.

Band gap energies of doped and undoped In_2O_3 are estimated from absorption onsets from dilute solutions of nanocrystals shown in Figure 4.4. For undoped In_2O_3, absorbance onset occurs at ~29,500 cm^{-1}, corresponding to a band gap ~ 3.66 eV. Bixbyite In_2O_3 is commonly reported as having a bandgap between 3.5-3.7 eV.[80] All doped samples display a slightly red-shifted absorbance onset of ~29,000 cm^{-1} (~3.60 eV). The slight decrease in bandgap with doping has been attributed to donor states which arise within the band, likely from charge compensating oxygen vacancies.[79] The presence of dopant cations likely lowers the energy of vacancy formation.[81] A qualitative measure of oxygen vacancy content can be assessed by examining the near-infrared/infrared localized surface

plasmon resonance (LSPR) absorbance of the nanocrystals, which arise in oxide nanocrystals due to free carriers formed via doping, or in this case, oxygen vacancies.[25,31,82,83] The peak of the LSPR is directly proportional to the free electron content of the nanocrystals.[84] IR spectra (Figure B3) of undoped In_2O_3 displays a weak LSPR absorbance ~1,400 cm^{-1}, while the doped samples display a broader, more intense absorption centered at energies > 4,000 cm^{-1}. The shift in the LSPR to higher energy indicates a higher free electron concentration in the doped samples, a direct result of the larger concentration of vacancy defects. Fitting of the O1s XPS spectra (Figure B1) for 5 and 20% Zn: In_2O_3 samples results in a more prominent peak at 529.7 eV, suggesting a higher degree of oxygen deficient/defective oxide sites that increase as the dopant concentration increases. Notably, these defects have been shown to enhance some favorable properties, including sensitivity to oxidizing or reducing gases when these materials are used as the active component in gas sensors.[85–87]

As shown in Figure 4.1, the synthetic method also produced Cu: In_2O_3 nanocrystals. Copper ions have traditionally been difficult to dope within intrinsically n-type oxides,[88,89] and indium oxide has recently been shown to be an effective diffusion barrier to copper.[90] The fact that we were able to incorporate copper highlights the kinetic control possible with the slow addition method. After isolation of the Cu doped nanocrystals, however, we noticed some gradual changes in the properties of the material. Immediately after purification and dispersion of the synthesized nanocrystals in hexanes the color of the solution appeared dark red. One day after leaving the solution at room temperature, the solution color changed from red to a blue/grey, and gradually (over several days to ~ a week), changed to dark green (Figure 4.5a). The absorbance spectrum (Figure 4.5b)

initially displayed a single absorbance band at ~17,530 cm^{-1} that gradually shifts to lower energies as the solution color gradually turns green. Because the intensity of the peak in the spectra gradually decreases over time, a spectrum from a concentrated sample after two weeks is shown in the inset of Figure 4.5b, more clearly displaying the red-shifted peak at ~16,430 cm^{-1}. XRD patterns from the copper-doped samples (Figure 4.5c) display peaks consistent with the bixbyite In_2O_3 pattern. However, the peak intensities are irregular and accurate Rietveld refinements were difficult to obtain without significantly altering the occupancy of the unit cell. This is especially noticeable in the pattern two days after synthesis (Figure 4.5c, blue trace) that displays a (440) peak at 51^o that is large relative to the (222) peak at 30^o. A new pattern acquired on the same sample two weeks later shows expected relative intensities of the (222) and (440) peaks; however, refinements still resulted in a poor fit. From Braggs law, a qualitative understanding of the change in lattice constant can be found from the peak centers of the (222) and (440) peaks. Both peaks initially display peak centers shifted to higher 2-theta relative to undoped In_2O_3, consistent with a lattice contraction. Over time the peak centers shift to slightly smaller 2-theta, indicating a subsequent lattice expansion.

To account for the observed changes, we performed XPS on a sample immediately after synthesis and two days after synthesis. As displayed in Figure 4.5d, the surface of the freshly made nanocrystal displays almost no copper present, while two days later copper appears on the nanocrystal surface. No change in nanocrystal size or size dispersion was found via SAXS during this period. Taken collectively, the data suggest that the electronic and structural changes are due to copper ions diffusing from the center of the crystal to the surface. Copper is likely substitutionally doped for indium cations during

synthesis, given the lattice contraction in the XRD pattern, though the irregularities in the pattern suggest that the unit cell is not contracting symmetrically. Subsequent lattice expansion and appearance of copper in the XPS spectrum indicates that copper diffused through interstitial sites to the particle surface. Electronic absorbance spectra are consistent with a change in the coordination of the Cu^{2+} ions,[91] though the precise coordination is very difficult to accurately identify. Cu^{2+} is well known to take many distorted octahedral coordinations, and it is often difficult to assign to a specific stereochemistry based on the absorption energy.[76,92] To the best of our knowledge, very few reports of copper doped bixbyite structures have been published.[93] Copper diffusion has long been studied in bulk semiconductors, much less, however, in oxide nanomaterials.

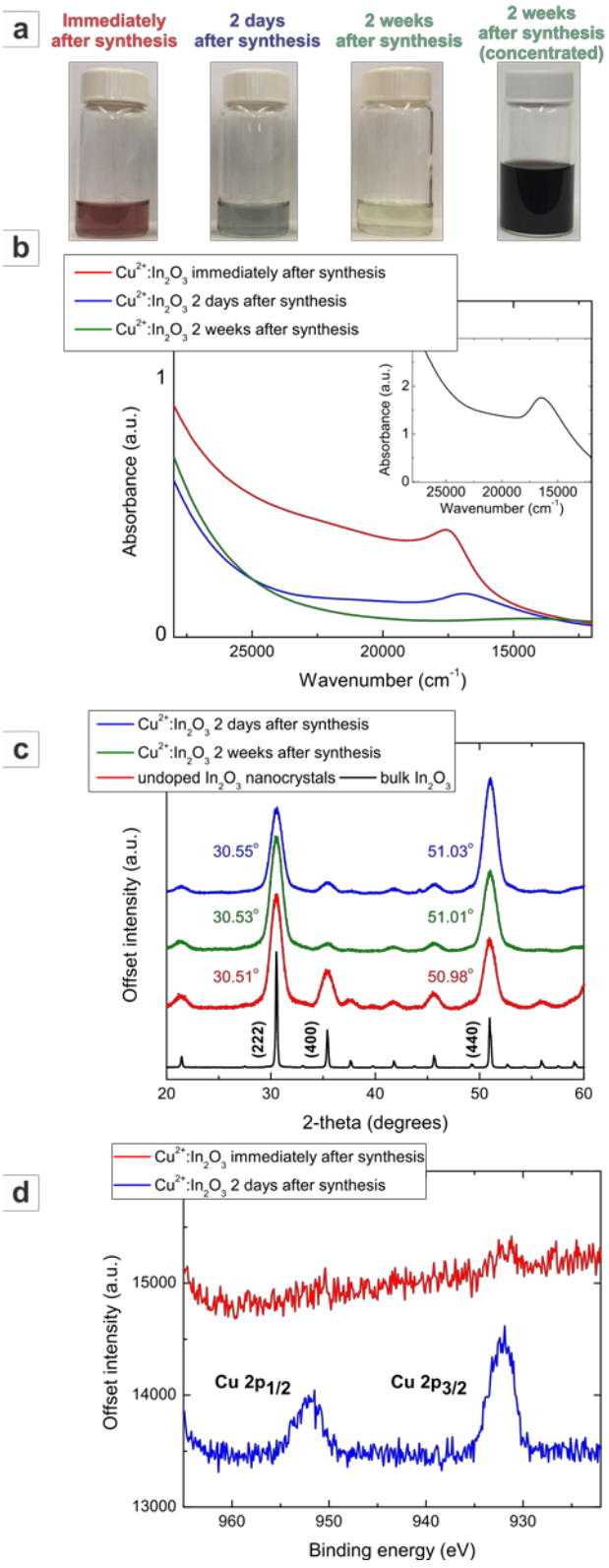

Figure 4.5. Characterization of Cu: In_2O_3 nanocrystals. **a**) Pictures of the purified nanocrystals dispersed in hexanes. From left to right, the nanocrystals the same day of

synthesis, two days after synthesis, and two weeks after synthesis. The final vial shows a concentrated solution of the nanocrystals two weeks after synthesis. The optical absorbance spectra of these solutions are shown in **b**). Panel **c**) XRD spectra of the doped nanocrystals two days (blue) and two weeks (green) after synthesis. The spectra of bulk In_2O_3 and undoped In_2O_3 are shown for reference. **d**) XPS spectra of the Cu 2p region immediately (red) and two days (blue) after synthesis. The spectra indicate copper is diffusing towards the nanocrystal surface.

Conclusion

Precise control of doped nanocrystal composition and structure is critical to the development and understanding of their important optical, magnetic, catalytic, and optoelectronic properties. Herein we synthesized substitutionally-doped Mn: In_2O_3, Fe: In_2O_3, Co: In_2O_3, Cu: In_2O_3, and Zn: In_2O_3 nanocrystals with dopant concentrations as high as 20%. Nanocrystal dopant concentration was controlled simply by the precursor feed ratio, allowing the logical preparation of compositions without the need for tedious trial and error. Dopant incorporation efficacy exceeded 90% for all dopants except for copper, which ranged from 67-92%, depending upon the feed ratio. Empirically selecting metal precursors was not necessary, and metal oleates of both host and dopant cations were used as metal precursors. This is made possible because the synthetic approach relies on the metal-catalyzed esterification of metal carboxylates, not thermal decomposition, and growth proceeds in a highly controlled, slow manner. The slow-growth approach allows concentration of both host and dopant cation to be constant over time, ensuring that dopant cations are homogeneously distributed throughout the nanocrystal. That copper could be incorporated into the In_2O_3 lattice, despite its propensity to segregate to the nanocrystal surface, demonstrates the level of kinetic control of dopant incorporation offered by the living growth synthesis. Wide band-gap oxides, like In_2O_3, allow ligand-field transitions from dopant cations to be easily observed. We utilized these optical features, elemental

composition analysis by ICP-OES and XPS, and XRD analysis, to confirm that dopants were substitutionally doping for In^{3+} cations.

The slow-addition approach allows the layer-by-layer growth of nanocrystals, resulting in precise control of composition as crystal growth continues and enhanced size control of doped and undoped structures.[55] This opens up the possibility for the logical synthesis of graded nanostructures and the radial localization of dopants to specific locations within the nanocrystal. Additionally, co-doping or adding multiple dopants into the same nanocrystal, within the same or different radial location, open up a new range of property exploration and optimization. The synthetic approach should be amenable to other transition metal dopants (and matrix oxides), beyond those we report here, at large dopant concentrations and with high, near 100% efficacy. The ability to prepare highly-doped nanoscale structures without rigorous optimization will not only decrease the time and resources for the production of materials but also aid in understanding and utilizing properties found from new structures.

Methods and Materials

Materials

Indium(III) acetate (99.99%), manganese(II) acetate (98%), copper(II) acetate (98%), iron(III) acetylacetonate, zinc(II) acetate, oleic acid (90% technical grade), were purchased from Sigma Aldrich and used as received. Oleyl alcohol (80−85% technical grade) was purchased from Alfa Aesar and used as received. A flow meter Cole-Parmer (model 03216−10) was used to monitor nitrogen flow.

Characterization of Transition Metal Doped Indium Oxide Nanocrystals

Small angle X-ray scattering (SAXS) analysis was done on a lab-scale SAXS (SAXSess, Anton Paar, Austria). The system was attached to an X-ray generator equipped with a X-ray tube (Cu Kα X-rays with wavelength $\lambda = 0.154$ nm) operating at 40 kV and 50 mA. The raw data was processed with SAXSquant software (version 2.0), and scattering curves were averaged over 50 individual acquisitions for various acquisition times (.5-10s). Curve fitting was done using Irena macros for IGOR (V. 6.3).[94]

Transmission electron microscopy (TEM) images and electron diffraction patterns were collected on 400 mesh Cu grids (Ted Pella, Redding, CA) using a Tecnai Spirit TEM (FEI, Hillsboro, OR) operating at 120 kV. Samples were prepared by dipping the grid into a dilute solution of particles. Images were analyzed using ImageJ software.[95]

Elemental compositions of the nanocrystal cores were determined using a Teledyne Leeman Labs (Hudson, NH) Prodigy High Dispersion Inductively Coupled Plasma Optical Emission Spectrometer (ICP-OES). Nanocrystals were dried and digested in stock nitric acid for at least 48 hrs before being diluted for analysis. Surface composition by X-ray photoelectron spectroscopy (XPS) was acquired using a Thermo Scientific ESCALAB 250 X-ray photoelectron spectrometer. Samples were prepared by drop-casting a hexane solution of nanocrystals on mica substrates.

X-ray diffraction (XRD) was carried out on a Rigaku Smartlab instrument using Bragg Brentano geometry and Cu Kα radiation. A step size of 0.01^{o} and collection speed of 0.1 degrees/min was utilized over a range of 20-70 2θ. Rietveld refinement was conducted on the collected patterns using Fullprof Suite.[71]

Optical absorbance data was collected with a Perkin Elmer (Waltham, MA) Lambda 1050 UV/Vis/NIR Spectrometer. Samples were dispersed in hexanes and data were collected at room temperature.

Fourier-transform infrared (FTIR) spectra on the nanocrystals were obtained using a Thermo Fisher Nicolet 6700 spectrometer. Samples were deposited form a hexanes solution and pressed into a KBr pellet.

Synthesis of Transition Metal Doped Indium Oxide Nanocrystals

Samples were prepared as described previously.[56] One mmol metal carboxylate solutions were prepared by mixing indium(III) acetate and the appropriate metal dopant salt with 2 mL of oleic acid in a 20 mL glass scintillation vial. The vial was then heated to 150°C in an oil bath under N_2 for at least one hour to generate a metal-oleate precursor solution. For the Fe doped precursor, the solution was allowed to sit at 190°C for at least an hour. The as-prepared precursor solution was added dropwise (0.35 mL/min) to a three-neck 100 mL flask containing 13 mL of oleyl alcohol heated to 290°C. The precursor solution was added using a syringe pump fitted with a 20 mL syringe. During addition, N_2 was flowing through the flask at a rate of 120-130 cc/min. All three necks of the flask were capped with septa, and three 16-gauge purge needles were placed in one of the necks with a small amount of Kimwipe in the purge needles to prevent water reintroduction into the flask.

After synthesis, the nanocrystal solution was allowed to sit at reaction temperature for 5 minutes under N_2 flow, after which the solution cooled to room temperature. To isolate the nanocrystals, 30 mL of ethanol was added to precipitate the nanocrystals. The nanocrystals were isolated by centrifugation at 7300 rpm for 10 minutes. The product was

washed twice more with ethanol and collected by centrifugation. The washed nanocrystals were then dispersed in hexanes. The solution of nanocrystals was then centrifuged at 7000 rpm for one minute to remove any insoluble material. After purification, typical yield of doped nanocrystal was > 100 mg (~90% yield).

Bridge to Chapter V

The similar reactivities of the host and dopant precursors under esterification conditions, shown in chapter IV, leads to dopant concentrations easily controlled through the ratio of precursors used. The slow, layer by layer growth method not only allows for homogeneously distributed dopants, but also the ability to synthesize doped/undoped and undoped/doped core/shell nanocrystals where the radial position of the dopant can be altered. The dramatic improvement in synthetic control over dopant placement makes it possible to systematically investigate the influence of dopant concentration and radial distribution on the LSPR, revealing a strong dependence of LSPR energies, dopant activations and LSPR quality factors upon dopant location, which are discussed in chapter V. The study demonstrates the first example of LSPR tailoring through precise radial dopant placement, and investigates the resulting optical properties from these architectures.

CHAPTER V

RADIAL DOPANT PLACEMENT FOR TUNING PLASMONIC PROPERTIES IN METAL OXIDE NANOCRYSTALS

This chapter was previously published as Crockett, B. M.; Jansons, A. W.; Koskela, K. M.; Johnson, D. W.; Hutchison, J. E. Radial Dopant Placement for Tuning Plasmonic Properties in Metal Oxide Nanocrystals. *ACS Nano* **2017**, *11* (8), 7719–7728.

Introduction

The unique properties of plasmonic nanomaterials allow their use in a variety of applications, such as spectroscopy,[1,2] chemical sensing,[3–5] transparent conducting films,[6,7] and as biomedical agents.[8–10] Recently, non-noble metal nanomaterials that display localized surface plasmon resonances (LSPRs) in the infrared (IR) and near-IR (NIR) region of the electromagnetic spectrum have been investigated, and their use explored as active components in a variety of the above applications.[11–15] Several types of extrinsically-doped oxide nanocrystals that display tunable LSPRs have been reported, including Sn-doped In_2O_3 (ITO),[16–20] Ce-doped In_2O_3,[21] In or Al-doped ZnO,[22–24] In and F/In co-doped CdO,[6,25,26] and Nb-doped TiO_2.[27] In these cases, the LSPR arises when dopant atoms and crystalline defects contribute free electrons into the conduction band that collectively oscillate when excited by their resonance frequency. In the case of metal oxides, the energy

of the LSPR can be tailored through changes in aliovalent dopant concentration or dopant identity.[14–16,26,28,29]

Recent reports suggest that the radial distribution of dopants in metal oxide nanocrystals may contribute to large variations in the plasmonic properties of these materials, specifically damping (which correlates to the LSPR linewidth)[14,30] and dopant activation (the number of free electrons per dopant cation).[31] Three example dopant architectures are shown in Figure 5.1. Using ITO nanocrystals as a model system, Lounis *et al*. observed that the LSPR energy and shape depend upon the radial dopant distribution of Sn.[31] The authors suggest that mitigating dopant heterogeneity and size effects, as well as deliberate radial placement of dopant atoms would be a powerful strategy for designing plasmonic nanocrystal properties. Such an approach however, is difficult to impossible to achieve given the current state of colloidal nanocrystal syntheses. In order to gain access to such level of LSPR control, a synthetic approach is required that allows for sub-nanometer size and composition control during the growth phase, which would permit the logical production of advanced structures, including doped/undoped or undoped/doped core/shell architectures.

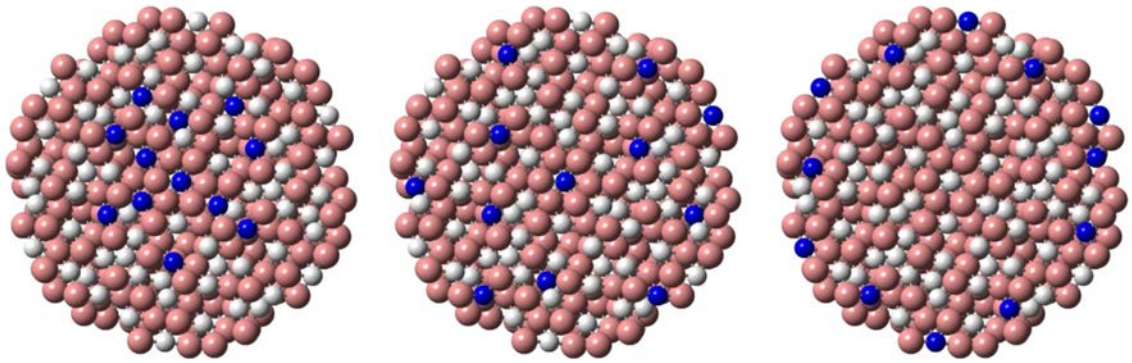

Figure 5.1. Schematic cross-section representations for three dopant distributions of Sn in an In_2O_3 nanocrystal. Sn localized in the core (left), Sn homogeneously doped

(middle), and Sn localized towards the surface (right). Oxygen, indium, and tin atoms are red, white, and blue spheres respectively. Schematics were generated in CrystalMaker using a bixbyite In_2O_3 lattice.

Recently, we reported a synthesis for both binary and doped metal oxide nanocrystals based upon esterification of metal oleates in long-chain alcohol solution that has the potential for deliberate and precise radial control over dopant placement.[32–34] During *slow* addition of a metal carboxylate into long-chain alcohol at elevated temperatures (> 200 °C), metal oxide particles nucleate and then grow continuously without coalescence, ripening, or forming additional particles. The synthesis proceeds with > 90 % yield and can provide gram-scale material.[33] This approach proceeds through a living or continuous growth mechanism, where the nucleated particles continue to grow upon the addition of more precursor. New metal oxide compositions can be added as a shell on the core matrix in a predictable fashion. Thus, this approach should permit the precise placement of dopants within a particle due to the layer-by-layer growth process.

Herein we utilize this approach to synthesize Sn-doped In_2O_3 nanocrystals with deliberate radial dopant placement and investigate the resulting LSPR spectra. We demonstrate that it is possible to precisely control the radial placement of dopants, maintaining uniform size dispersions and controlled core dimensions. We observe decreases in LSPR damping with dopant-segregated regions in the core or the shell with respect to homogeneously-doped nanocrystals. We confirm the presence of inactive Sn dopants on the nanocrystal surface, and observe their activation upon the addition of a sub-nanometer thick undoped In_2O_3 shell. Finally we show it is possible predictively design LSPR shape and energy, independent of dopant concentration, through control over core or shell dopant placement.

Results and Discussion

Synthesis of Core/shell Nanocrystals with Varying Radial Dopant Placement

Two series of core/shell nanocrystals (In_2O_3/ITO core/shell, ITO/In_2O_3 core/shell) were synthesized through a one-pot, controlled, slow addition approach. Each series was synthesized (Scheme 5.1) by a two-stage approach whereby either i) an indium oleate precursor is used to produce an In_2O_3 core, then subsequently, and without purification, the mixed In/Sn precursor is slowly added to produce In_2O_3/ITO core/shell nanocrystals, or ii) a mixture of Sn and In oleate precursors is used to produce an ITO core, then subsequently, an indium oleate precursor is slowly added to produce ITO/In_2O_3 core/shell nanocrystals. Shell thicknesses were varied in each series to investigate the influence of dopant placement on the LSPR. Aliquots were taken and purified for analysis after the formation of the core and periodically during shell growth.

Scheme 5.1. Living growth synthesis of homogeneously doped and core/shell nanocrystals. In_2O_3 and ITO are represented in red and blue, respectively.

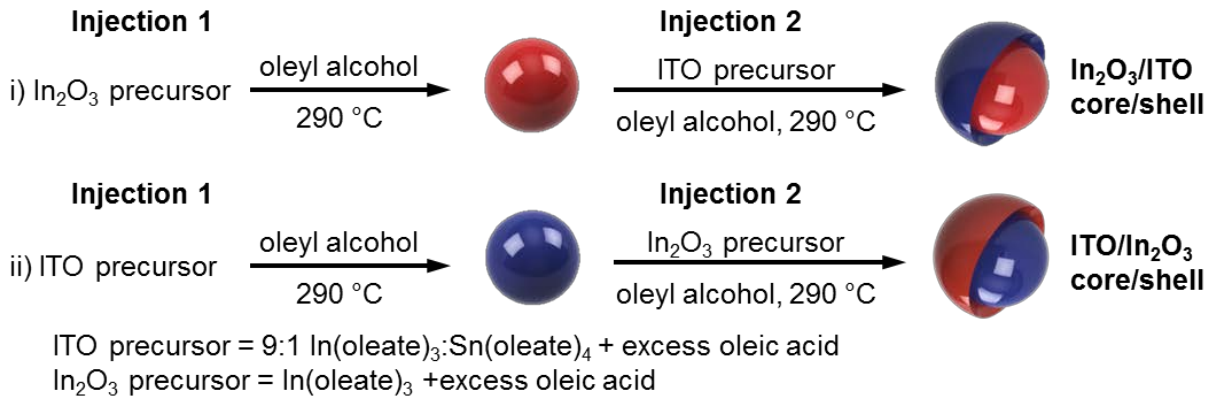

The dopant locations in the nanocrystals were investigated through a combination of bulk and surface elemental analysis. Absolute dopant concentration was determined for nanocrystals digested in stock hydrochloric acid and analyzed using inductively coupled plasma optical emission spectroscopy (ICP-OES). The concentrations of surface localized Sn were investigated using X-ray photoelectron spectroscopy (XPS). XPS probes only the surface atomic structure (the sampling depth was calculated to be ~ 5 nm for the In and Sn 3d photoelectrons)[35] and has been previously shown to be a powerful technique in elucidating nanocrystal dopant distributions.[22,31] Relative surface Sn concentrations were quantified by integrating the In and Sn $3d_{5/2}$ peaks in the XPS spectra. Only minor attenuation of the signal is expected from the ligand shell, and this should be similar for both the indium and tin signals. Elemental analysis results are shown in Figures C1 and C2, and were used to confirm that Sn dopants were either located in the core or shell of the nanocrystals for the ITO/In_2O_3 and In_2O_3/ITO core/shell series respectively.

Figure 5.2 displays TEM micrographs of the initial core and final core/shell samples for the In_2O_3/ITO core/shell and ITO/In_2O_3 series. The nanocrystals are uniformly-sized single crystals that pack readily into extended arrays. HRTEM was performed on the largest In_2O_3/ITO and ITO/In_2O_3 core/shell particles (Figure C3). The analysis does not reveal the presence of any apparent structural defects of the crystalline particles at the core/shell interfaces, suggesting that the shells are epitaxially grown onto the core of the nanocrystals. Shell growth was monitored *via* SAXS (Figures C1 and C2). The final (largest) shell thicknesses were 4.1 and 4.0 nm for the In_2O_3/ITO and ITO/In_2O_3 series, respectively. SAXS and TEM analysis confirmed that there was no new nucleation upon shell precursor

injection. The NIR absorbance spectra were measured from 3,100 to 11,000 cm^{-1} (3225 to 909nm), and plotted for the In_2O_3/ITO and ITO/In_2O_3 core/shell series in Figures 5.2e and 5.2f, respectively. The initial absorbance spectrum of the In_2O_3/ITO core/shell series in Figure 5.2e (black spectrum) displays no LSPR absorbance in the NIR and only displays ligand C-H stretches, as expected for an undoped nanocrystal.

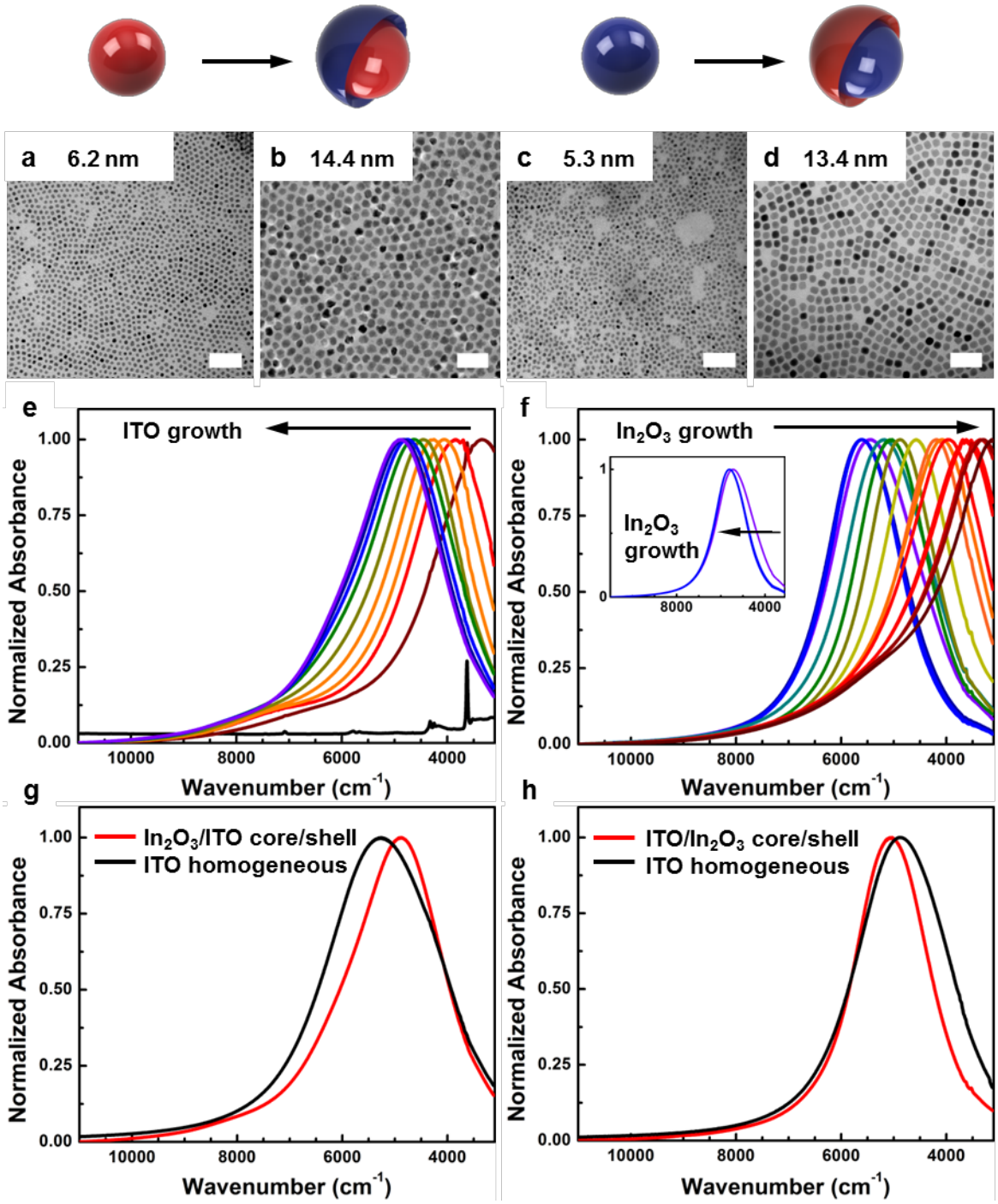

Figure 5.2. Core/shell schematics, TEM micrographs, and NIR spectra of In_2O_3/ITO (left) and ITO/In_2O_3 (right) core/shell nanocrystals. TEM images and respective core/shell schematics of the initial core and final core/shell samples, with sizes reported from SAXS: In_2O_3 core (**a)**; In_2O_3/ITO core/shell **(b)**; ITO core **(c)**; ITO/In_2O_3 core/shell **(d**). Core/shell schematics represent In_2O_3 and ITO in red and blue respectively. Scale bars are 50 nm. Normalized LSPR spectra for In_2O_3/ITO series during ITO shell growth

(**e**), and ITO/In_2O_3 series during In_2O_3 shell growth (**f**). Normalized LSPR spectra of the ITO core and first ITO/In_2O_3 core/shell nanocrystal to show the initial blue-shift in the LSPR as a result of shell growth (**f, inset**). NIR spectra of In_2O_3/ITO core/shell sample (red) and homogeneously-doped ITO (black), with Sn concentrations of 9.71 and 9.98 atomic %, respectively (**g**), NIR spectra of ITO/In_2O_3 core/shell sample (red) and homogeneously-doped ITO (black), with Sn concentrations of 7.36 and 7.17% respectively (**h**).

The LSPR spectra for the In_2O_3/ITO core/shell nanocrystals are shown in Figure 5.2e. The shift in the $LSPR_{max}$ to higher energies with more incorporated Sn is consistent with that predicted by Eq. 1. The response of the LSPR should be proportional to the bulk plasma frequency (ω_p), described by

$$\omega_p = \sqrt{\frac{N_e e^2}{m^* \varepsilon_0}} \tag{1}$$

where N_e is the free carrier concentration, e is the elementary charge, m^* is the effective mass, and ε_0 is the permittivity of free space. As more Sn is incorporated into the lattice, the free carrier concentration is expected to increase, until a saturation point is reached at very high concentrations[16] (> 15 % Sn). For the ITO/In_2O_3 core/shell nanocrystals (Figure 5.2f), the $LSPR_{max}$ decreases as the dimensions of the In_2O_3 shell are increased, consistent with a dilution of free electrons due to the addition of the undoped shell.

Upon closer inspection of the spectra for the ITO/In_2O_3 core/shell nanocrystals (Figure 5.2f, inset), there is a blue-shift from 5436 to 5629 cm^{-1} upon initial In_2O_3 shell growth before the peak maxima shift to longer wavelength as the shell thickens. The blue shift is accompanied by a 25% decrease in linewidth (1992 cm^{-1} to 1548 cm^{-1}). To further explore the influence of thin shells of indium oxide on the ITO cores, we grew a series of sub-nanometer In_2O_3 shells on ITO (Figure C4). Although one would expect that the addition

of an undoped, In_2O_3 shell would effectively dilute the Sn concentration in the nanocrystal, and therefore should shift the LSPR to lower energy according to equation (1), these experiments (Figure C4) confirmed our initial observation that thin In_2O_3 shells lead to an initial blue-shift of the LSPR suggesting an effective increase in free electron concentration in the material. This observation provides further evidence to hypotheses that the ITO surface contains localized Sn surface trap states that contribute to a reduced dopant activation in ITO,[13,31] which can be activated by a sub-monolayer In_2O_3 shell. Surface trap states are well known in the QD literature[36–39] and can arise from a combination of ligand-surface interactions, dangling bonds, and surface site defects.

To further explore the influence of dopant placement on the LSPR, samples with the same dopant concentration, but different radial placement of the dopant atoms, were synthesized and examined. Figure 5.2g compares the LSPR response of an In_2O_3/ITO core/shell sample with a homogeneously-doped ITO nanocrystal sample, containing 9.71 and 9.98 atomic % Sn, respectively. Structural characterization, including ICP-OES and XPS analysis for both samples are shown in supporting information (Table C1). The $LSPR_{max}$ for the In_2O_3/ITO core/shell sample is red-shifted by approximately 381 cm^{-1} and linewidth is decreased by approximately 439 cm^{-1} (17%), relative to the homogeneously-doped sample. The red-shift is likely due to the slightly lower Sn concentration in the core/shell sample. A similar decrease in linewidth has been previously observed for surface-segregated ITO nanocrystals.[31] In that case, the authors suggest that narrowing of the linewidth results from less dopant-based scattering in the Sn-depleted core.

A comparison of the LSPR spectra for an ITO/In_2O_3 core/shell sample and a homogeneously-doped ITO sample of the approximately the same Sn concentration (7.36

and 7.17 atomic %, respectively) is shown in Figure 5.2h. Structural and compositional characterization for both samples is shown in Table C2. Just as in the previous case, the LSPR linewidth in the core/shell sample is narrower (by 26%, 1629 *versus* 2201 cm^{-1}) compared to the homogeneously-doped sample. In this case; however, the $LSPR_{max}$ of the core/shell sample is blue-shifted relative the homogeneously-doped sample by 145 cm^{-1}. The observed effects likely arise from the dopant-free shell, which aids in reducing damping and a slight increase in dopant concentration (*vide infra*).

Extraction of Optical Constants for Core/Shell Nanocrystals

The NIR optical responses observed in ITO nanocrystals can be interpreted semi-quantitatively through their dielectric function described by the free electron approximation of the Drude equation

$$\varepsilon_{NC}(\omega) = \varepsilon_{\infty} - \frac{\omega_p^2}{(\omega^2 + i\omega\Gamma)} \tag{2}$$

where ε_∞ is the high frequency dielectric constant of ITO (taken as 4), ω_p is the bulk plasma frequency of the free carriers, and Γ is the free carrier damping. Using the Drude equation, the LSPR absorption cross-section (σ_A) of the nanocrystals can be modeled from the quasi-static approximation of Mie theory

$$\sigma_A = 4\pi k R^3 Imag\left\{\frac{\varepsilon_{NC}(\omega) - \varepsilon_m}{\varepsilon_{NC}(\omega) + 2\varepsilon_m}\right\} \tag{3}$$

where ε_m is the dielectric constant of the medium (2.238 for CCl_4), $k = \sqrt{\varepsilon_m}\omega/c$, and R is the nanocrystal radius. The absorbance of the NC solution can then be calculated with the Beer-Lambert law

$$A = \frac{N\sigma_A L}{\log(10)} \tag{4}$$

where N is the nanocrystal number density (#particles/cm^{-3}), and L is the pathlength of the cuvette. LSPR spectra from Figure 5.2 were modeled in order to extract ω_p and Γ. This simple Drude model has been used extensively to model LSPR spectra of semiconducting and oxide nanocrystals.[14,15,40–42] Example modeled spectra, along with a comparison to the observed spectra, are shown in Figure C5. Figure 5.3a shows ω_p and Γ as a function of shell thickness for both the In_2O_3/ITO and the ITO/In_2O_3 core/shell nanocrystals represented in Figures 5.2e and 5.2f.

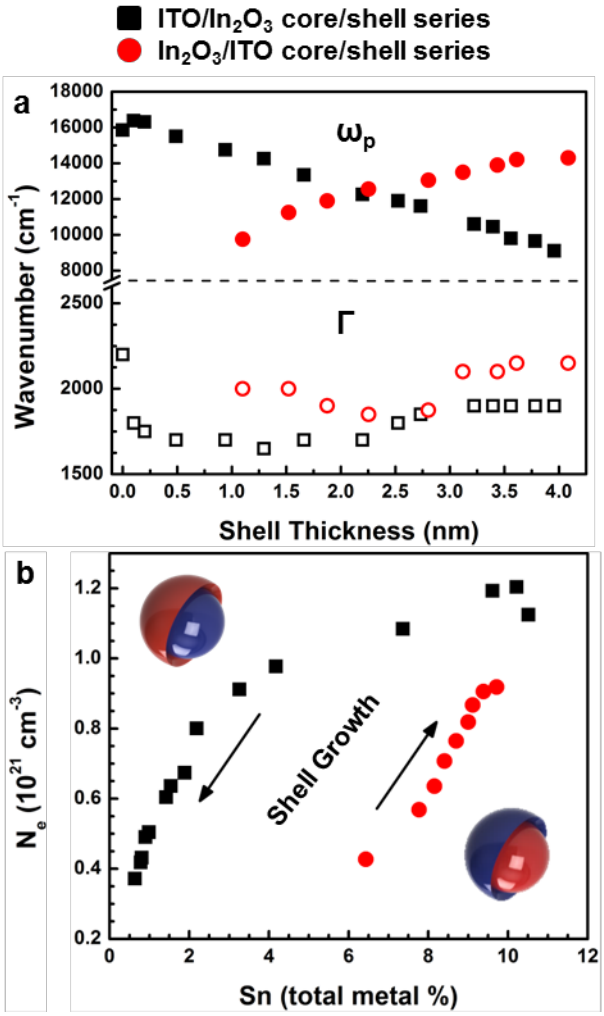

Figure 5.3. Extracted parameters from the spectra in Figure 5.2 as a function of shell thickness and absolute Sn concentration (measured by ICP-OES). Black and red symbols represent ITO/In_2O_3 and In_2O_3/ITO core/shell nanocrystals respectively. ω_p (top, solid symbols) and Γ values (bottom, open symbols) plotted *versus* shell thickness (**a**). N_e values plotted against absolute Sn concentration (**b**). The core/shell schematics are placed for reference, with In_2O_3 and ITO represented in red and blue respectively.

As expected by equation 1, ω_p increases with increasing shell thickness for the In_2O_3/ITO core/shell nanocrystals. Interestingly Γ decreases initially, indicating a reduction in electron scattering during LSPR excitation. As the main scattering mechanism in ITO is

electron-ionized impurity scattering,[43,44] this decrease in Γ is most likely due to the undoped In_2O_3 core providing an impurity-free zone for conduction band electrons to oscillate upon excitation. At greater shell thicknesses, the In_2O_3/ITO core/shell nanocrystals display in increase in Γ, most likely from the nanocrystals being > 90% ITO by volume and exhibiting damping closer to homogeneous ITO (see Γ for ITO core, shell thickness = 0 nm, in Figure 5.3a).

For the ITO/In_2O_3 core/shell nanocrystals, ω_p increases during the first nanometer of shell growth, indicating and increase in N_e (Figure C4). A significant decrease in damping, Γ, is also observed upon initial shell growth. Near the maximum shell thicknesses, Γ increases, likely due to the cubic-shape of the nanocrystals (Figure 5.2d) giving rise to additional shape-dependent plasmonic modes in the LSPR spectrum.[21,45] The decrease in damping exhibited by both core/shell nanocrystals provides strong evidence that the undoped In_2O_3 region is the main factor in decreasing impurity scattering, independent of dopant concentration (as shown by Figures 5.2g and 5.2h). However the undoped In_2O_3 region located in the shell seems to reduce damping the most, likely due to reduced surface scattering, lack of Sn surface trap states, in addition to the impurity-free zone that both core/shell nanocrystals possess.

For both core/shell nancorystals, N_e values were calculated from the extracted ω_p values using equation 1, and plotted in Figure 5.3b *versus* absolute Sn% as measured by ICP-OES. The ITO/In_2O_3 core/shell nanocrystals display an increasing N_e initially in agreement with the observed blue-shift from Figure 5.2f, and a gradual decrease in N_e as the Sn is diluted from the In_2O_3 shell. Conversely, the In_2O_3/ITO core/shell nanocrystals display an increase in N_e with increasing shell thickness. Comparing the two series, the ITO/In_2O_3 core/shell

series utilizes nearly an order of magnitude less absolute dopant % for an equivalent LSPR energy than the In_2O_3/ITO core/shell series (0.78% Sn for N_e of 0.42 x $10^{21}cm^{-3}$ *versus* 6.43% Sn for N_e of 0.43 x $10^{21}cm^{-3}$ respectively). Because the nanocrystal diameters are several orders of magnitude smaller than the wavelength of absorbing light, size effects on the LSPR are negligible and can effectively be ignored,[40,46] indicating that only dopant concentration and radial location (core *versus* shell) is contributing to the LSPR spectra. As aliovalent doping leads to scattering-based damping in metal oxides, any opportunity to reduce dopant concentration is an opportunity to improve material performance.

Investigating the Impact of Radial Dopant Placement on LSPR Energy and Damping

Currently two of the biggest challenges in plasmonic metal-oxide nanocrystal synthesis are increasing dopant activation (*i.e.*, maximizing the number of free electrons contributed per dopant atom) and mitigating plasmonic damping. Common causes of reduced dopant activation include dopant-induced defects (such as Sn-oxo complexes and the formation of tin oxide phases)[47,48] and inactive surface sites[31,49,50] (arising from crystal defects[36,38] and ligand-metal binding[39]). Thus, in attempts to achieve high dopant activation at large dopant concentrations, these increases in dopant levels may yield more defects and reduce activation. Plasmonic damping generally arises from a combination of ionized impurity scattering (from the dopant atoms themselves), surface scattering, and scattering from charge compensation defects (such as oxygen vacancies).[14,15] Ionized impurity and charge compensation defect scattering are generally reduced by a decrease in Sn concentration. It is therefore synthetically challenging to mitigate damping when higher dopant densities are needed to achieve desired carrier concentrations.

To explore how the radial placement of dopants can be used as a strategy to enhance dopant activation and reduce plasmon damping, we synthesized and investigated the optical properties of two core/shell series of Sn-doped In_2O_3 nanocrystals. The *Doping Series* allows for the investigation of architecture on LSPR energies and dopant activations by keeping the absolute doping levels constant. This is accomplished by adapting the synthetic strategy in Scheme 5.1 so that nanocrystal samples in the Doping Series would be of approximately equal doping concentration and diameter. This ensures that the observed changes to the LSPR and observed dopant activation would be due solely to the radial dopant location. Because the plasmon energy depends on damping (Eqs. 2-4), a series of nanocrystals were produced with the same $LSPR_{max}$ to isolate the effects of radial dopant placement on damping. Thus, the *Damping Series* allows for a convenient comparison of structural effects on damping by holding LSPR energy equivalent across different nanocrystal structures. To this end, two core/shell samples, one from Figure 5.2e and one from Figure 5.2f in Section I, were selected that have the same LSPR energies. A homogeneously-doped sample was designed and synthesized to have the same LSPR energy for comparison to the other two samples.

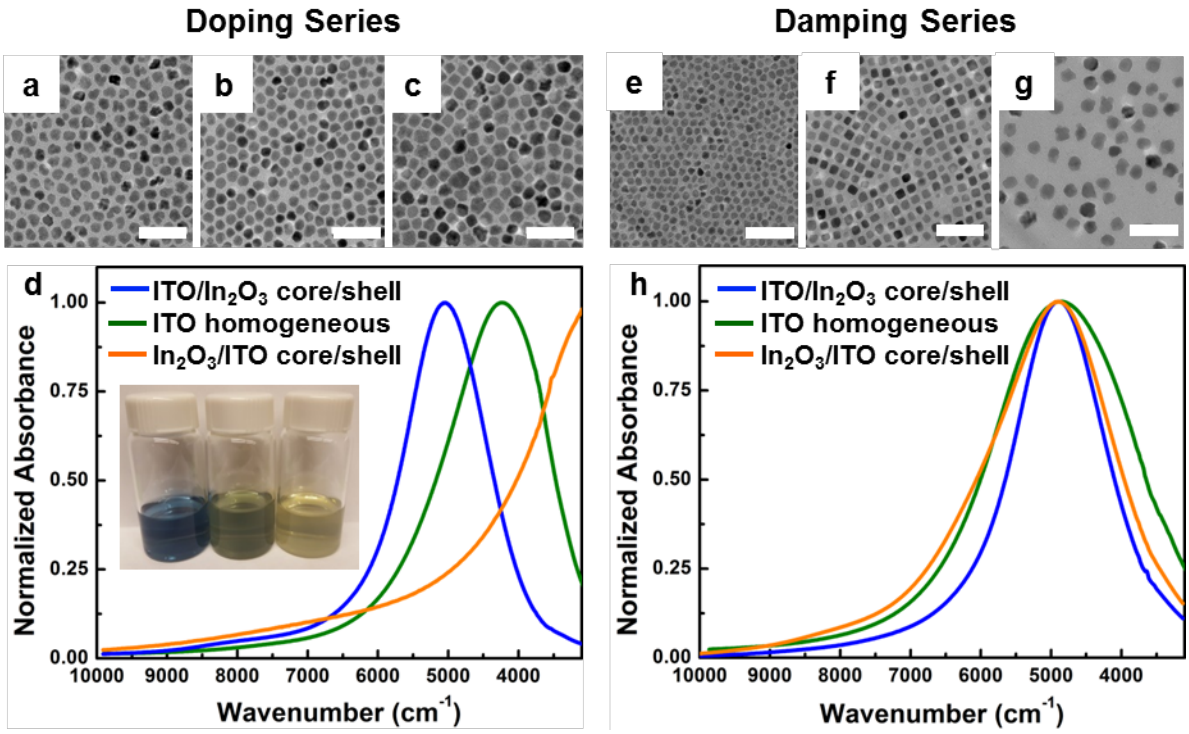

Figure 5.4. ITO nanocrystals for the Doping (left) and Damping (right) Series. Doping Series (left): TEM micrographs of homogeneously doped ITO nanocrystals (**a**), ITO/In_2O_3 core/shell nanocrystals (**b**), and In_2O_3/ITO core/shell nanocrystals (**c**). Scale bars are 50 nm. Normalized LSPR absorption spectra (**d**). Inset: photograph of the purified nanocrystal solutions in hexanes, immediately following synthesis, spectra presented left to right correspond to solution presented left to right. Damping Series (right): TEM micrographs of homogeneously doped ITO nanocrystals (**e**), ITO/In_2O_3 core/shell nanocrystals (**f**), and In_2O_3/ITO core/shell nanocrystals (**g**). Scale bars are 50 nm. Normalized LSPR absorption spectra (**h**).

Figure 5.4 displays TEM micrographs for the nanocrystals from both Doping and Damping Series. Samples in the Doping Series are approximately equal size as measured by SAXS (Table 5.1), with the In_2O_3/ITO sample measured to be slightly larger (~ 2 nm larger in diameter), likely due to differences in nucleation without the initial presence of dopant cations. Samples in the Damping Series have different sizes, as well as shape, by SAXS (Table 5.2) and TEM. These size and shape discrepancies are expected given the varying Sn concentrations and core/shell architectures required to produce an LSPR with

the same energy. The dopant distributions were investigated *via* ICP-OES and XPS in the same fashion described previously. The overall tin content of samples in the Doping Series (Table 5.1) is essentially the same (within 0.5 atomic % Sn) as measured by ICP-OES. Results of the surface analysis by XPS (Table 5.1) are in agreement with the specific architecture described, and confirm the anticipated Sn localization in each sample. The Damping Series contains a range Sn doping percentages from 3.26 to 9.71 total metal %.

Table 5.1. Doping Series: nanocrystal size, absolute and surface Sn concentrations, and extracted parameters from Drude modeling of the LSPR spectra in Figure 5.4d.

Structure	Size +/- 1σ (SAXS, nm)	Core size (SAXS, nm)	Sn % (ICP-OES)	Sn % (XPS)	ω_p (cm^{-1})	N_e ($10^{21}cm^{-3}$)	Γ (cm^{-1})
ITO homogeneous	10.7+/- 1.6	N/A	4.17 +/- 0.05	4.5 +/- 0.2	12750	0.73	1850
ITO/In_2O_3 core/shell	10.2+/- 1.2	7.0 +/- 1.0	3.63 +/- 0.08	2.5 +/- 0.2	15280	1.05	1650
In_2O_3/ITO core/shell	12.8 +/- 1.6	11.1 +/- 1.4	3.84 +/- 0.06	5.6 +/-0.1	7500	0.25	3100

Table 5.2. Damping Series: nanocrystal size, absolute and surface Sn concentrations, and extracted parameters from Drude modeling of the LSPR spectra in Figure 5.4h.

Structure	Size +/- 1σ (SAXS, nm)	Core size (SAXS, nm)	Sn % (ICP-OES)	Sn % (XPS)	ω_p (cm^{-1})	N_e ($10^{21}cm^{-3}$)	Γ (cm^{-1})
ITO homogeneous	7.3+/- 1.1	N/A	7.17 +/- 0.05	7.7 +/- 0.2	14250	0.91	2500
ITO/In_2O_3 core/shell	7.9+/- 0.9	5.3 +/- 2.3	3.26 +/- 0.07	3.5 +/- 0.2	14300	0.92	1600
In_2O_3/ITO core/shell	14.4 +/- 2.2	6.3 +/- 0.8	9.71 +/- 0.04	10.3 +/-0.2	14300	0.92	2050

The NIR absorbance spectra were measured and plotted for the Doping Series in Figure 5.4d. The colors of the as-synthesized nanocrystal solutions dispersed in hexanes (Figure 5.4d inset) are strikingly different, ranging from yellow to blue, despite the nanocrystal containing the same concentration of dopant. Upon inspection of the NIR spectra (Figure 5.4d) we observe the ITO/In_2O_3 core/shell nanocrystals to have the highest LSPR energy (of 5020 cm^{-1}), compared to 4220 cm^{-1} and 3030 cm^{-1} for the homogeneously-doped and In_2O_3/ITO nanocrystals, respectively. To further investigate the LSPR, we modeled all three spectra with the Drude formula., with the extracted values in Table 5.1.

The ITO/In_2O_3 core/shell sample exhibits an N_e value four times greater than the In_2O_3/ITO core/shell sample, with damping reduced by 50%. The extracted damping from the In_2O_3/ITO sample is much larger, either because of the cubic nature of the nanocrystal and/or detector cutoffs that do not allow the full LSPR to be observed and modeled. The ITO/In_2O_3 core/shell sample also yields an N_e value 25% larger, and damping value that is 11% reduced with respect to the homogeneous sample. The N_e value ($1.05\ 10^{21} cm^{-3}$) for the ITO/In_2O_3 core/shell nanocrystals is unusually high given the doping level (3.26% Sn). In previously reported ITO nanocrystal samples, significantly higher doping levels (5 – 7% Sn) were required in order to attain an analogous free carrier concentration, depending upon the reaction chemistry used to synthesize the nanocrystals.[31] Combined, these results indicate that having a dopant-free shell (*i.e.*, ITO/In_2O_3 core/shell) increases dopant activation more than the other two architectures.

The NIR absorbance spectra were measured and plotted for the Damping Series in Figure 5.4h. LSPR linewidth (which is an indication of the overall damping in the nanocrystal) has been shown to be a defining feature for device performance and design,[4,30,51–53] from

sensing, thin film conductivity,[31] and selective electromagnetic radiation filtering.[54–56] From the spectra in Figure 5.4h, it is readily apparent that linewidth can be tuned with radial dopant placement, with linewidths measured to be 1552, 2101, and 2358 cm^{-1} for the ITO/In_2O_3 core/shell, In_2O_3/ITO core/shell, and ITO homogeneous nanocrystals respectively. As measured by ICP-OES, the Sn % required to produce an LSPR of ~4870 cm^{-1} for the ITO/In_2O_3 core/shell sample is only 3.55 %, compared to 7.20 % and 9.71 % for the homogeneously doped ITO and In_2O_3/ITO core/shell nanocrystals respectively. This activation trend is in agreement with our findings from the Doping Series, with Sn being most activated when there is an In_2O_3 shell (ITO/In_2O_3 core/shell).

To compare damping and carrier concentration values between the samples, Drude modeling was performed on the LSPR spectra from Figure 5.4h for the Damping Series, and the extracted values shown in Table 5.2. Both core/shell nanocrystals display dramatically reduced damping values with respect to the homogeneous sample, with a 36% and 18% damping reduction for the ITO/In_2O_3 and In_2O_3/ITO nanocrystals, respectively. The In_2O_3/ITO core/shell sample is particularly interesting, because the nanocrystals contain much more overall Sn relative to the homogeneously-doped sample (Table 5.2), however In_2O_3/ITO core/shell nanocrystals display *less* plasmonic damping. This suggests that the dopant-depleted core is aiding in reducing the damping regardless of the excess Sn present. Across the three samples the ITO/In_2O_3 core/shell sample produces the lowest damping value of 1600 cm^{-1} due to (i) reduced impurity scattering from fewer dopant cations present (Table 5.2) and (ii) the dopant-depleted shell. Plasmon damping values have been reported with wide ranges[31] as high as 5000-8000 cm^{-1}, from nanocrystals synthesized with a combination of carboxylates and amines,[16] and with much lower values

of 900 – 1500 cm^{-1} from nanocrystals synthesized from a mixture of metal acetonates, chlorides and oleyl amine.[18] While it may be tempting to draw direct comparisons from values in this study to other values reported for ITO nanocrystals in the literature, the chemistries used to synthesize the nanocrystals can influence the properties beyond the effects due to doping. The range of ITO syntheses rely on different solvents, surfactants, metal precursors, temperatures, and counter anions, all of which will contribute to the defect chemistry in the nanocrystals that is then manifested spectrally in sometimes unpredictable ways. The approach presented here allows for direct comparison between nanocrystals synthesized with varying levels and placements of dopants because the nanocrystals are all synthesized from the same precursor material, using the same surfactants, under the same reaction conditions.

Conclusion

The synthetic method described here offers the opportunity for precise radial dopant positioning within an oxide nanocrystal matrix. Dopants can be positioned with sub-nanometer precision into the host nanocrystal *via* the slow injection of metal precursors, with no purification required in between precursor additions. We utilized Sn-doped In_2O_3 (ITO) as a model system to evaluate the influence of radial dopant position on resulting properties, in this case the LSPR response. The core/shell nanostructure architectures were confirmed through bulk and surface elemental analysis.

Radial dopant placement has a profound influence on the LSPR energy, free electron concentration, and damping. Inactive Sn surface sites could be activated upon the addition of a thin (≤ 0.5 nm) In_2O_3 shell. In both types of core/shell nanocrystals, damping decreased relative to homogeneously-doped nanocrystals, due to the dopant-free region. ITO/In_2O_3

core/shell nanocrystals have the lowest damping, due to the dopant-free region at the surface, which reduces surface and impurity scattering, while increasing activation. This undoped region is crucial to realizing the theoretical minimum damping in metal-oxide nanocrystals, which has been a challenge in material development.

The ability to precisely control the radial placement of dopants creates opportunities in structure/property design and optimization. We foresee this approach ultimately being widely applicable to other metal oxide nanocrystal systems, whose properties are inhibited by dopant-scattering and localized-surface defects. Studies involving a combination of ultrafast optical spectroscopy and rigorous computational modeling will aid in developing a more comprehensive understanding of the underlying electronic structure of these materials and prove useful in tapping the nearly infinite compositions made possible through the control of dopant placement in these materials. This same approach should also be useful in modifying catalytic, magnetic, and electronic properties of nanocrystal extending beyond In_2O_3 systems.

Materials and methods.

Indium(III) acetate (99.99%), oleic acid (90% technical grade), and tin(IV) acetate were purchased from Sigma-Aldrich and used as received. Oleyl alcohol (80-85% technical grade) was purchased from Alfa Aesar and used as received. A flow meter purchased from Cole-Parmer was used to monitor nitrogen flow (model 03216-10).

Synthesis of Homogeneously-doped and Core/Shell Nanocrystals

All syntheses were carried out similar to those described in literature with modifications to control the placement of dopant atoms into the nanocrystal matrix.[32,33]

Synthesis of In_2O_3/ITO Core/shell Nanocrystals (Figures 5.2, C1, C3)

Two precursor solutions were prepared in separate vials. In one vial, indium(III) was mixed with of oleic acid (in a 1:6 molar ratio) to yield an undoped indium oleate precursor solution. In a separate vial, tin(IV) acetate and indium(III) acetate (in a 1:9 Sn:In ratio) were mixed with oleic acid (in a 1:6 metal to acid molar ratio) to yield a 10% Sn doped ITO precursor solution. Both precursors were left at 150 ^{o}C under N_2 for several hours. Indium oxide nanocrystals cores were synthesized by first adding the indium oleate precursor solution at a rate of 0.35 mL/min *via* syringe pump to 13.0 mL of oleyl alcohol at 290 ^{o}C. A 6.3 nm In_2O_3 core was grown in this manner, and a small aliquot was pulled out of the reaction flask using a 1.0 mL syringe. After the addition of the undoped precursor, a 10% ITO precursor solution was added to the reaction solution in the same manner described above. During the dropwise addition of the ITO precursor, small aliquots were taken out of the reaction vessel for analysis. Nanocrystals were isolated by precipitating with ~12 mL of ethanol. The solid was collected by centrifugation at 7000 rpm for 10 min. The solid was then washed and centrifuged once more with ethanol. Elemental analysis along with size and size dispersion analysis by SAXS from these particles can be found in Figure C1.

Synthesis of ITO/In_2O_3 Core/shell Nanocrystals (Figures 5.2, C2, C3)

For the synthesis of the ITO/In_2O_3core/shell nanocrystals, a 10% Sn ITO precursor solution was added to oleyl alcohol in the same manner described above. A 5.3 nm ITO core was grown in this manner, and a small aliquot was pulled out of the reaction flask using a 1.0 mL syringe. After the addition of the ITO precursor, an indium precursor solution was added to the reaction solution in the same manner described above. During the dropwise addition of the indium precursor, small aliquots were taken out of the reaction

vessel for analysis. Aliquots were purified and analyzed as stated above. Elemental analysis along with size and size dispersion analysis by SAXS from these particles can be found in Figure C2.

Synthesis of Homogeneously-doped ITO Nanocrystals (Figure 5.2, Tables C1 and C2): An ITO metal oleate precursor was prepared by mixing indium(III) acetate and tin(IV) acetate (in the proper molar ratio for the desired Sn doping level) in oleic acid (1:6 metal to acid molar ratio) in a scintillation vial. The solution was stirred at 150 ^{o}C under N_2 for several hours. Nanoparticles were formed by adding the precursor at a rate of 0.35 mL/min, using a syringe pump, to 13.0 mL of oleyl alcohol in a 100 mL three-neck flask at 290 ^{o}C. The three-neck flask was sealed with septa, however N_2 was allowed to flow over the solution at a rate of ~130 cc/min and exit out each of several purge needles. Aliquots were purified and analyzed as stated above.

Synthesis for Activation of Sn surfaces on an ITO Nanocrystal (Figure C4)

A 10% ITO precursor solution was added to oleyl alcohol in the same manner described above to yield a 6.9 nm ITO nanocrystal. An aliquot was taken at this point for analysis. Next, 20 drops of an undoped, indium oleate precursor was added to the reaction vessel. Another aliquot was taken at this point. Ten more drops of the indium oleate was added to the reaction vessel, another aliquot was taken, and finally ten more drops of undoped precursor was added to the vessel. Aliquots were purified and analyzed as stated above. Size and size dispersions from this synthesis can be found in Figure C4.

Synthesis of Doping Series: Homogeneously-doped and Core/shell Nanocrystals

Synthesis of the Homogeneously-doped ITO nanocrystals (Figure 5.4, Table 5.1)

A 3.3 % ITO metal oleate precursor was prepared by mixing indium(III) acetate (846 mg, 2.90 mmol) and tin(IV) acetate (35 mg, 0.10 mmol) in 6 mL of oleic acid in a scintillation vial. The solution was stirred at 150 ^{o}C under N_2 for several hours. Nanoparticles were formed by adding the precursor at a rate of 0.35 mL/min, using a syringe pump, to 13.0 mL of oleyl alcohol in a 100 mL three-neck flask at 290 ^{o}C. The three-neck flask was sealed with septa, however N_2 was allowed to flow over the solution at a rate of ~130 cc/min and exit out each of several purge needles. Aliquots were purified and analyzed as stated above. After collection, the final nanocrystals (350 mg, > 90% yield; yield for the nanocrystal core was calculated from the inorganic core mass (determined using Thermal Gravimetric Analysis from the mass isolated and the mass percent remaining after heating to 600 °C) and the theoretical maximum yield from the metal salts to form the metal oxide.

Synthesis of the ITO/In_2O_3 Core/shell Nanocrystals (Figure 5.4, Table 5.1)

Core/shell nanocrystals were prepared using the same method described above for homogeneously doped nanocrystals using different precursor solutions. Two precursor solutions were prepared in separate vials. In one vial, indium(III) acetate (584 mg, 2.00 mmol) was mixed with 4.0 mL of oleic acid to yield an undoped indium oleate precursor solution. In a separate vial, tin(IV) acetate (35 mg, 0.10 mmol) and indium(III) acetate (263 mg, 0.901 mmol) were mixed with 2.0 mL of oleic acid to yield a 10% doped ITO precursor solution. Both precursors were left at 150 ^{o}C under N_2 for several hours. Nanocrystals were synthesized by first adding the ITO precursor solution at a rate of 0.35 mL/min *via* syringe pump to 13.0 mL of oleyl alcohol at 290 ^{o}C. After the addition of the 2.0 mL precursor, the ITO precursor was removed from the syringe pump and replaced

with the indium oleate precursor. The indium oleate precursor was added *via* syringe pump to the reaction solution at the same addition rate. Aliquots were purified and analyzed as stated above, and yield determination of the nanocrystal products were carried as described above for homogeneously doped nanocrystals (355 mg, > 90% yield).

Synthesis of In_2O_3/ITO Core/shell Nanocrystals (Figure 5.4, Table 5.1)

10% ITO and indium oleate precursors were prepared in separate vials as described above. Nanocrystals were synthesized by first adding the undoped indium oleate precursor at a rate of 0.35 mL/min to 13.0 mL of oleyl alcohol at 290 ^{o}C the flask, then adding the ITO precursor. Precursors were added *via* a syringe pump and the nanocrystals were isolated and purified as described above (340 mg, > 90% yield.

Characterization of Indium Oxide and Sn-doped Indium Oxide Nanocrystals.

Optical measurements were carried out on a PerkinElmer (Waltham, MA) Lambda 1050 UV/Vis/NIR Spectrometer. Spectra were collected in CCl_4 using only one detector (PbS) in order to remove most detector artifacts. Samples were diluted to a concentration of ~0.5 mg/mL. Spectra were sampled from 1000 – 3300 nm with a scan resolution of 1 nm.

Elemental compositions of the nanocrystal cores were determined using a Teledyne Leeman Labs (Hudson, NH) Prodigy High Dispersion Inductively Coupled Plasma Optical Emission Spectrometer (ICP-OES). Nanocrystals were dried and digested in stock HCl for at least 48 hrs before being diluted for analysis.

Elemental composition for the surface of the nanoparticles was determined using a Thermo Scientific ESCALAB 250 X-ray Photoelectron Spectrometer (XPS). Samples were prepared by drop casting a hexanes solution onto mica substrates. Surface tin content

was determined by integrating the tin $3d_{5/2}$ peaks and comparing those intensities to those of the indium $3d_{5/2}$ peaks.

Transmission electron microscopy (TEM) micrographs were collected using a FEI Tecnai Spirit TEM (Hillsboro, OR) operating at 120 kV. HRTEM images (Figure C1) were collected on a 300 kV C_s image corrected FEI Titan (S)TEM. Nanocrystals were imaged on Ted Pella (Redding, CA) lacey carbon grids supported by a copper grid. Samples were prepared by dropping a sample dissolved in hexanes onto the water surface in a small vial, allowing the hexanes to dissolve, and dipping a grid through the layer of particles.

Small-angle X-ray scattering (SAXS) analysis was done on a lab-scale SAXS (SAXSess, Anton Paar, Austria). The system was attached to an X-ray generator equipped with an X-ray tube (Cu Kα, wavelength $\lambda = 0.154$ nm) operating at 40 kV and 50 mA. The scattered X-ray intensities were measured with a charge-coupled device detector (Roper Scientific, Germany). The raw data was processed with SAXSquant software (version 2.0). Scattering curves were averaged over 50 individual curves for various acquisition times (0.25-15s). Curve fitting was done using Irena macros for IGOR (V. 6.3.7.2).[57]

Drude modeling was performed in MatLab. Models were fitted manually to simulated spectra through a combination of Equations 1-4. Models were allowed to optimize to a least-squared fit, with extracted value errors of 25 cm^{-1}. This approach has been used extensively to model LSPR spectra of metal oxide, and metal chalcogenide nanocrystals.[40-42]

Bridge to Chapter VI

The following concluding chapter offers concluding remarks regarding living nanocrystal growth, with an eye toward future opportunities.

CHAPTER VI

CONCLUSION

Concluding Remarks

Nanocrystals and nanoparticles offer advantages in both application assembly and performance, and promise to improve the lives of humanity in the coming years. Though colloidal nanomaterials synthesis has advanced tremendously over the past four decades, our ability to produce precision materials, tailored for specific use or property exploration, remains limited. Just as polymer chemists lacked the synthetic ability to test basic structure/property theories in the early 1950s, the approaches available to nanochemists today are limited in the size, composition, and architecture of nanomaterials they can produce.

Colloidal living growth approaches offer the incredible ability to quickly and intuitively synthesize complex nanomaterial structures and compositions, so new phenomena can be understood and harnessed. Living growth is possible when the production and maintenance of reactive sites on the surface facilitate growth through the controlled addition of reactive monomers. This type of growth mechanism has several consequences; because growth occurs by monomer addition rather than heterogeneous

nucleation, epitaxial growth of single crystal nanoparticles results. Further, continuous growth from "living" reactive sites on the particle surface leads to nanocrystals with low size dispersions. When monomer addition is irreversible, crystals are no longer susceptible to ripening. At the same time, when crystals are stabilized against core fusion or aggregation by a surface-bound surfactant, a constant number of nanocrystals persists throughout the growth process. When a constant number of crystals is maintained for the entire growth process, addition of more precursor leads to *predictable* growth. Finally, the preservation of reactive species in a controlled, layer-by-layer growth process provides opportunities introduce new elements, thus altering the composition and structure of the nanocrystal with sub-nanometer precision, affording access to novel doped and core/shell structures.

Future Opportunities

Discovery and development of new living growth methods for nanocrystals will require greater understanding of key mechanistic aspects of these processes. Perhaps the most important aspect for exploration is understanding the nanocrystal surface chemistry during growth. In order to support a living growth process, there must be a complex interplay of 1) ligand binding to promote particle stability, and 2) appropriately reactive surface promoting epitaxial growth through monomer addition. Although some mechanistic understanding can be inferred from particle growth studies over time, *in situ* and *ex situ* experiments to probe the surface chemistry will be needed. Investigation into the influence of ligand type and concentration, characterization of the structure of metal precursor, and examination of the growth behavior during different addition rates, and at different reaction temperatures, will be needed to advance our understanding of these

systems. Direct characterization of the surface chemistry may be more difficult to obtain. Studies should target the chemical makeup of the reactive nanocrystal surface, structure of reactive monomer produced from precursors, and nuclei or clusters formed early in the growth process through detailed, likely *in situ*, chemical analysis.

Many of the answers to these questions will require more advanced analytical tools and rigorous analysis of nanocrystal growth mechanisms. Cutting-edge analytical tools are needed to monitor nucleation and nanocrystal growth, assess atomic-scale compositional and structural changes over time, as well as monitor functional groups participating in living growth processes.[1–3] We have found SAXS an invaluable tool to quickly probe the products of new synthetic routes and monitor nanocrystal growth. Lab-scale SAXS instruments are now more widely available and offer the capability to quickly obtain size, size dispersion, and concentration measurements. Compared to TEM, SAXS analysis can obtain information from a statistically significant population of nanoparticles in a fraction of the time that image analysis takes, and it offers the added benefit of probing nanoparticle size, shape, and structure in solution.[4] Of course, TEM maintains its value in identifying shape and corroborating SAXS measurements. Furthermore, HRTEM measurements are necessary to characterize crystallinity of synthesized products. Atomic pair distribution function analysis (PDF) is a powerful tool that can probe species at the atomic level, and should provide significant insights regarding reactive monomer formation, nucleation, and growth.[5–7] PDF should be especially useful for probing the structures of very small species (e.g. monomers and nuclei) that are not easily detected and characterized by SAXS or TEM. Towards monitoring key functional groups in monomers and on nanocrystal surfaces, we believe

that traditional small-molecule chemical analysis tools, including NMR, IR, and Raman spectroscopy, together with complementary surface chemistry tools, such as XPS or ToF-SIMS, can be used alongside more sophisticated methods to enhance our mechanistic understanding of living growth processes.

Conclusion

Despite the challenges evident in discovering new living growth systems and elucidating the mechanisms, the future of precision nanomaterial production through these approaches is promising and inspiring. It appears that living growth methods are widely applicable across the periodic table, employing single metals or several metals in combination. From what we have seen so far, these mechanisms facilitate the convenient and rapid assembly of new nanostructures with advantageous and appealing properties. At the same time, these intuitive synthetic approaches produce high-performance nanomaterials in fewer steps, in higher yields, and under greener conditions than thermal decomposition methods. Already, the synthesis of an almost-infinite number of binary, doped, co-doped, and core/shell oxide nanocrystal structures is possible by living growth. Products of these syntheses promise increased performance in optical, electronic, and catalytic application, as well as provide avenues for understanding fundamental physical processes. With respect to the compositions and structures that can be produced via these methods, we have only scratched the surface. We expect living approaches will make it possible to produce shape-controlled nanostructures, ternary oxides, and other chalcogenide nanocrystals (not limited to oxides).[8] Indeed, growing metal chalcogenides may be possible by incorporating a chalcogenide source. For example, many indium phosphide syntheses utilize the dehalosilylation of tris(trimethylsilyl)phosphine

($P(SiMe_3)_3$) with the similar metal precursors as the living methods we have described above.[9,10] Some existing approaches to arsenide nanocrystals may in time prove to be living mechanisms.[8] Development of living growth approaches to these traditionally highly-sought materials would greatly increase the number of new structures that are possible, while simultaneously decreasing synthetic burden. Further, the ability to easily and predictably combine materials in unique, epitaxial heterostructured compositions will bring about a flurry in discovery-driven science.

APPENDIX A

SUPPORTING INFORMATION FOR CHAPTER III: CONTINUOUS GROWTH OF METAL OXIDE NANOCRYSTALS: ENHANCED CONTROL OF NANOCRYSTAL SIZE AND RADIAL DOPANT DISTRIBUTION

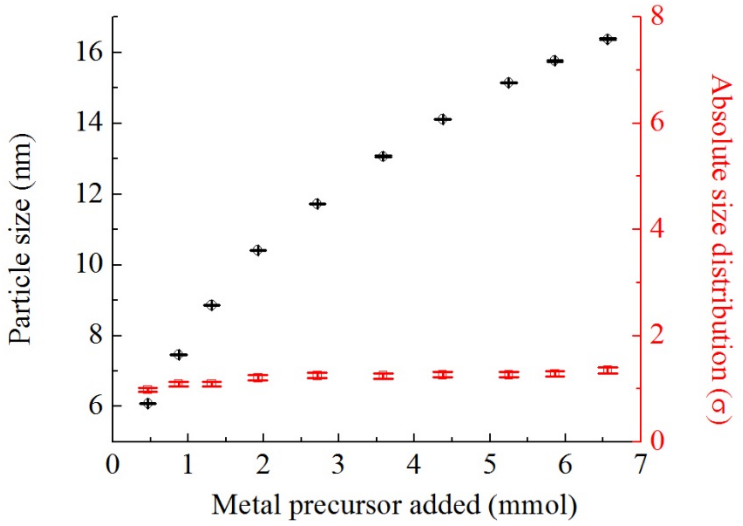

Figure A1. Figure 3.2a from the manuscript replotted with absolute size distribution (in nm) instead of relative size distribution shown in the manuscript.

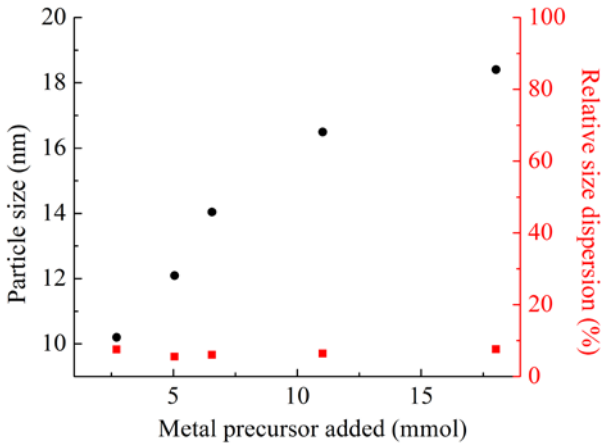

Figure A2. Particle size and size dispersion measured from TEM. While TEM and SAXS yield different sizes and size dispersions for nanocrystals based on number-weighted and volume-weighted analysis respectively, the TEM data illustrate the same trend of increasing particle size with precursor added. Over 300 particles were measured for each data point.

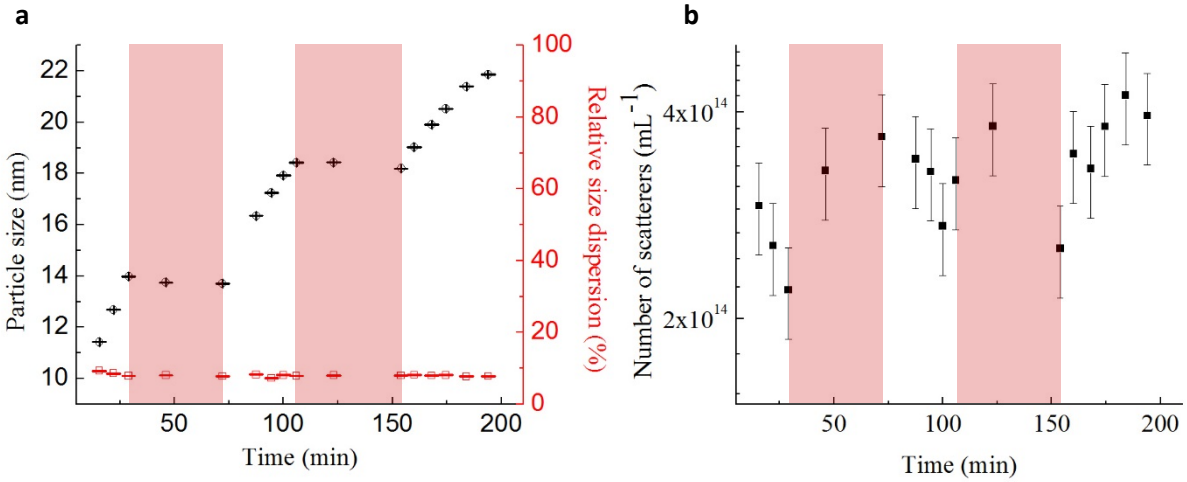

Figure A3. SAXS data from the synthesis of large In_2O_3 nanocrystals. In order to synthesize larger nanocrystals, excess alcohol must be added to the reaction flask to ensure further esterification and nanocrystal growth as metal oleate is slowly added. During this synthesis, metal oleate was first added dropwise to the reaction flask. Precursor addition was then stopped, and oleyl alcohol was added dropwise (alcohol addition is noted in the red transparent rectangle). This cycle was then repeated. See methods section for specific details of synthesis. As shown in **a**, particle size increases as metal oleate is added, and remains nearly constant while precursor addition stops. (**b**) Number of scatterers from SAXS shows nearly constant nanocrystal concentration over time. Error bars represent standard deviation of the measurement. If a larger excess of alcohol is added to the reaction flask before metal precursor addition begins, smaller nanocrystals are produced compared to the method described here. Therefore, precursor and alcohol were added in an alternating fashion, as shown above.

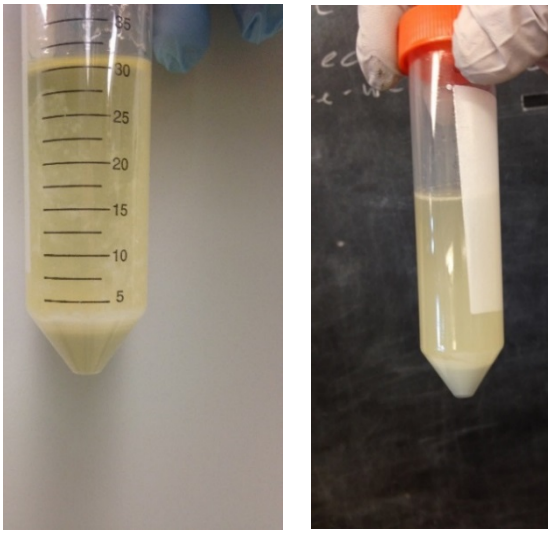

Figure A4. Multigram quantities of In_2O_3 nanocrystals produced. Each centrifuge tube above contains half of the reaction solution described in Figure A2 and in methods sections. After the synthesis, over 3.0 g of nanocrystals were recovered, seen as the solid precipitate in the above figure.

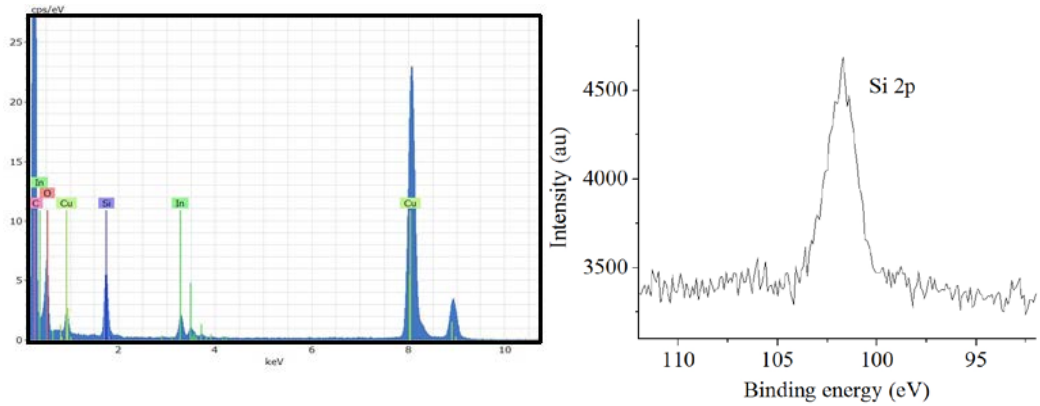

Figure A5. Top left: EDX spectrum of nanocrystals after treatment with trimethoxy(octadecyl)silane. Nanocrystals (which have been twice precipitated with ethanol, isolated by centrifugation and dispersed in hexanes) show the presence of silicon from the coupled silane along with indium and oxygen from In_2O_3 nanocrystals. Copper is present from the TEM grid. Because silicon may be present from the EDX detector, we confirmed the presence of silicon with XPS. Right: XPS Si 2p peak from the same particles.

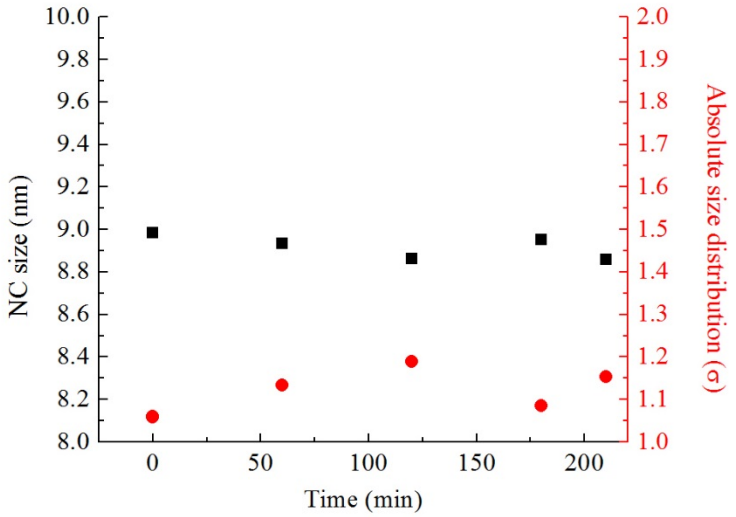

Figure A6. SAXS data of In_2O_3 nanocrystals left under reaction conditions (290 ^oC) after the injection of metal precursor. Very little change in the size or size distribution (nm) is observed for three hours following synthesis.

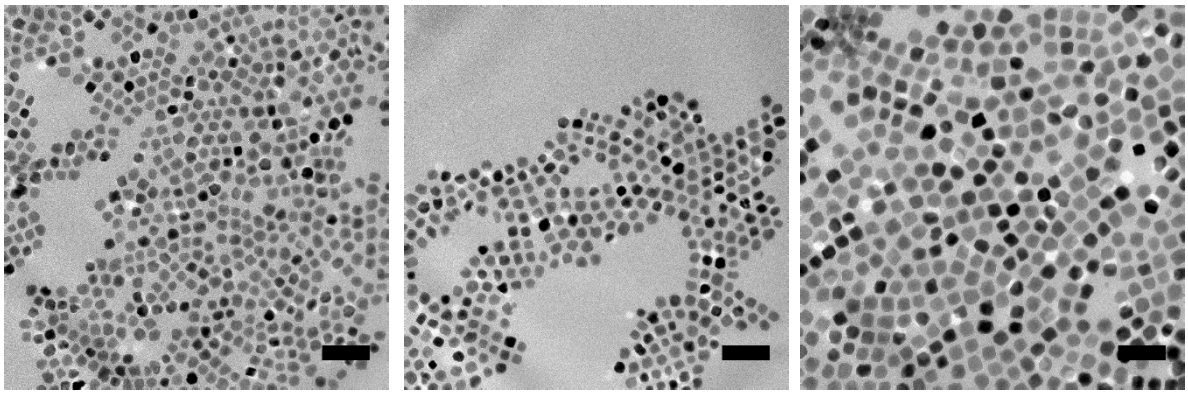

Figure A7. TEM of 8.9 nm In_2O_3 core (left), 10.4 nm In_2O_3/ITO core/shell (middle), and 13.6 nm In_2O_3/ITO/In_2O_3 core/shell/shell nanocrystals. XPS data from the nanocrystals are displayed in Fig. 8 of the manuscript. Scale bars are 50 nm.\

APPENDIX B

SUPPORTING INFORMATION FOR CHAPTER IV: TRANSITION METAL-DOPED METAL OXIDE NANOCRYSTALS: EFFICIENT SUBSTITUTIONAL DOPING THROUGH A CONTINUOUS GROWTH PROCESS

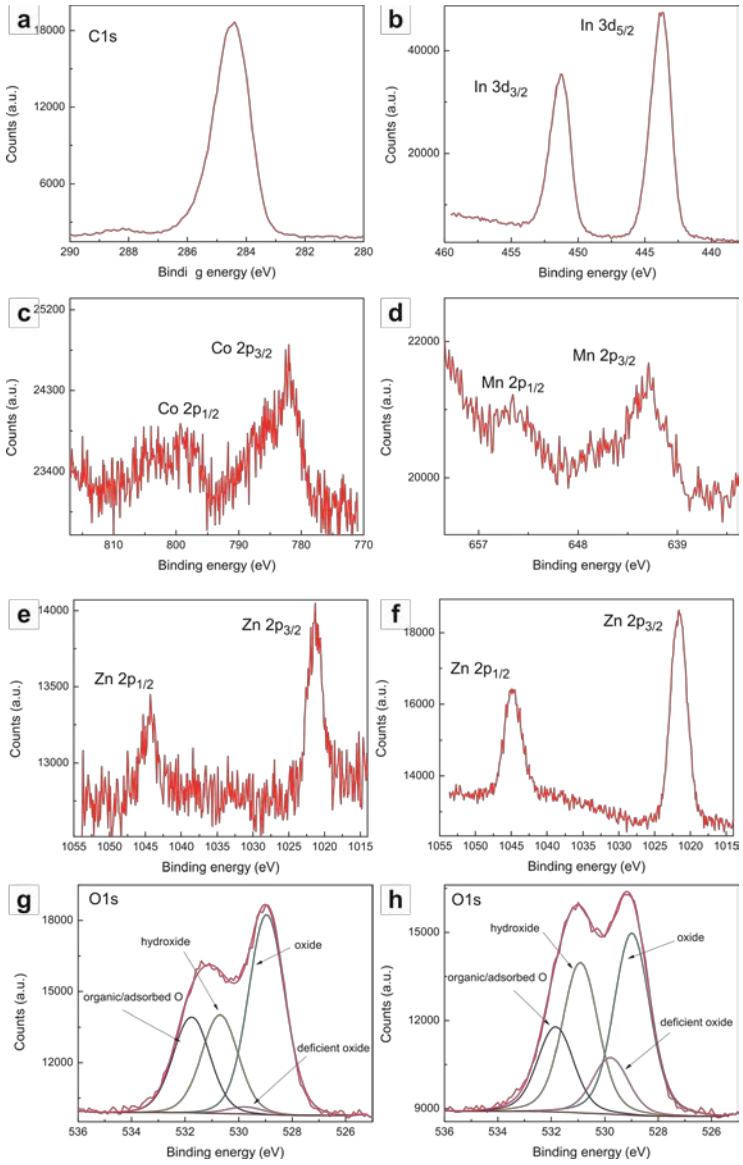

Figure B1. XPS spectra of doped In_2O_3 nanocrystals. Compositions shown in Table 3 of the manuscript are calculated based on integration of the In $3d_{5/2}$ and dopant $2p_{3/2}$ peak. **a**) displays a typical C1s spectra and **b**) a typical In 3d spectra of the doped and undoped nanocrystals. **c**) and **d**) show the Co and Mn 2p spectra from Co: In_2O_3 and Mn: In_2O_3 respectively. **e**) and **f**) display the Zn 2p region of 5% Zn: In_2O_3 and 20% Zn: In_2O_3, respectively. **g**) displays the O1s spectra from 5% Zn: In_2O_3, and **h**) 20% Zn: In_2O_3. The O1s spectra shown in **g** and **h** can be fit to four peaks of the same peak shape and a width of 1.5 eV; the peak at 529.0 eV corresponds to oxide in In_2O_3, the peak 0.7 eV greater corresponds to oxygen deficient/defect oxide, the peak at 530.9 eV corresponds to hydroxide, and the peak at 531.8 eV corresponds to adsorbed oxygen and organic oxygen in the ligand shell.[1–5] The increase in dopant atom concentration likely leads to the

increase in oxygen vacancy formation, which displayed in **g** and **h**. Spectra are referenced to the C1s hydrocarbon peak at 284.5 eV.

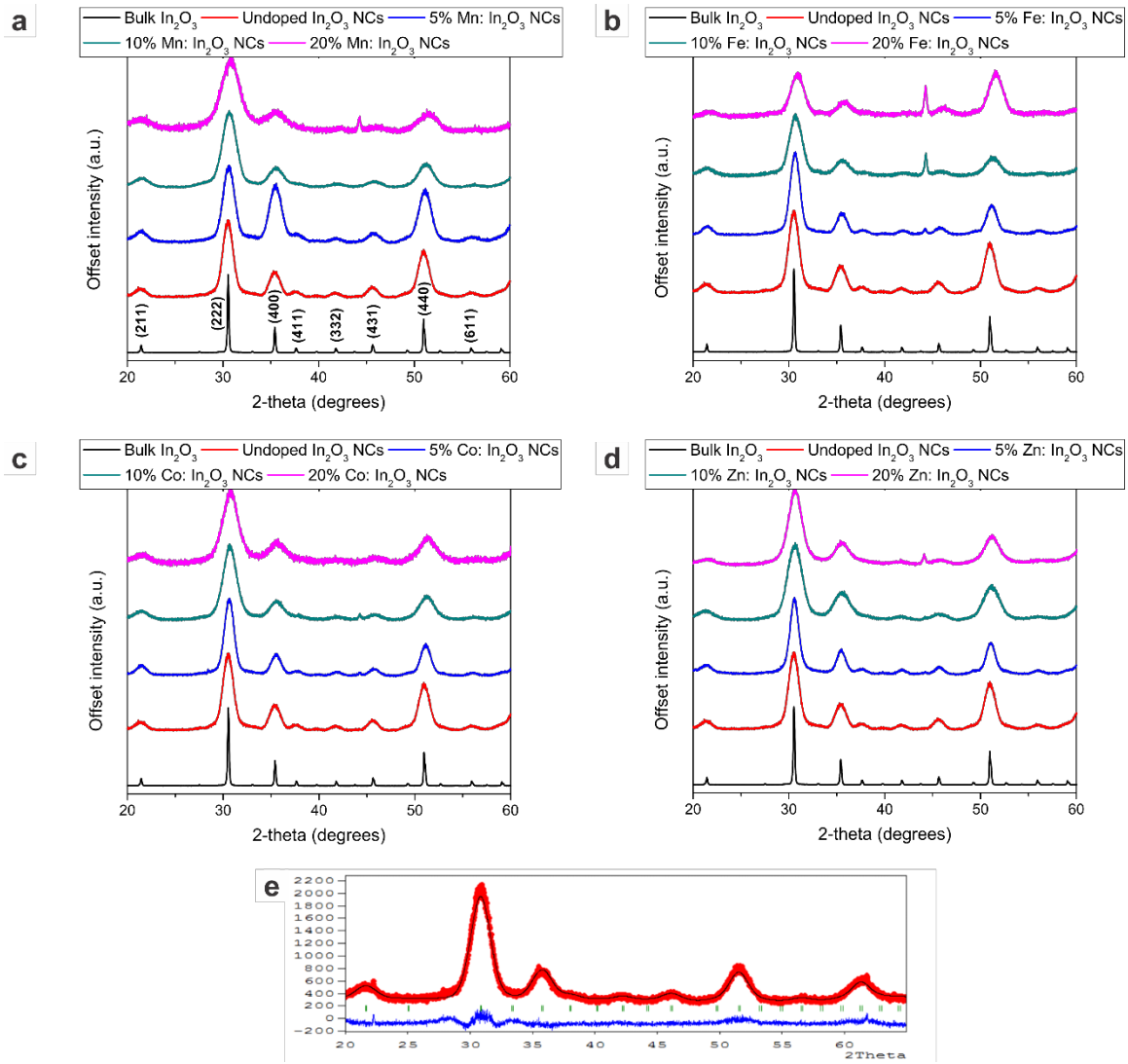

Figure B2. Raw XRD patterns acquired from undoped and doped In_2O_3 nanocrystals at varying dopant concentrations, re-plotted from Figure 2 in the manuscript: **a**) Mn: In_2O_3 **b**) Fe: In_2O_3 **c**) Co: In_2O_3 **d**) Zn: In_2O_3. The peak present at 43.5 ^{o} in some samples is due to the silicon substrate. All acquired patterns match that of cubic In_2O_3 (bulk pattern shown in black in each plot). **e**) Displays a typical Rietveld refinement using Fullprof Suite.[6] Background points were picked by hand, and peaks were fit using a pseudo-Voigt profile. Once scale, zero offsets, and peak shape were refined, lattice parameters were allowed to optimize. In XRD patterns where the substrate peak is present, an exclusion zone in the refinement was added to prevent model optimization from 43-44 ^{o}.

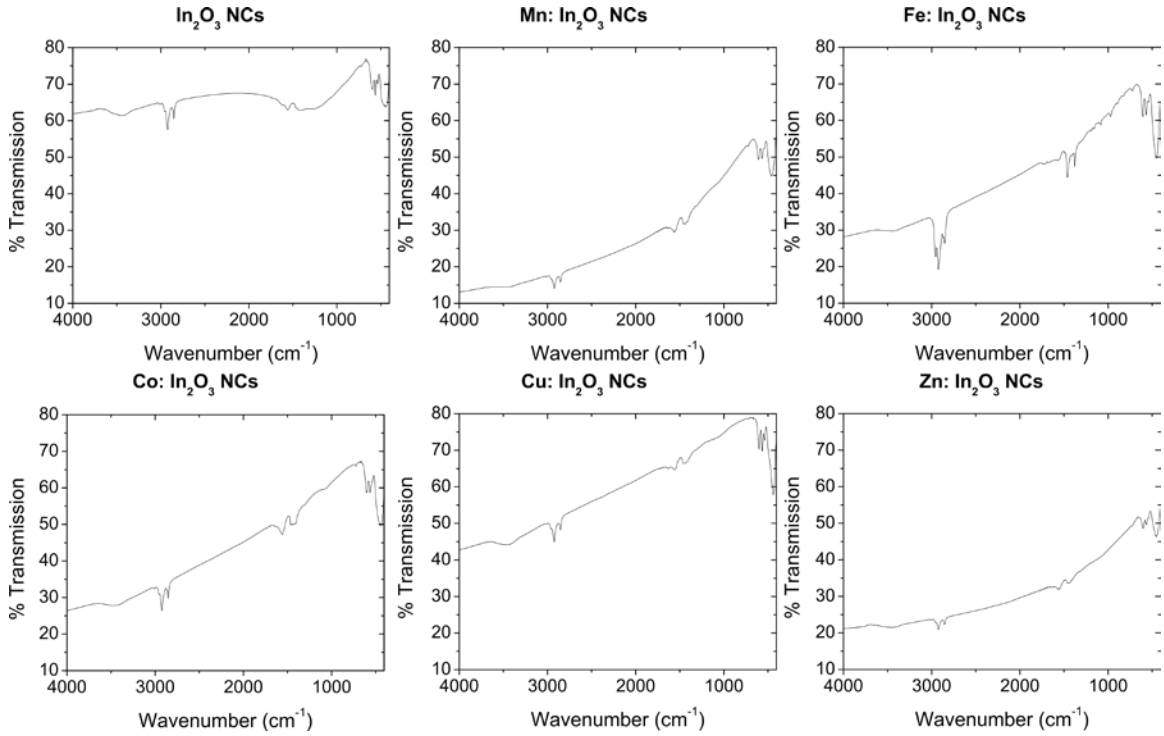

Figure B3. FTIR spectra obtained from undoped and doped In_2O_3 nanocrystals. Unlike the undoped nanocrystals (top left), which display a weak plasmon resonance ~1400 cm^{-1}, the doped nanocrystals display much stronger plasmon absorbances centered at energies > 4000 cm^{-1}. The strong absorbance and the shift of the LSPR to higher energies is an indication of an increased concentration of oxygen vacancy formation.

APPENDIX C

SUPPORTING INFORMATION FOR CHAPTER V: RADIAL DOPANT PLACEMENT FOR TUNING PLASMONIC PROPERTIES IN METAL OXIDE NANOCRYSTALS

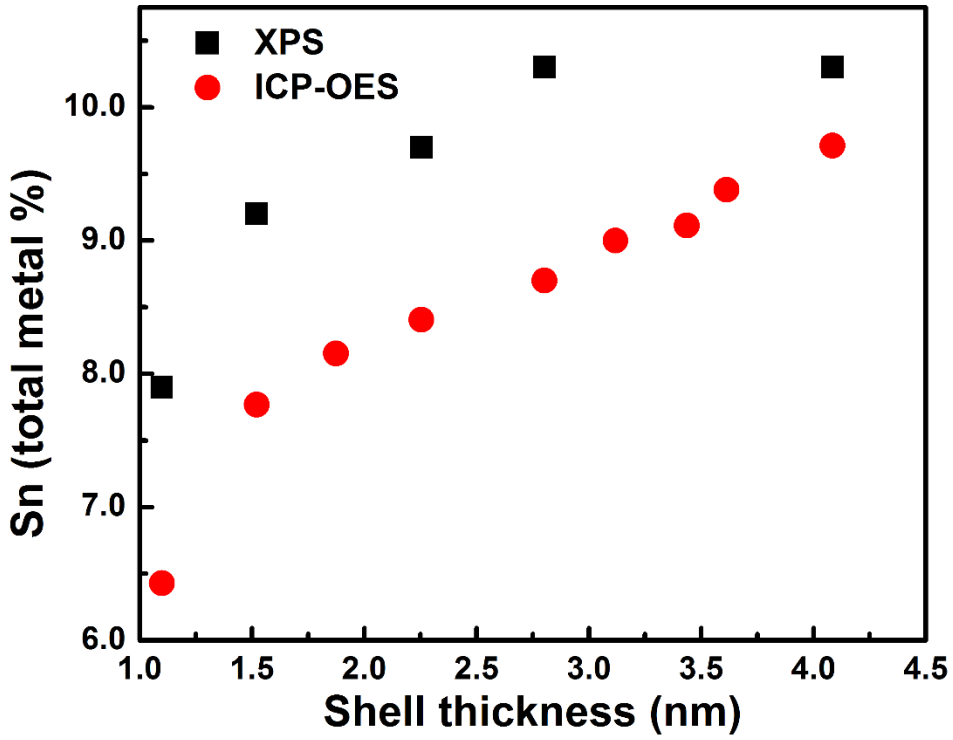

Sample	Core size (nm)	Dispersity (1σ, nm)	Shell thickness (nm)
In_2O_3 core	6.3	0.8	-
In_2O_3/ITO core/shell	8.5	1.0	1.1
In_2O_3/ITO core/shell	9.3	1.0	1.5
In_2O_3/ITO core/shell	10.0	1.1	1.9
In_2O_3/ITO core/shell	10.8	1.2	2.3
In_2O_3/ITO core/shell	11.9	1.4	2.8
In_2O_3/ITO core/shell	12.5	1.7	3.1
In_2O_3/ITO core/shell	13.1	1.8	3.4
In_2O_3/ITO core/shell	13.5	1.8	3.6
In_2O_3/ITO core/shell	14.4	2.2	4.1

Figure C1. (Top) Elemental analysis of Sn (plotted as total metal %) via XPS and ICP-OES versus shell thickness for In_2O_3/ITO core/shell series. The trend shows an overall increase in Sn with increasing ITO shell thickness. Additionally, measured XPS values are larger than ICP-OES values indicating the dopants are localized in the shell. (Bottom) Size and size dispersion from SAXS analysis for the In_2O_3/ITO core/shell nanocrystal series. LSPR spectra are shown in Figure 2e in the manuscript.

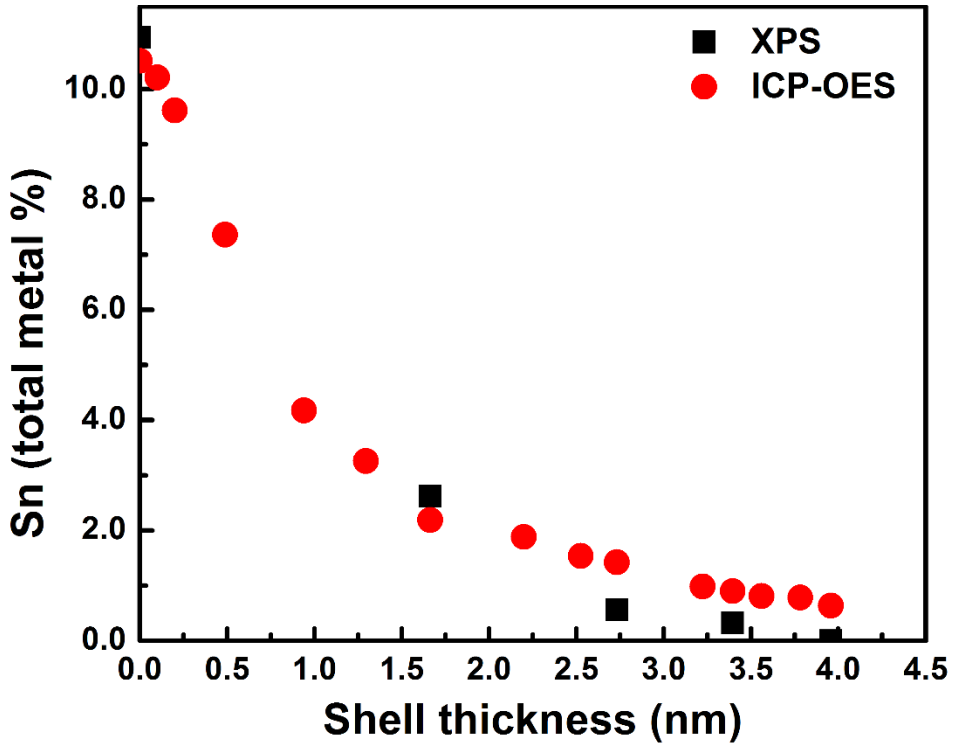

Sample	Core size (nm)	Dispersity (1σ, nm)	Shell thickness (nm)
ITO core	5.3	2.3	-
ITO/In_2O_3 core/shell	6.3	1.4	0.5
ITO/In_2O_3 core/shell	7.2	1.1	0.9
ITO/In_2O_3 core/shell	7.9	0.9	1.3
ITO/In_2O_3 core/shell	8.7	1.0	1.7
ITO/In_2O_3 core/shell	9.7	1.1	2.2
ITO/In_2O_3 core/shell	10.4	1.2	2.5
ITO/In_2O_3 core/shell	10.8	1.2	2.7
ITO/In_2O_3 core/shell	11.2	1.2	2.9
ITO/In_2O_3 core/shell	11.8	1.3	3.2
ITO/In_2O_3 core/shell	12.1	1.3	3.4
ITO/In_2O_3 core/shell	12.4	1.3	3.6
ITO/In_2O_3 core/shell	12.9	1.3	3.8
ITO/In_2O_3 core/shell	13.2	1.3	4.0
ITO/In_2O_3 core/shell	13.3	1.2	4.0

Figure C2. (Top) Elemental analysis of Sn (plotted as total metal %) via XPS and ICP-OES versus shell thickness for ITO/ In_2O_3 core/shell series. The trend shows an overall decrease in Sn with increasing In_2O_3 shell thickness. Additionally, XPS values trend to zero indicating the dopants are localized in the core. (Bottom) Size and size dispersion from SAXS analysis for the ITO/ In_2O_3 core/shell nanocrystal series.

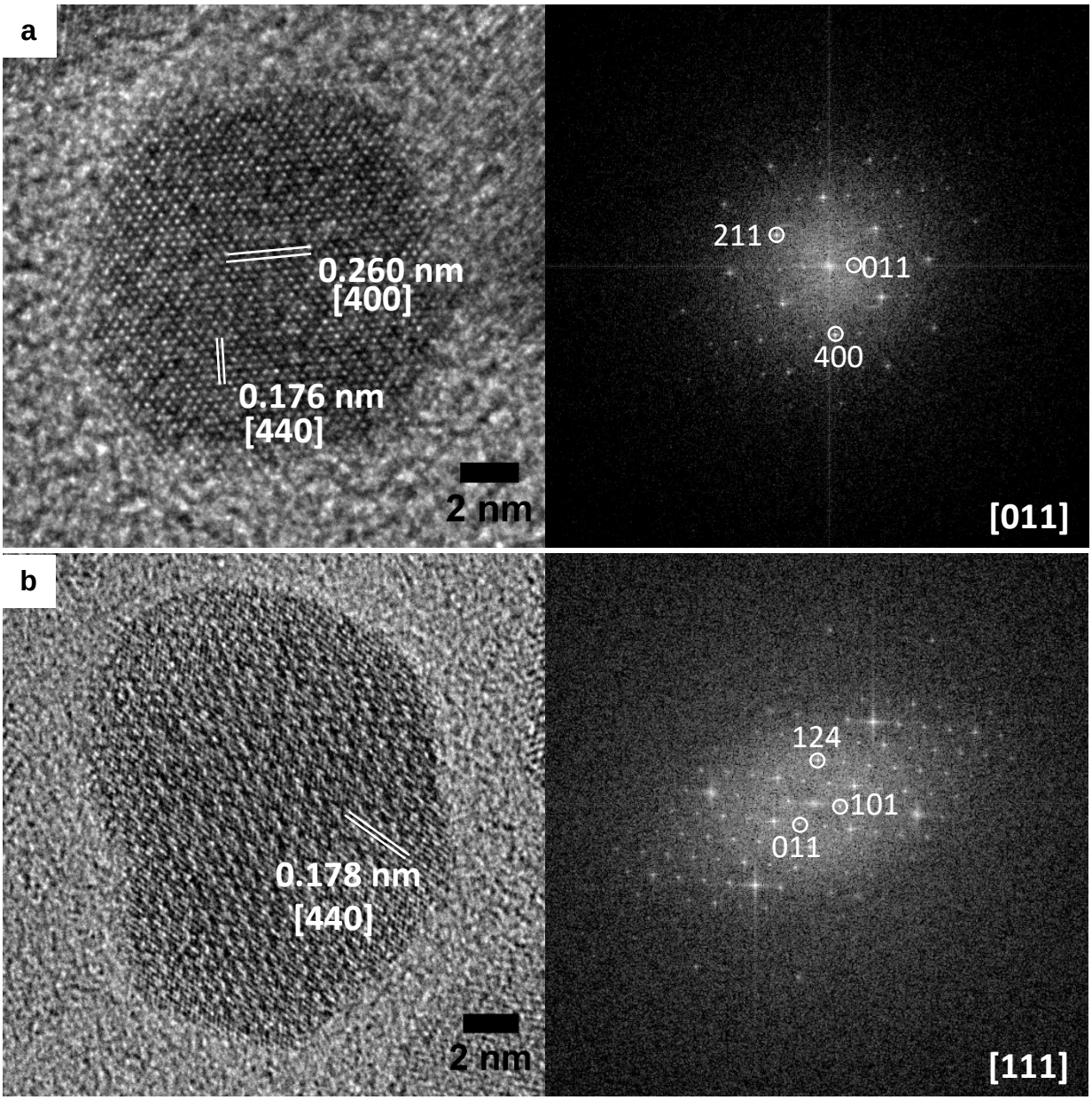

Figure C3. HRTEM images of ITO/In_2O_3 core/shell nanocrystal (**a**) and the In_2O_3/ITO core/shell nanocrystal (**b**). As shown, no striking structural defects are found in the single crystals. The FFT of the image is shown to the right of the micrographs. The micrograph in **a** is looking down the [011] zone axis, and the micrograph in **b** is down the [111] zone axis.

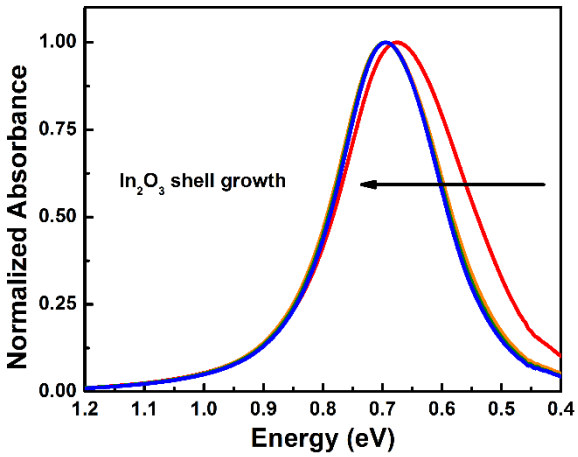

Sample	Core size (nm)	Dispersity (1σ, nm)
ITO core	6.9	1.0
ITO/In_2O_3 core/shell	7.0	1.2
ITO/In_2O_3 core/shell	7.1	1.1
ITO/In_2O_3 core/shell	7.2	1.1

Figure C4. (Top) NIR spectra of ITO nanocrystal core with sub-namometer shells. (Bottom) Size and size dispersion from SAXS analysis for the ITO/In_2O_3 core/shell nanocrystals with thin undoped shells.

Table C1. Size and composition data for homogeneous ITO and In_2O_3/ITO core/shell nanocrystals shown in Figure 5.2g. Sizes and size dispersions are from SAXS analysis. Elemental analyses are derived from XPS and ICP-OES.

Structure	Size +/- 1σ (SAXS, nm)	Core size (SAXS, nm)	Sn % (ICP-OES)	Sn % (XPS)
ITO homogeneous	7.3 ± 1.1	N/A	9.98 ± 0.05	10.6 ± 0.2
In_2O_3/ITO core/shell	14.4 +/- 2.2	6.3 +/- 0.8	9.71 ± 0.06	10.3 ± 0.1

Table C2. Size and composition for homogeneous ITO and ITO/In_2O_3core/shell nanocrystals shown in Figure 5.2h. Size and size dispersion are from SAXS analysis. Elemental analyses are derived from XPS and ICP-OES.

Structure	Size +/- 1σ (SAXS, nm)	Core size (SAXS, nm)	Sn % (ICP-OES)	Sn % (XPS)
ITO homogeneous	6.9 ± 1.0	N/A	7.17 ± 0.06	7.1 ± 0.2
ITO/In_2O_3 core/shell	7.9 +/- 0.9	5.3 +/- 2.3	7.36 ± 0.04	7.5 ± 0.1

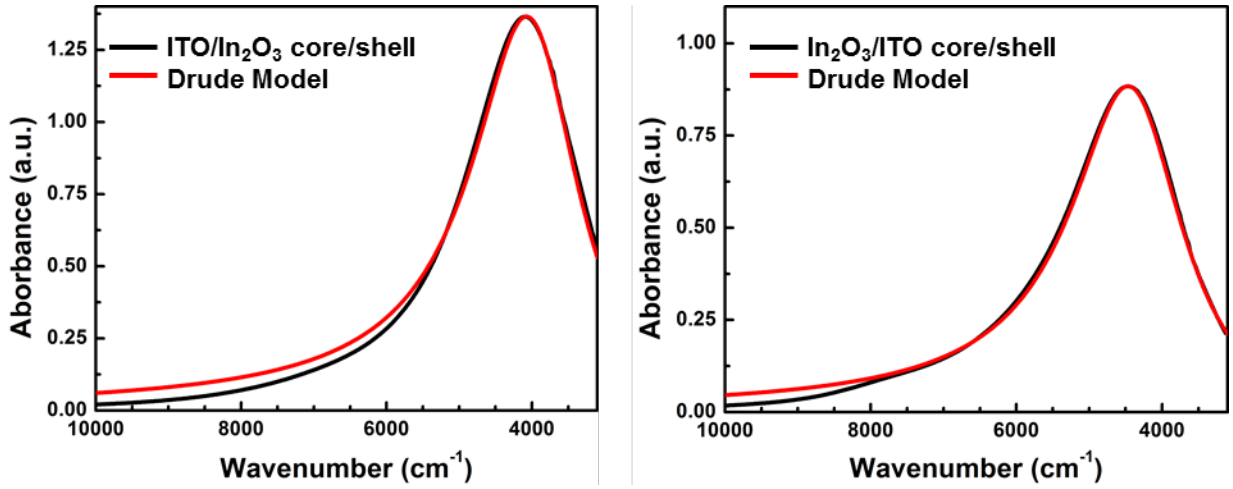

Figure C5. Example spectra modeling with the Drude equation of ITO/In_2O_3 nanocrystals (left) and In_2O_3/ITO nanocrystals (right). Modeling was performed in MatLab as described in the Experimental section of the main text.

REFERENCES CITED

Chapter I

(1) Nakhleh, M. K.; Amal, H.; Jeries, R.; Broza, Y. Y.; Aboud, M.; Gharra, A.; Ivgi, H.; Khatib, S.; Badarneh, S.; Har-Shai, L.; *et al.* Diagnosis and Classification of 17 Diseases from 1404 Subjects via Pattern Analysis of Exhaled Molecules. *ACS Nano* **2017**, *11*, 112–125.

(2) Choi, J.-H.; Wang, H.; Oh, S. J.; Paik, T.; Sung, P.; Sung, J.; Ye, X.; Zhao, T.; Diroll, B. T.; Murray, C. B.; *et al.* Exploiting the Colloidal Nanocrystal Library to Construct Electronic Devices. *Science* **2016**, *352*, 205–208.

(3) Talapin, D. V.; Lee, J.-S.; Kovalenko, M. V.; Shevchenko, E. V. Prospects of Colloidal Nanocrystals for Electronic and Optoelectronic Applications. *Chem. Rev.* **2010**, *110*, 389–458.

(4) Mulvaney, P. Surface Plasmon Spectroscopy of Nanosized Metal Particles. *Langmuir* **1996**, *12*, 788–800.

(5) Link, S.; El-Sayed, M. A. Spectral Properties and Relaxation Dynamics of Surface Plasmon Electronic Oscillations in Gold and Silver Nanodots and Nanorods. *J. Phys. Chem. B* **1999**, *103*, 8410–8426.

(6) Chen, X.; Li, C.; Gratzel, M.; Kostecki, R.; Mao, S. S. Nanomaterials for Renewable Energy Production and Storage. *Chem. Soc. Rev.* **2012**, *41*, 7909–7937.

(7) Astruc, D.; Lu, F.; Aranzaes, J. R. Nanoparticles as Recyclable Catalysts: The Frontier between Homogeneous and Heterogeneous Catalysis. *Angew. Chem. Int. Ed.* **2005**, *44*, 7852–7872.

(8) Saha, K.; Agasti, S. S.; Kim, C.; Li, X.; Rotello, V. M. Gold Nanoparticles in Chemical and Biological Sensing. *Chem. Rev.* **2012**, *112*, 2739–2779.

(9) Park, J.; Joo, J.; Kwon, S. G.; Jang, Y.; Hyeon, T. Synthesis of Monodisperse Spherical Nanocrystals. *Angew. Chem. Int. Ed.* **2007**, *46*, 4630–4660.

(10) Thanh, N. T. K.; Maclean, N.; Mahiddine, S. Mechanisms of Nucleation and Growth of Nanoparticles in Solution. *Chem. Rev.* **2014**, *114*, 7610–7630.

(11) Hendricks, M. P.; Campos, M. P.; Cleveland, G. T.; Jen-La Plante, I.; Owen, J. S. A Tunable Library of Substituted Thiourea Precursors to Metal Sulfide Nanocrystals. *Science* **2015**, *348*, 1226–1230.

(12) Campos, M. P.; Hendricks, M. P.; Beecher, A. N.; Walravens, W.; Swain, R. A.; Cleveland, G. T.; Hens, Z.; Sfeir, M. Y.; Owen, J. S. A Library of Selenourea Precursors to PbSe Nanocrystals with Size Distributions near the Homogeneous Limit. *J. Am. Chem. Soc.* **2017**.

(13) Reiss, P.; Carrière, M.; Lincheneau, C.; Vaure, L.; Tamang, S. Synthesis of Semiconductor Nanocrystals, Focusing on Nontoxic and Earth-Abundant Materials. *Chem. Rev.* **2016**, *116*, 10731–10819.

(14) Watzky, M. A.; Finke, R. G. Nanocluster Size-Control and "Magic Number" Investigations. Experimental Tests of the "Living-Metal Polymer" Concept and of Mechanism-Based Size-Control Predictions Leading to the Syntheses of Iridium(0) Nanoclusters Centering about Four Sequential Magic Numbers. *Chem. Mater.* **1997**, *9*, 3083–3095.

(15) van Embden, J.; Chesman, A. S. R.; Jasieniak, J. J. The Heat-Up Synthesis of Colloidal Nanocrystals. *Chem. Mater.* **2015**, *27*, 2246–2285.

(16) Lee, J.; Zhang, S.; Sun, S. High-Temperature Solution-Phase Syntheses of Metal-Oxide Nanocrystals. *Chem. Mater.* **2013**, *25*, 1293–1304.

(17) Wang, F.; Richards, V. N.; Shields, S. P.; Buhro, W. E. Kinetics and Mechanisms of Aggregative Nanocrystal Growth. *Chem. Mater.* **2014**, *26*, 5–21.

(18) Leskelä, M.; Ritala, M. Atomic Layer Deposition Chemistry: Recent Developments and Future Challenges. *Angew. Chem. Int. Ed.* **2003**, *42*, 5548–5554.

(19) Herman, M. A.; Sitter, H. *Molecular Beam Epitaxy: Fundamentals and Current Status*; Springer Science & Business Media, 2012; Vol. 7.

(20) Stein, A.; Keller, S. W.; Mallouk, T. E. Turning Down the Heat: Design and Mechanism in Solid-State Synthesis. *Science* **1993**, *259*, 1558–1564.

(21) Hornbostel, M. D.; Hyer, E. J.; Thiel, J.; Johnson, D. C. Rational Synthesis of Metastable Skutterudite Compounds Using Multilayer Precursors. *J. Am. Chem. Soc.* **1997**, *119*, 2665–2668.

(22) Mann, S. *Biomineralization: Principles and Concepts in Bioinorganic Materials Chemistry*; Oxford University Press on Demand, 2001; Vol. 5.

(23) Szwarc, M. Living Polymers. Their Discovery, Characterization, and Properties. *J. Polym. Sci. Part Polym. Chem.* **1998**, *36*, IX–XV.

(24) LaMer, V. K.; Dinegar, R. H. Theory, Production and Mechanism of Formation of Monodispersed Hydrosols. *J. Am. Chem. Soc.* **1950**, *72*, 4847–4854.

Chapter II

(1) Szwarc, M. Living Polymers. Their Discovery, Characterization, and Properties. *J. Polym. Sci. Part Polym. Chem.* **1998**, *36*, IX–XV.

(2) Patterson, G. Sixty Years of Living Polymers. *Nature* **2016**, *536*, 276–278.

(3) Szwarc, M. /`Living/' Polymers. *Nature* **1956**, *178*, 1168–1169.

(4) Webster, O. W. Living Polymerization Methods. *Science* **1991**, *251*, 887–893.

(5) Watzky, M. A.; Finke, R. G. Nanocluster Size-Control and “Magic Number” Investigations. Experimental Tests of the “Living-Metal Polymer” Concept and of Mechanism-Based Size-Control Predictions Leading to the Syntheses of Iridium(0) Nanoclusters Centering about Four Sequential Magic Numbers. *Chem. Mater.* **1997**, *9*, 3083–3095.

(6) Yin, Y.; Alivisatos, A. P. Colloidal Nanocrystal Synthesis and the Organic-Inorganic Interface. *Nature* **2005**, *437*, 664–670.

(7) Steigerwald, M. L.; Brus, L. E. Semiconductor Crystallites: A Class of Large Molecules. *Acc. Chem. Res.* **1990**, *23*, 183–188.

(8) Park, J.; Joo, J.; Kwon, S. G.; Jang, Y.; Hyeon, T. Synthesis of Monodisperse Spherical Nanocrystals. *Angew. Chem. Int. Ed.* **2007**, *46*, 4630–4660.

(9) Reiss, P.; Carrière, M.; Lincheneau, C.; Vaure, L.; Tamang, S. Synthesis of Semiconductor Nanocrystals, Focusing on Nontoxic and Earth-Abundant Materials. *Chem. Rev.* **2016**, *116*, 10731–10819.

(10) Murray, C. B.; Norris, D. J.; Bawendi, M. G. Synthesis and Characterization of Nearly Monodisperse CdE (E = Sulfur, Selenium, Tellurium) Semiconductor Nanocrystallites. *J. Am. Chem. Soc.* **1993**, *115*, 8706–8715.

(11) Cushing, B. L.; Kolesnichenko, V. L.; O’Connor, C. J. Recent Advances in the Liquid-Phase Syntheses of Inorganic Nanoparticles. *Chem. Rev.* **2004**, *104*, 3893–3946.

(12) Niederberger, M. Nonaqueous Sol–Gel Routes to Metal Oxide Nanoparticles. *Acc. Chem. Res.* **2007**, *40*, 793–800.

(13) Kwon, S. G.; Hyeon, T. Formation Mechanisms of Uniform Nanocrystals via Hot-Injection and Heat-Up Methods. *Small* **2011**, *7*, 2685–2702.

(14) LaMer, V. K.; Dinegar, R. H. Theory, Production and Mechanism of Formation of Monodispersed Hydrosols. *J. Am. Chem. Soc.* **1950**, *72*, 4847–4854.

(15) Peng, X.; Wickham, J.; Alivisatos, A. P. Kinetics of II-VI and III-V Colloidal Semiconductor Nanocrystal Growth: “Focusing” of Size Distributions. *J. Am. Chem. Soc.* **1998**, *120*, 5343–5344.

(16) Park, J.; Lee, E.; Hwang, N.-M.; Kang, M.; Kim, S. C.; Hwang, Y.; Park, J.-G.; Noh, H.-J.; Kim, J.-Y.; Park, J.-H.; *et al.* One-Nanometer-Scale Size-Controlled Synthesis of Monodisperse Magnetic Iron Oxide Nanoparticles. *Angew. Chem. Int. Ed.* **2005**, *44*, 2872–2877.

(17) Yu, H.; Gibbons, P. C.; Kelton, K. F.; Buhro, W. E. Heterogeneous Seeded Growth: A Potentially General Synthesis of Monodisperse Metallic Nanoparticles. *J. Am. Chem. Soc.* **2001**, *123*, 9198–9199.

(18) Jana, N. R.; Peng, X. Single-Phase and Gram-Scale Routes toward Nearly Monodisperse Au and Other Noble Metal Nanocrystals. *J. Am. Chem. Soc.* **2003**, *125*, 14280–14281.

(19) Wilcoxon, J. P.; Provencio, P. P. Heterogeneous Growth of Metal Clusters from Solutions of Seed Nanoparticles. *J. Am. Chem. Soc.* **2004**, *126*, 6402–6408.

(20) Farrell, D.; Majetich, S. A.; Wilcoxon, J. P. Preparation and Characterization of Monodisperse Fe Nanoparticles. *J. Phys. Chem. B* **2003**, *107*, 11022–11030.

(21) Sun, S.; Zeng, H.; Robinson, D. B.; Raoux, S.; Rice, P. M.; Wang, S. X.; Li, G. Monodisperse MFe_2O_4 (M = Fe, Co, Mn) Nanoparticles. *J. Am. Chem. Soc.* **2004**, *126*, 273–279.

(22) Steigerwald, M. L.; Alivisatos, A. P.; Gibson, J. M.; Harris, T. D.; Kortan, R.; Muller, A. J.; Thayer, A. M.; Duncan, T. M.; Douglass, D. C.; Brus, L. E. Surface Derivatization and Isolation of Semiconductor Cluster Molecules. *J. Am. Chem. Soc.* **1988**, *110*, 3046–3050.

(23) Jana, N. R.; Gearheart, L.; Murphy, C. J. Evidence for Seed-Mediated Nucleation in the Chemical Reduction of Gold Salts to Gold Nanoparticles. *Chem. Mater.* **2001**, *13*, 2313–2322.

(24) Levy, M.; Quarta, A.; Espinosa, A.; Figuerola, A.; Wilhelm, C.; García-Hernández, M.; Genovese, A.; Falqui, A.; Alloyeau, D.; Buonsanti, R.; *et al.* Correlating Magneto-Structural Properties to Hyperthermia Performance of Highly Monodisperse Iron Oxide Nanoparticles Prepared by a Seeded-Growth Route. *Chem. Mater.* **2011**, *23*, 4170–4180.

(25) Vreeland, E. C.; Watt, J.; Schober, G. B.; Hance, B. G.; Austin, M. J.; Price, A. D.; Fellows, B. D.; Monson, T. C.; Hudak, N. S.; Maldonado-Camargo, L.; *et al.* Enhanced Nanoparticle Size Control by Extending LaMer's Mechanism. *Chem. Mater.* **2015**, *27*, 6059–6066.

(26) Gordon, T. R.; Cargnello, M.; Paik, T.; Mangolini, F.; Weber, R. T.; Fornasiero, P.; Murray, C. B. Nonaqueous Synthesis of TiO_2 Nanocrystals Using TiF_4 to Engineer Morphology, Oxygen Vacancy Concentration, and Photocatalytic Activity. *J. Am. Chem. Soc.* **2012**, *134*, 6751–6761.

(27) Buonsanti, R.; Grillo, V.; Carlino, E.; Giannini, C.; Kipp, T.; Cingolani, R.; Cozzoli, P. D. Nonhydrolytic Synthesis of High-Quality Anisotropically Shaped Brookite TiO_2 Nanocrystals. *J. Am. Chem. Soc.* **2008**, *130*, 11223–11233.

(28) Tamang, S.; Lee, S.; Choi, H.; Jeong, S. Tuning Size and Size Distribution of Colloidal InAs Nanocrystals via Continuous Supply of Prenucleation Clusters on Nanocrystal Seeds. *Chem. Mater.* **2016**, *28*, 8119–8122.

(29) Bronstein, L. M.; Huang, X.; Retrum, J.; Schmucker, A.; Pink, M.; Stein, B. D.; Dragnea, B. Influence of Iron Oleate Complex Structure on Iron Oxide Nanoparticle Formation. *Chem. Mater.* **2007**, *19*, 3624–3632.

(30) Ito, D.; Yokoyama, S.; Zaikova, T.; Masuko, K.; Hutchison, J. E. Synthesis of Ligand-Stabilized Metal Oxide Nanocrystals and Epitaxial Core/Shell Nanocrystals via a Lower-Temperature Esterification Process. *ACS Nano* **2014**, *8*, 64–75.

(31) Jansons, A. W.; Hutchison, J. E. Continuous Growth of Metal Oxide Nanocrystals: Enhanced Control of Nanocrystal Size and Radial Dopant Distribution. *ACS Nano* **2016**, *10*, 6942–6951.

(32) Buonsanti, R.; Milliron, D. J. Chemistry of Doped Colloidal Nanocrystals. *Chem. Mater.* **2013**, *25*, 1305–1317.

(33) Bryan, J. D.; Gamelin, D. R. Doped Semiconductor Nanocrystals: Synthesis, Characterization, Physical Properties, and Applications. In *Progress in Inorganic Chemistry*; John Wiley & Sons, Inc., 2005; pp. 47–126.

(34) Radovanovic, P. V. Defect-Induced Optical and Magnetic Properties of Colloidal Transparent Conducting Oxide Nanocrystals. In *Functional Metal Oxides*; Wiley-VCH Verlag GmbH & Co. KGaA, 2013; pp. 163–194.

(35) Norris, D. J.; Efros, A. L.; Erwin, S. C. Doped Nanocrystals. *Science* **2008**, *319*, 1776–1779.

(36) Deng, Z.; Tong, L.; Flores, M.; Lin, S.; Cheng, J.-X.; Yan, H.; Liu, Y. High-Quality Manganese-Doped Zinc Sulfide Quantum Rods with Tunable Dual-Color and Multiphoton Emissions. *J. Am. Chem. Soc.* **2011**, *133*, 5389–5396.

(37) Buonsanti, R.; Llordes, A.; Aloni, S.; Helms, B. A.; Milliron, D. J. Tunable Infrared Absorption and Visible Transparency of Colloidal Aluminum-Doped Zinc Oxide Nanocrystals. *Nano Lett.* **2011**, *11*, 4706–4710.

(38) Della Gaspera, E.; Chesman, A. S. R.; van Embden, J.; Jasieniak, J. J. Non-Injection Synthesis of Doped Zinc Oxide Plasmonic Nanocrystals. *ACS Nano* **2014**, *8*, 9154–9163.

(39) Djerdj, I.; Garnweitner, G.; Arcon, D.; Pregelj, M.; Jaglicic, Z.; Niederberger, M. Diluted Magnetic Semiconductors: Mn/Co-Doped ZnO Nanorods as Case Study. *J. Mater. Chem.* **2008**, *18*, 5208–5217.

(40) Bilecka, I.; Luo, L.; Djerdj, I.; Rossell, M. D.; Jagodič, M.; Jagličić, Z.; Masubuchi, Y.; Kikkawa, S.; Niederberger, M. Microwave-Assisted Nonaqueous Sol−Gel Chemistry for Highly Concentrated ZnO-Based Magnetic Semiconductor Nanocrystals. *J. Phys. Chem. C* **2011**, *115*, 1484–1495.

(41) Liang, X.; Ren, Y.; Bai, S.; Zhang, N.; Dai, X.; Wang, X.; He, H.; Jin, C.; Ye, Z.; Chen, Q.; *et al.* Colloidal Indium-Doped Zinc Oxide Nanocrystals with Tunable Work Function: Rational Synthesis and Optoelectronic Applications. *Chem. Mater.* **2014**, *26*, 5169–5178.

(42) Jansons, A. W.; Koskela, K. M.; Crockett, B. M.; Hutchison, J. E. Transition Metal-doped Metal Oxide Nanocrystals: Efficient Substitutional Doping Through a Continuous Growth Process. *Chem. Mater.* **2017**

(43) Singhal, A.; Achary, S. N.; Manjanna, J.; Jayakumar, O. D.; Kadam, R. M.; Tyagi, A. K. Colloidal Fe-Doped Indium Oxide Nanoparticles: Facile Synthesis, Structural, and Magnetic Properties. *J. Phys. Chem. C* **2009**, *113*, 3600–3606.

(44) Yang, P.; Lu, C.; Hua, N.; Du, Y. Titanium Dioxide Nanoparticles Co-Doped with Fe^{3+} and Eu^{3+} Ions for Photocatalysis. *Mater. Lett.* **2002**, *57*, 794–801.

(45) Ye, X.; Fei, J.; Diroll, B. T.; Paik, T.; Murray, C. B. Expanding the Spectral Tunability of Plasmonic Resonances in Doped Metal-Oxide Nanocrystals through Cooperative Cation–Anion Codoping. *J. Am. Chem. Soc.* **2014**, *136*, 11680–11686.

(46) Schwartz, D. A.; Norberg, N. S.; Nguyen, Q. P.; Parker, J. M.; Gamelin, D. R. Magnetic Quantum Dots: Synthesis, Spectroscopy, and Magnetism of Co^{2+}- and Ni^{2+}-Doped ZnO Nanocrystals. *J. Am. Chem. Soc.* **2003**, *125*, 13205–13218.

(47) Kovalenko, M. V.; Manna, L.; Cabot, A.; Hens, Z.; Talapin, D. V.; Kagan, C. R.; Klimov, V. I.; Rogach, A. L.; Reiss, P.; Milliron, D. J.; *et al.* Prospects of Nanoscience with Nanocrystals. *ACS Nano* **2015**, *9*, 1012–1057.

(48) Lounis, S. D.; Runnerstrom, E. L.; Llordés, A.; Milliron, D. J. Defect Chemistry and Plasmon Physics of Colloidal Metal Oxide Nanocrystals. *J. Phys. Chem. Lett.* **2014**, *5*, 1564–1574.

(49) Faucheaux, J. A.; Stanton, A. L. D.; Jain, P. K. Plasmon Resonances of Semiconductor Nanocrystals: Physical Principles and New Opportunities. *J. Phys. Chem. Lett.* **2014**, *5*, 976–985.

(50) Johns, R. W.; Bechtel, H. A.; Runnerstrom, E. L.; Agrawal, A.; Lounis, S. D.; Milliron, D. J. Direct Observation of Narrow Mid-Infrared Plasmon Linewidths of Single Metal Oxide Nanocrystals. *Nat Commun* **2016**, *7*.

(51) Luther, J. M.; Jain, P. K.; Ewers, T.; Alivisatos, A. P. Localized Surface Plasmon Resonances Arising from Free Carriers in Doped Quantum Dots. *Nat Mater* **2011**, *10*, 361–366.

(52) Kriegel, I.; Scotognella, F.; Manna, L. Plasmonic Doped Semiconductor Nanocrystals: Properties, Fabrication, Applications and Perspectives. *Plasmonic Doped Semicond. Nanocrystals Prop. Fabr. Appl. Perspect.* **2017**, *674*, 1–52.

(53) Agrawal, A.; Johns, R. W.; Milliron, D. J. Control of Localized Surface Plasmon Resonances in Metal Oxide Nanocrystals. *Annu. Rev. Mater. Res.* **2017**, *47*, null.

(54) Lounis, S. D.; Runnerstrom, E. L.; Bergerud, A.; Nordlund, D.; Milliron, D. J. Influence of Dopant Distribution on the Plasmonic Properties of Indium Tin Oxide Nanocrystals. *J. Am. Chem. Soc.* **2014**, *136*, 7110–7116.

(55) Kanehara, M.; Koike, H.; Yoshinaga, T.; Teranishi, T. Indium Tin Oxide Nanoparticles with Compositionally Tunable Surface Plasmon Resonance Frequencies in the Near-IR Region. *J. Am. Chem. Soc.* **2009**, *131*, 17736–17737.

(56) Choi, S.-I.; Nam, K. M.; Park, B. K.; Seo, W. S.; Park, J. T. Preparation and Optical Properties of Colloidal, Monodisperse, and Highly Crystalline ITO Nanoparticles. *Chem. Mater.* **2008**, *20*, 2609–2611.

(57) Crockett, B. M.; Jansons, A. W.; Koskela, K. M.; Johnson, D. W.; Hutchison, J. E. Core/Shell Dopant Segregation as a Strategy for Tuning Plasmonic Properties in Metal Oxide Nanocrystals. *ACS Nano*.

(58) Casavola, M.; Buonsanti, R.; Caputo, G.; Cozzoli, P. D. Colloidal Strategies for Preparing Oxide-Based Hybrid Nanocrystals. *Eur. J. Inorg. Chem.* **2008**, *2008*, 837–854.

(59) van Embden, J.; Jasieniak, J.; Gómez, D. E.; Mulvaney, P.; Giersig, M. Review of the Synthetic Chemistry Involved in the Production of Core/Shell Semiconductor Nanocrystals. *Aust. J. Chem.* **2007**, *60*, 457–471.

(60) Reiss, P.; Protière, M.; Li, L. Core/Shell Semiconductor Nanocrystals. *Small* **2009**, *5*, 154–168.

(61) Ghosh Chaudhuri, R.; Paria, S. Core/Shell Nanoparticles: Classes, Properties, Synthesis Mechanisms, Characterization, and Applications. *Chem. Rev.* **2012**, *112*, 2373–2433.

(62) Li, J. J.; Wang, Y. A.; Guo, W.; Keay, J. C.; Mishima, T. D.; Johnson, M. B.; Peng, X. Large-Scale Synthesis of Nearly Monodisperse CdSe/CdS Core/Shell Nanocrystals Using Air-Stable Reagents via Successive Ion Layer Adsorption and Reaction. *J. Am. Chem. Soc.* **2003**, *125*, 12567–12575.

(63) Xie, R.; Kolb, U.; Li, J.; Basché, T.; Mews, A. Synthesis and Characterization of Highly Luminescent CdSe−Core CdS/$Zn_{0.5}Cd_{0.5}S$/ZnS Multishell Nanocrystals. *J. Am. Chem. Soc.* **2005**, *127*, 7480–7488.

(64) Tan, R.; Blom, D. A.; Ma, S.; Greytak, A. B. Probing Surface Saturation Conditions in Alternating Layer Growth of CdSe/CdS Core/Shell Quantum Dots. *Chem. Mater.* **2013**, *25*, 3724–3736.

(65) Ocana, M.; Hsu, W. P.; Matijevic, E. Preparation and Properties of Uniform-Coated Colloidal Particles. 6. Titania on Zinc Oxide. *Langmuir* **1991**, *7*, 2911–2916.

(66) He, Q.; Zhang, Z.; Xiong, J.; Xiong, Y.; Xiao, H. A Novel Biomaterial — Fe_3O_4:TiO_2 Core-Shell Nano Particle with Magnetic Performance and High Visible Light Photocatalytic Activity. *Opt. Mater.* **2008**, *31*, 380–384.

(67) Davar, F.; Majedi, A.; Abbasi, A. Synthesis of Fe_3O_4@ZrO_2 Core–shell Nanoparticles through New Approach and Its Solar Light Photocatalyst Application. *J. Mater. Sci. Mater. Electron.* **2017**, *28*, 4871–4878.

Chapter III

(1) Park, J.; Joo, J.; Kwon, S. G.; Jang, Y.; Hyeon, T. Synthesis of Monodisperse Spherical Nanocrystals. *Angew. Chem. Int. Ed.* **2007**, *46*, 4630–4660.

(2) Thanh, N. T. K.; Maclean, N.; Mahiddine, S. Mechanisms of Nucleation and Growth of Nanoparticles in Solution. *Chem. Rev.* **2014**, *114*, 7610–7630.

(3) Kwon, S. G.; Hyeon, T. Formation Mechanisms of Uniform Nanocrystals *via* Hot-Injection and Heat-Up Methods. *Small* **2011**, *7*, 2685–2702.

(4) Owen, J. S.; Chan, E. M.; Liu, H.; Alivisatos, A. P. Precursor Conversion Kinetics and the Nucleation of Cadmium Selenide Nanocrystals. *J. Am. Chem. Soc.* **2010**, *132*, 18206–18213.

(5) Abe, S.; Čapek, R. K.; De Geyter, B.; Hens, Z. Tuning the Postfocused Size of Colloidal Nanocrystals by the Reaction Rate: From Theory to Application. *ACS Nano* **2012**, *6*, 42–53.

(6) Hendricks, M. P.; Cossairt, B. M.; Owen, J. S. The Importance of Nanocrystal Precursor Conversion Kinetics: Mechanism of the Reaction between Cadmium Carboxylate and Cadmium Bis(diphenyldithiophosphinate). *ACS Nano* **2012**, *6*, 10054–10062.

(7) Hendricks, M. P.; Campos, M. P.; Cleveland, G. T.; Jen-La Plante, I.; Owen, J. S. A Tunable Library of Substituted Thiourea Precursors to Metal Sulfide Nanocrystals. *Science* **2015**, *348*, 1226–1230.

(8) LaMer, V. K.; Dinegar, R. H. Theory, Production and Mechanism of Formation of Monodispersed Hydrosols. *J. Am. Chem. Soc.* **1950**, *72*, 4847–4854.

(9) Robb, D. T.; Privman, V. Model of Nanocrystal Formation in Solution by Burst Nucleation and Diffusional Growth. *Langmuir* **2008**, *24*, 26–35.

(10) Rempel, J. Y.; Bawendi, M. G.; Jensen, K. F. Insights into the Kinetics of Semiconductor Nanocrystal Nucleation and Growth. *J. Am. Chem. Soc.* **2009**, *131*, 4479–4489.

(11) Park, J.; Lee, E.; Hwang, N.-M.; Kang, M.; Kim, S. C.; Hwang, Y.; Park, J.-G.; Noh, H.-J.; Kim, J.-Y.; Park, J.-H.; Hyeon, T. One-Nanometer-Scale Size-Controlled Synthesis of Monodisperse Magnetic Iron Oxide Nanoparticles. *Angew. Chem. Int. Ed.* **2005**, *44*, 2872–2877.

(12) Yu, H.; Gibbons, P. C.; Kelton, K. F.; Buhro, W. E. Heterogeneous Seeded Growth: A Potentially General Synthesis of Monodisperse Metallic Nanoparticles. *J. Am. Chem. Soc.* **2001**, *123*, 9198–9199.

(13) Jana, N. R.; Peng, X. Single-Phase and Gram-Scale Routes toward Nearly Monodisperse Au and Other Noble Metal Nanocrystals. *J. Am. Chem. Soc.* **2003**, *125*, 14280–14281.

(14) Wilcoxon, J. P.; Provencio, P. P. Heterogeneous Growth of Metal Clusters from Solutions of Seed Nanoparticles. *J. Am. Chem. Soc.* **2004**, *126*, 6402–6408.

(15) Farrell, D.; Majetich, S. A.; Wilcoxon, J. P. Preparation and Characterization of Monodisperse Fe Nanoparticles. *J. Phys. Chem. B* **2003**, *107*, 11022–11030.

(16) Sun, S.; Zeng, H.; Robinson, D. B.; Raoux, S.; Rice, P. M.; Wang, S. X.; Li, G. Monodisperse MFe_2O_4 (M = Fe, Co, Mn) Nanoparticles. *J. Am. Chem. Soc.* **2004**, *126*, 273–279.

(17) Peng, X.; Wickham, J.; Alivisatos, A. P. Kinetics of II-VI and III-V Colloidal Semiconductor Nanocrystal Growth: "Focusing" of Size Distributions. *J. Am. Chem. Soc.* **1998**, *120*, 5343–5344.

(18) Qian, C.; Kim, F.; Ma, L.; Tsui, F.; Yang, P.; Liu, J. Solution-Phase Synthesis of Single-Crystalline Iron Phosphide Nanorods/Nanowires. *J. Am. Chem. Soc.* **2004**, *126*, 1195–1198.

(19) Lu, W.; Gao, P.; Jian, W. B.; Wang, Z. L.; Fang, J. Perfect Orientation Ordered in-Situ One-Dimensional Self-Assembly of Mn-Doped PbSe Nanocrystals. *J. Am. Chem. Soc.* **2004**, *126*, 14816–14821.

(20) Watzky, M. A.; Finke, R. G. Nanocluster Size-Control and "Magic Number" Investigations. Experimental Tests of the "Living-Metal Polymer" Concept and of Mechanism-Based Size-Control Predictions Leading to the Syntheses of Iridium(0) Nanoclusters Centering about Four Sequential Magic Numbers. *Chem. Mater.* **1997**, *9*, 3083–3095.

(21) Wang, X.; Zhuang, J.; Peng, Q.; Li, Y. A General Strategy for Nanocrystal Synthesis. *Nature* **2005**, *437*, 121–124.

(22) Mayer, M.; Scarabelli, L.; March, K.; Altantzis, T.; Tebbe, M.; Kociak, M.; Bals, S.; García de Abajo, F. J.; Fery, A.; Liz-Marzán, L. M. Controlled Living Nanowire Growth: Precise Control over the Morphology and Optical Properties of AgAuAg Bimetallic Nanowires. *Nano Lett.* **2015**, *15*, 5427–5437.

(23) Cademartiri, L.; Guerin, G.; Bishop, K. J. M.; Winnik, M. A.; Ozin, G. A. Polymer-like Conformation and Growth Kinetics of Bi_2S_3 Nanowires. *J. Am. Chem. Soc.* **2012**, *134*, 9327–9334.

(24) Evans, C. M.; Love, A. M.; Weiss, E. A. Surfactant-Controlled Polymerization of Semiconductor Clusters to Quantum Dots through Competing Step-Growth and Living Chain-Growth Mechanisms. *J. Am. Chem. Soc.* **2012**, *134*, 17298–17305.

(25) Gordon, T. R.; Cargnello, M.; Paik, T.; Mangolini, F.; Weber, R. T.; Fornasiero, P.; Murray, C. B. Nonaqueous Synthesis of TiO_2 Nanocrystals Using TiF_4 to Engineer Morphology, Oxygen Vacancy Concentration, and Photocatalytic Activity. *J. Am. Chem. Soc.* **2012**, *134*, 6751–6761.

(26) Vreeland, E. C.; Watt, J.; Schober, G. B.; Hance, B. G.; Austin, M. J.; Price, A. D.; Fellows, B. D.; Monson, T. C.; Hudak, N. S.; Maldonado-Camargo, L.; Bohorquez, A. C.; Rinaldi, C.; Huber, D. L. Enhanced Nanoparticle Size Control by Extending LaMer's Mechanism. *Chem. Mater.* **2015**, *27*, 6059–6066.

(27) Buonsanti, R.; Grillo, V.; Carlino, E.; Giannini, C.; Kipp, T.; Cingolani, R.; Cozzoli, P. D. Nonhydrolytic Synthesis of High-Quality Anisotropically Shaped Brookite TiO_2 Nanocrystals. *J. Am. Chem. Soc.* **2008**, *130*, 11223–11233.

(28) Ito, D.; Yokoyama, S.; Zaikova, T.; Masuko, K.; Hutchison, J. E. Synthesis of Ligand-Stabilized Metal Oxide Nanocrystals and Epitaxial Core/Shell Nanocrystals *via* a Lower-Temperature Esterification Process. *ACS Nano* **2014**, *8*, 64–75.

(29) Niederberger, M. Nonaqueous Sol–Gel Routes to Metal Oxide Nanoparticles. *Acc. Chem. Res.* **2007**, *40*, 793–800.

(30) Song, J.; Kulinich, S. A.; Li, J.; Liu, Y.; Zeng, H. A General One-Pot Strategy for the Synthesis of High-Performance Transparent-Conducting-Oxide Nanocrystal Inks for All-Solution-Processed Devices. *Angew. Chem. Int. Ed.* **2015**, *54*, 462–466.

(31) Della Gaspera, E.; Chesman, A. S. R.; van Embden, J.; Jasieniak, J. J. Non-Injection Synthesis of Doped Zinc Oxide Plasmonic Nanocrystals. *ACS Nano* **2014**, *8*, 9154–9163.

(32) Narayanaswamy, A.; Xu, H.; Pradhan, N.; Kim, M.; Peng, X. Formation of Nearly Monodisperse In_2O_3 Nanodots and Oriented-Attached Nanoflowers: Hydrolysis and Alcoholysis vs Pyrolysis. *J. Am. Chem. Soc.* **2006**, *128*, 10310–10319.

(33) Ilavsky, J.; Jemian, P. R. Irena: Tool Suite for Modeling and Analysis of Small-Angle Scattering. *J. Appl. Crystallogr.* **2009**, *42*, 347–353.

(34) Szwarc, M. Living Polymers. Their Discovery, Characterization, and Properties. *J. Polym. Sci. Part Polym. Chem.* **1998**, *36*, IX – XV.

(35) Xia, Y.; Xiong, Y.; Lim, B.; Skrabalak, S. E. Shape-Controlled Synthesis of Metal Nanocrystals: Simple Chemistry Meets Complex Physics? *Angew. Chem. Int. Ed.* **2009**, *48*, 60–103.

(36) Agoston, P.; Albe, K. Thermodynamic Stability, Stoichiometry, and Electronic Structure of bcc-In_2O_3 Surfaces. *Phys. Rev. B* **2011**, *84*, 045311.

(37) Reiss, P.; Protière, M.; Li, L. Core/Shell Semiconductor Nanocrystals. *Small* **2009**, *5*, 154–168.

(38) Ghosh Chaudhuri, R.; Paria, S. Core/Shell Nanoparticles: Classes, Properties, Synthesis Mechanisms, Characterization, and Applications. *Chem. Rev.* **2012**, *112*, 2373–2433.

(39) Buonsanti, R.; Milliron, D. J. Chemistry of Doped Colloidal Nanocrystals. *Chem. Mater.* **2013**, *25*, 1305–1317.

(40) Tanuma, S.; Powell, C. J.; Penn, D. R. Calculations of Electron Inelastic Mean Free Paths. V. Data for 14 Organic Compounds over the 50–2000 eV Range. *Surf. Interface Anal.* **1994**, *21*, 165–176.

(41) Tougaard, S. Surface Nanostructure Determination by X-ray Photoemission Spectroscopy Peak Shape Analysis. *J. Vac. Sci. Technol. A* **1996**, *14*, 1415–1423.

(42) Kovalenko, M. V.; Manna, L.; Cabot, A.; Hens, Z.; Talapin, D. V.; Kagan, C. R.; Klimov, V. I.; Rogach, A. L.; Reiss, P.; Milliron, D. J.; Guyot-Sionnnest, P.; Konstantatos, G.; Parak, W. J.; Hyeon, T.; Korgel, B. A.; Murray, C. B.; Heiss, W. Prospects of Nanoscience with Nanocrystals. *ACS Nano* **2015**, *9*, 1012–1057.

(43) Faucheaux, J. A.; Stanton, A. L. D.; Jain, P. K. Plasmon Resonances of Semiconductor Nanocrystals: Physical Principles and New Opportunities. *J. Phys. Chem. Lett.* **2014**, *5*, 976–985.

(44) Lounis, S. D.; Runnerstrom, E. L.; Llordés, A.; Milliron, D. J. Defect Chemistry and Plasmon Physics of Colloidal Metal Oxide Nanocrystals. *J. Phys. Chem. Lett.* **2014**, *5*, 1564–1574.

(45) Schimpf, A. M.; Lounis, S. D.; Runnerstrom, E. L.; Milliron, D. J.; Gamelin, D. R. Redox Chemistries and Plasmon Energies of Photodoped In_2O_3 and Sn-Doped In_2O_3 (ITO) Nanocrystals. *J. Am. Chem. Soc.* **2015**, *137*, 518–524.

(46) Lounis, S. D.; Runnerstrom, E. L.; Bergerud, A.; Nordlund, D.; Milliron, D. J. Influence of Dopant Distribution on the Plasmonic Properties of Indium Tin Oxide Nanocrystals. *J. Am. Chem. Soc.* **2014**, *136*, 7110–7116.

(47) Kline, S. Reduction and Analysis of SANS and USANS Data Using IGOR Pro. *J. Appl. Crystallogr.* **2006**, *39*, 895–900.

(48) Woehrle, G. H.; Hutchison, J. E.; Özkar, S.; Finke, R. G. Analysis of Nanoparticle Transmission Electron Microscopy Data Using a Public-Domain Image-Processing Program, Image. *Turk. J. Chem.* **2006**, *30*, 1–13.

Chapter IV

(1) Levy, R. *Microelectronic Materials and Processes*; Springer Science & Business Media, 2012; Vol. 164.

(2) Ohno, H. Making Nonmagnetic Semiconductors Ferromagnetic. *Science* **1998**, *281*, 951–956.

(3) Talapin, D. V.; Lee, J.-S.; Kovalenko, M. V.; Shevchenko, E. V. Prospects of Colloidal Nanocrystals for Electronic and Optoelectronic Applications. *Chem. Rev.* **2010**, *110*, 389–458.

(4) Kovalenko, M. V.; Manna, L.; Cabot, A.; Hens, Z.; Talapin, D. V.; Kagan, C. R.; Klimov, V. I.; Rogach, A. L.; Reiss, P.; Milliron, D. J.; *et al.* Prospects of Nanoscience with Nanocrystals. *ACS Nano* **2015**, *9*, 1012–1057.

(5) Liang, X.; Bai, S.; Wang, X.; Dai, X.; Gao, F.; Sun, B.; Ning, Z.; Ye, Z.; Jin, Y. Colloidal Metal Oxide Nanocrystals as Charge Transporting Layers for Solution-Processed Light-Emitting Diodes and Solar Cells. *Chem. Soc. Rev.* **2017**.

(6) Saleh, N. B.; Milliron, D. J.; Aich, N.; Katz, L. E.; Liljestrand, H. M.; Kirisits, M. J. Importance of Doping, Dopant Distribution, and Defects on Electronic Band Structure Alteration of Metal Oxide Nanoparticles: Implications for Reactive Oxygen Species. *Sci. Total Environ.* **2016**, *568*, 926–932.

(7) Furdyna, J. K. Diluted Magnetic Semiconductors. *J. Appl. Phys.* **1988**, *64*, R29–R64.

(8) Ochsenbein, S. T.; Gamelin, D. R. Quantum Oscillations in Magnetically Doped Colloidal Nanocrystals. *Nat Nano* **2011**, *6*, 112–115.

(9) Ochsenbein, S. T.; Feng, Y.; Whitaker, K. M.; Badaeva, E.; Liu, W. K.; Li, X.; Gamelin, D. R. Charge-Controlled Magnetism in Colloidal Doped Semiconductor Nanocrystals. *Nat Nano* **2009**, *4*, 681–687.

(10) Liu, W. K.; Whitaker, K. M.; Kittilstved, K. R.; Gamelin, D. R. Stable Photogenerated Carriers in Magnetic Semiconductor Nanocrystals. *J. Am. Chem. Soc.* **2006**, *128*, 3910–3911.

(11) Stowell, C. A.; Wiacek, R. J.; Saunders, A. E.; Korgel, B. A. Synthesis and Characterization of Dilute Magnetic Semiconductor Manganese-Doped Indium Arsenide Nanocrystals. *Nano Lett.* **2003**, *3*, 1441–1447.

(12) Somaskandan, K.; Tsoi, G. M.; Wenger, L. E.; Brock, S. L. Isovalent Doping Strategy for Manganese Introduction into III-V Diluted Magnetic Semiconductor Nanoparticles: InP:Mn. *Chem. Mater.* **2005**, *17*, 1190–1198.

(13) Lin, J.; Hu, D.-D.; Zhang, Q.; Li, D.-S.; Wu, T.; Bu, X.; Feng, P. Improving Photoluminescence Emission Efficiency of Nanocluster-Based Materials by in Situ Doping Synthetic Strategy. *J. Phys. Chem. C* **2016**, *120*, 29390–29396.

(14) Mocatta, D.; Cohen, G.; Schattner, J.; Millo, O.; Rabani, E.; Banin, U. Heavily Doped Semiconductor Nanocrystal Quantum Dots. *Science* **2011**, *332*, 77–81.

(15) Pradhan, N.; Goorskey, D.; Thessing, J.; Peng, X. An Alternative of CdSe Nanocrystal Emitters: Pure and Tunable Impurity Emissions in ZnSe Nanocrystals. *J. Am. Chem. Soc.* **2005**, *127*, 17586–17587.

(16) Pu, C.; Qin, H.; Gao, Y.; Zhou, J.; Wang, P.; Peng, X. Synthetic Control of Exciton Behavior in Colloidal Quantum Dots. *J. Am. Chem. Soc.* **2017**, *139*, 3302–3311.

(17) Deng, Z.; Tong, L.; Flores, M.; Lin, S.; Cheng, J.-X.; Yan, H.; Liu, Y. High-Quality Manganese-Doped Zinc Sulfide Quantum Rods with Tunable Dual-Color and Multiphoton Emissions. *J. Am. Chem. Soc.* **2011**, *133*, 5389–5396.

(18) Wu, S.; Han, G.; Milliron, D. J.; Aloni, S.; Altoe, V.; Talapin, D. V.; Cohen, B. E.; Schuck, P. J. Non-Blinking and Photostable Upconverted Luminescence from Single Lanthanide-Doped Nanocrystals. *Proc. Natl. Acad. Sci.* **2009**, *106*, 10917–10921.

(19) Ostrowski, A. D.; Chan, E. M.; Gargas, D. J.; Katz, E. M.; Han, G.; Schuck, P. J.; Milliron, D. J.; Cohen, B. E. Controlled Synthesis and Single-Particle Imaging of Bright, Sub-10 Nm Lanthanide-Doped Upconverting Nanocrystals. *ACS Nano* **2012**, *6*, 2686–2692.

(20) Bradshaw, L. R.; Knowles, K. E.; McDowall, S.; Gamelin, D. R. Nanocrystals for Luminescent Solar Concentrators. *Nano Lett.* **2015**, *15*, 1315–1323.

(21) Knowles, K. E.; Hartstein, K. H.; Kilburn, T. B.; Marchioro, A.; Nelson, H. D.; Whitham, P. J.; Gamelin, D. R. Luminescent Colloidal Semiconductor Nanocrystals

Containing Copper: Synthesis, Photophysics, and Applications. *Chem. Rev.* **2016**, *116*, 10820–10851.

(22) Walter, M. G.; Warren, E. L.; McKone, J. R.; Boettcher, S. W.; Mi, Q.; Santori, E. A.; Lewis, N. S. Solar Water Splitting Cells. *Chem. Rev.* **2010**, *110*, 6446–6473.

(23) Cong, Y.; Zhang, J.; Chen, F.; Anpo, M.; He, D. Preparation, Photocatalytic Activity, and Mechanism of Nano-TiO_2 Co-Doped with Nitrogen and Iron (III). *J. Phys. Chem. C* **2007**, *111*, 10618–10623.

(24) Xu, A.-W.; Gao, Y.; Liu, H.-Q. The Preparation, Characterization, and Their Photocatalytic Activities of Rare-Earth-Doped TiO_2 Nanoparticles. *J. Catal.* **2002**, *207*, 151–157.

(25) Kriegel, I.; Scotognella, F.; Manna, L. Plasmonic Doped Semiconductor Nanocrystals: Properties, Fabrication, Applications and Perspectives. *Plasmonic Doped Semicond. Nanocrystals Prop. Fabr. Appl. Perspect.* **2017**, *674*, 1–52.

(26) Comin, A.; Manna, L. New Materials for Tunable Plasmonic Colloidal Nanocrystals. *Chem. Soc. Rev.* **2014**, *43*, 3957–3975.

(27) Della Gaspera, E.; Chesman, A. S. R.; van Embden, J.; Jasieniak, J. J. Non-Injection Synthesis of Doped Zinc Oxide Plasmonic Nanocrystals. *ACS Nano* **2014**, *8*, 9154–9163.

(28) Lounis, S. D.; Runnerstrom, E. L.; Llordés, A.; Milliron, D. J. Defect Chemistry and Plasmon Physics of Colloidal Metal Oxide Nanocrystals. *J. Phys. Chem. Lett.* **2014**, *5*, 1564–1574.

(29) Runnerstrom, E. L.; Bergerud, A.; Agrawal, A.; Johns, R. W.; Dahlman, C. J.; Singh, A.; Selbach, S. M.; Milliron, D. J. Defect Engineering in Plasmonic Metal Oxide Nanocrystals. *Nano Lett.* **2016**, *16*, 3390–3398.

(30) Schimpf, A. M.; Lounis, S. D.; Runnerstrom, E. L.; Milliron, D. J.; Gamelin, D. R. Redox Chemistries and Plasmon Energies of Photodoped In_2O_3 and Sn-Doped In_2O_3 (ITO) Nanocrystals. *J. Am. Chem. Soc.* **2015**, *137*, 518–524.

(31) Agrawal, A.; Johns, R. W.; Milliron, D. J. Control of Localized Surface Plasmon Resonances in Metal Oxide Nanocrystals. *Annu. Rev. Mater. Res.* **2017**, *47*, 1-31.

(32) Johns, R. W.; Bechtel, H. A.; Runnerstrom, E. L.; Agrawal, A.; Lounis, S. D.; Milliron, D. J. Direct Observation of Narrow Mid-Infrared Plasmon Linewidths of Single Metal Oxide Nanocrystals. *Nat. Commun.* **2016**, *7*, 11583.

(33) Schimpf, A. M.; Knowles, K. E.; Carroll, G. M.; Gamelin, D. R. Electronic Doping and Redox-Potential Tuning in Colloidal Semiconductor Nanocrystals. *Acc. Chem. Res.* **2015**, *48*, 1929–1937.

(34) Radovanovic, P. V.; Norberg, N. S.; McNally, K. E.; Gamelin, D. R. Colloidal Transition-Metal-Doped ZnO Quantum Dots. *J. Am. Chem. Soc.* **2002**, *124*, 15192–15193.

(35) Djerdj, I.; Garnweitner, G.; Arcon, D.; Pregelj, M.; Jaglicic, Z.; Niederberger, M. Diluted Magnetic Semiconductors: Mn/Co-Doped ZnO Nanorods as Case Study. *J. Mater. Chem.* **2008**, *18*, 5208–5217.

(36) Djerdj, I.; Arčon, D.; Jagličić, Z.; Niederberger, M. Nonaqueous Synthesis of Metal Oxide Nanoparticles: Short Review and Doped Titanium Dioxide as Case Study for the Preparation of Transition Metal-Doped Oxide Nanoparticles. *Solid State Chem. Nanoscale Achiev. Chall. Oppor.* **2008**, *181*, 1571–1581.

(37) Bilecka, I.; Luo, L.; Djerdj, I.; Rossell, M. D.; Jagodič, M.; Jagličić, Z.; Masubuchi, Y.; Kikkawa, S.; Niederberger, M. Microwave-Assisted Nonaqueous Sol−Gel Chemistry for Highly Concentrated ZnO-Based Magnetic Semiconductor Nanocrystals. *J. Phys. Chem. C* **2011**, *115*, 1484–1495.

(38) Viswanatha, R.; Sapra, S.; Sen Gupta, S.; Satpati, B.; Satyam, P. V.; Dev, B. N.; Sarma, D. D. Synthesis and Characterization of Mn-Doped ZnO Nanocrystals. *J. Phys. Chem. B* **2004**, *108*, 6303–6310.

(39) Farvid, S. S.; Ju, L.; Worden, M.; Radovanovic, P. V. Colloidal Chromium-Doped In_2O_3 Nanocrystals as Building Blocks for High-TC Ferromagnetic Transparent Conducting Oxide Structures. *J. Phys. Chem. C* **2008**, *112*, 17755–17759.

(40) Liang, X.; Ren, Y.; Bai, S.; Zhang, N.; Dai, X.; Wang, X.; He, H.; Jin, C.; Ye, Z.; Chen, Q.; *et al.* Colloidal Indium-Doped Zinc Oxide Nanocrystals with Tunable Work Function: Rational Synthesis and Optoelectronic Applications. *Chem. Mater.* **2014**, *26*, 5169–5178.

(41) Buonsanti, R.; Llordes, A.; Aloni, S.; Helms, B. A.; Milliron, D. J. Tunable Infrared Absorption and Visible Transparency of Colloidal Aluminum-Doped Zinc Oxide Nanocrystals. *Nano Lett.* **2011**, *11*, 4706–4710.

(42) Gilstrap, R. A.; Capozzi, C. J.; Carson, C. G.; Gerhardt, R. A.; Summers, C. J. Synthesis of a Nonagglomerated Indium Tin Oxide Nanoparticle Dispersion. *Adv. Mater.* **2008**, *20*, 4163–4166.

(43) Choi, S.-I.; Nam, K. M.; Park, B. K.; Seo, W. S.; Park, J. T. Preparation and Optical Properties of Colloidal, Monodisperse, and Highly Crystalline ITO Nanoparticles. *Chem. Mater.* **2008**, *20*, 2609–2611.

(44) Sun, Z.; He, J.; Kumbhar, A.; Fang, J. Nonaqueous Synthesis and Photoluminescence of ITO Nanoparticles. *Langmuir* **2010**, *26*, 4246–4250.

(45) Della Gaspera, E.; Bersani, M.; Cittadini, M.; Guglielmi, M.; Pagani, D.; Noriega, R.; Mehra, S.; Salleo, A.; Martucci, A. Low-Temperature Processed Ga-Doped ZnO Coatings from Colloidal Inks. *J. Am. Chem. Soc.* **2013**, *135*, 3439–3448.

(46) Norris, D. J.; Efros, A. L.; Erwin, S. C. Doped Nanocrystals. *Science* **2008**, *319*, 1776–1779.

(47) Dalpian, G. M.; Chelikowsky, J. R. Self-Purification in Semiconductor Nanocrystals. *Phys. Rev. Lett.* **2006**, *96*, 226802.

(48) Erwin, S. C.; Zu, L.; Haftel, M. I.; Efros, A. L.; Kennedy, T. A.; Norris, D. J. Doping Semiconductor Nanocrystals. *Nature* **2005**, *436*, 91–94.

(49) Galli, G. Solid-State Physics: Doping the Undopable. *Nature* **2005**, *436*, 32–33.

(50) Buonsanti, R.; Milliron, D. J. Chemistry of Doped Colloidal Nanocrystals. *Chem. Mater.* **2013**, *25*, 1305–1317.

(51) Du, M.-H.; Erwin, S. C.; Efros, A. L. Trapped-Dopant Model of Doping in Semiconductor Nanocrystals. *Nano Lett.* **2008**, *8*, 2878–2882.

(52) Lounis, S. D.; Runnerstrom, E. L.; Bergerud, A.; Nordlund, D.; Milliron, D. J. Influence of Dopant Distribution on the Plasmonic Properties of Indium Tin Oxide Nanocrystals. *J. Am. Chem. Soc.* **2014**, *136*, 7110–7116.

(53) Crockett, B. M.; Jansons, A. W.; Koskela, K. M.; Johnson, D. W.; Hutchison, J. E. Radial Dopant Placement for Tuning Plasmonic Properties in Metal Oxide Nanocrystals. *ACS Nano* **2017**, 11, 7719-7728.

(54) Bryan, J. D.; Gamelin, D. R. Doped Semiconductor Nanocrystals: Synthesis, Characterization, Physical Properties, and Applications. In *Progress in Inorganic Chemistry*; John Wiley & Sons, Inc., 2005; pp. 47–126.

(55) Zhang, N.; Wang, X.; Ye, Z.; Jin, Y. A Quantitative Study of Chemical Kinetics for the Synthesis of Doped Oxide Nanocrystals Using FTIR. *Sci. Rep.* **2014**, *4*, 4353.

(56) Jansons, A. W.; Hutchison, J. E. Continuous Growth of Metal Oxide Nanocrystals: Enhanced Control of Nanocrystal Size and Radial Dopant Distribution. *ACS Nano* **2016**, *10*, 6942–6951.

(57) Jansons, A. W.; Plummer, L. K.; Hutchison, J. E. Living Nanocrystals. *Chem. Mater.* **2017**, *29*, 5415–5425.

(58) Song, J.; Kulinich, S. A.; Li, J.; Liu, Y.; Zeng, H. A General One-Pot Strategy for the Synthesis of High-Performance Transparent-Conducting-Oxide Nanocrystal Inks for All-Solution-Processed Devices. *Angew. Chem. Int. Ed.* **2015**, *54*, 462–466.

(59) Ito, D.; Yokoyama, S.; Zaikova, T.; Masuko, K.; Hutchison, J. E. Synthesis of Ligand-Stabilized Metal Oxide Nanocrystals and Epitaxial Core/Shell Nanocrystals via a Lower-Temperature Esterification Process. *ACS Nano* **2014**, *8*, 64–75.

(60) Niederberger, M. Nonaqueous Sol–Gel Routes to Metal Oxide Nanoparticles. *Acc. Chem. Res.* **2007**, *40*, 793–800.

(61) Frank, G.; Köstlin, H. Electrical Properties and Defect Model of Tin-Doped Indium Oxide Layers. *Appl. Phys. A* **1982**, *27*, 197–206.

(62) Kanehara, M.; Koike, H.; Yoshinaga, T.; Teranishi, T. Indium Tin Oxide Nanoparticles with Compositionally Tunable Surface Plasmon Resonance Frequencies in the Near-IR Region. *J. Am. Chem. Soc.* **2009**, *131*, 17736–17737.

(63) Radovanovic, P. V. Defect-Induced Optical and Magnetic Properties of Colloidal Transparent Conducting Oxide Nanocrystals. In *Functional Metal Oxides*; Wiley-VCH Verlag GmbH & Co. KGaA, 2013; pp. 163–194.

(64) Shannon, R. Revised Effective Ionic Radii and Systematic Studies of Interatomic Distances in Halides and Chalcogenides. *Acta Crystallogr. Sect. A* **1976**, *32*, 751–767.

(65) Schwartz, D. A.; Norberg, N. S.; Nguyen, Q. P.; Parker, J. M.; Gamelin, D. R. Magnetic Quantum Dots: Synthesis, Spectroscopy, and Magnetism of Co^{2+}- and Ni^{2+}-Doped ZnO Nanocrystals. *J. Am. Chem. Soc.* **2003**, *125*, 13205–13218.

(66) van Enckevort, W. J. P.; van der Berg, A. C. J. F.; Kreuwel, K. B. G.; Derksen, A. J.; Couto, M. S. Impurity Blocking of Growth Steps: Experiments and Theory. *Cryst. Growth 1995* **1996**, *166*, 156–161.

(67) Yang, Y.; Jin, Y.; He, H.; Wang, Q.; Tu, Y.; Lu, H.; Ye, Z. Dopant-Induced Shape Evolution of Colloidal Nanocrystals: The Case of Zinc Oxide. *J. Am. Chem. Soc.* **2010**, *132*, 13381–13394.

(68) Tanuma, S.; Powell, C. J.; Penn, D. R. Calculations of Electron Inelastic Mean Free Paths. V. Data for 14 Organic Compounds over the 50–2000 eV Range. *Surf. Interface Anal.* **1994**, *21*, 165–176.

(69) Farvid, S. S.; Dave, N.; Wang, T.; Radovanovic, P. V. Dopant-Induced Manipulation of the Growth and Structural Metastability of Colloidal Indium Oxide Nanocrystals. *J. Phys. Chem. C* **2009**, *113*, 15928–15933.

(70) Farvid, S. S.; Sabergharesou, T.; Hutfluss, L. N.; Hegde, M.; Prouzet, E.; Radovanovic, P. V. Evidence of Charge-Transfer Ferromagnetism in Transparent Diluted Magnetic Oxide Nanocrystals: Switching the Mechanism of Magnetic Interactions. *J. Am. Chem. Soc.* **2014**, *136*, 7669–7679.

(71) Roisnel, T.; Rodríquez-Carvajal, J. WinPLOTR: A Windows Tool for Powder Diffraction Pattern Analysis. In *Materials Science Forum*; Transtec Publications; 1999, 2001; Vol. 378, pp. 118–123.

(72) Denton, A. R.; Ashcroft, N. W. Vegard's Law. *Phys. Rev. A* **1991**, *43*, 3161–3164.

(73) Perebeinos, V.; Chan, S.-W.; Zhang, F. "Madelung Model" Prediction for Dependence of Lattice Parameter on Nanocrystal Size. *Solid State Commun.* **2002**, *123*, 295–297.

(74) González, G. B.; Cohen, J. B.; Hwang, J.-H.; Mason, T. O.; Hodges, J. P.; Jorgensen, J. D. Neutron Diffraction Study on the Defect Structure of Indium–tin–oxide. *J. Appl. Phys.* **2001**, *89*, 2550–2555.

(75) Stanek, C. R.; McClellan, K. J.; Uberuaga, B. P.; Sickafus, K. E.; Levy, M. R.; Grimes, R. W. Determining the Site Preference of Trivalent Dopants in Bixbyite Sesquioxides by Atomic-Scale Simulations. *Phys. Rev. B* **2007**, *75*, 134101.

(76) Lever, A. B. P. *Inorganic Electronic Spectroscopy*; Elsevier: New York: Amsterdam ; New York, 1984.

(77) Garnet, N. S.; Ghodsi, V.; Hutfluss, L. N.; Yin, P.; Hegde, M.; Radovanovic, P. V. Probing the Role of Dopant Oxidation State in the Magnetism of Diluted Magnetic Oxides Using Fe-Doped In_2O_3 and SnO_2 Nanocrystals. *J. Phys. Chem. C* **2017**, *121*, 1918–1927.

(78) Singhal, A.; Achary, S. N.; Manjanna, J.; Jayakumar, O. D.; Kadam, R. M.; Tyagi, A. K. Colloidal Fe-Doped Indium Oxide Nanoparticles: Facile Synthesis, Structural, and Magnetic Properties. *J. Phys. Chem. C* **2009**, *113*, 3600–3606.

(79) Hakimi, A. M. H. R.; Blamire, M. G.; Heald, S. M.; Alshammari, M. S.; Alqahtani, M. S.; Score, D. S.; Blythe, H. J.; Fox, A. M.; Gehring, G. A. Donor-Band Ferromagnetism in Cobalt-Doped Indium Oxide. *Phys. Rev. B* **2011**, *84*, 085201.

(80) Liu, D.; Lei, W. W.; Zou, B.; Yu, S. D.; Hao, J.; Wang, K.; Liu, B. B.; Cui, Q. L.; Zou, G. T. High-Pressure X-Ray Diffraction and Raman Spectra Study of Indium Oxide. *J. Appl. Phys.* **2008**, *104*, 083506.

(81) Tang, L.-M.; Wang, L.-L.; Wang, D.; Liu, J.-Z.; Chen, K.-Q. Donor-Donor Binding in In_2O_3: Engineering Shallow Donor Levels. *J. Appl. Phys.* **2010**, *107*, 083704.

(82) Faucheaux, J. A.; Stanton, A. L. D.; Jain, P. K. Plasmon Resonances of Semiconductor Nanocrystals: Physical Principles and New Opportunities. *J. Phys. Chem. Lett.* **2014**, *5*, 976–985.

(83) Liu, X.; Swihart, M. T. Heavily-Doped Colloidal Semiconductor and Metal Oxide Nanocrystals: An Emerging New Class of Plasmonic Nanomaterials. *Chem. Soc. Rev.* **2014**, *43*, 3908–3920.

(84) Luther, J. M.; Jain, P. K.; Ewers, T.; Alivisatos, A. P. Localized Surface Plasmon Resonances Arising from Free Carriers in Doped Quantum Dots. *Nat Mater* **2011**, *10*, 361–366.

(85) Korotcenkov, G.; Boris, I.; Brinzari, V.; Golovanov, V.; Lychkovsky, Y.; Karkotsky, G.; Cornet, A.; Rossinyol, E.; Rodrigue, J.; Cirera, A. Gas-Sensing Characteristics of One-Electrode Gas Sensors Based on Doped In_2O_3 Ceramics. *17th Euopean Conf. Solid-State Transducers Univ. Minho Guimares Port. Sept. 21-24 2003* **2004**, *103*, 13–22.

(86) Elouali, S.; Bloor, L. G.; Binions, R.; Parkin, I. P.; Carmalt, C. J.; Darr, J. A. Gas Sensing with Nano-Indium Oxides (In_2O_3) Prepared via Continuous Hydrothermal Flow Synthesis. *Langmuir* **2012**, *28*, 1879–1885.

(87) Sysoev, V. V.; Button, B. K.; Wepsiec, K.; Dmitriev, S.; Kolmakov, A. Toward the Nanoscopic "Electronic Nose": Hydrogen vs Carbon Monoxide Discrimination with an Array of Individual Metal Oxide Nano- and Mesowire Sensors. *Nano Lett.* **2006**, *6*, 1584–1588.

(88) Mani, G. K.; Rayappan, J. B. B. Influence of Copper Doping on Structural, Optical and Sensing Properties of Spray Deposited Zinc Oxide Thin Films. *J. Alloys Compd.* **2014**, *582*, 414–419.

(89) Klingshirn, C.; Fallert, J.; Zhou, H.; Sartor, J.; Thiele, C.; Maier-Flaig, F.; Schneider, D.; Kalt, H. 65 Years of ZnO Research – Old and Very Recent Results. *Phys. Status Solidi B* **2010**, *247*, 1424–1447.

(90) Liu, C. M.; Liu, W. L.; Chen, W. J.; Hsieh, S. H.; Tsai, T. K.; Yang, L. C. ITO as a Diffusion Barrier Between Si and Cu. *J. Electrochem. Soc.* **2005**, *152*, G234–G239.

(91) Prenesti, E.; Daniele, P. G.; Toso, S. Visible Spectrophotometric Determination of Metal Ions: The Influence of Structure on Molar Absorptivity Value of copper(II) Complexes in Aqueous Solution. *Anal. Chim. Acta* **2002**, *459*, 323–336.

(92) Hathaway, B.; Duggan, M.; Murphy, A.; Mullane, J.; Power, C.; Walsh, A.; Walsh, B. The Stereochemistry and Electronic Properties of Fluxional Six-Coordinate copper(II) Complexes. *Coord. Chem. Rev.* **1981**, *36*, 267–324.

(93) Wen, S. J.; Couturier, G.; Campet, G.; Portier, J.; Claverie, J. Transport Properties of Copper-Doped Indium Oxide and Indium Tin Oxide Ceramics. *Phys. Status Solidi A* **1992**, *130*, 407–414.

(94) Ilavsky, J.; Jemian, P. R. Irena: Tool Suite for Modeling and Analysis of Small-Angle Scattering. *J. Appl. Crystallogr.* **2009**, *42*, 347–353.

(95) Schneider, C. A.; Rasband, W. S.; Eliceiri, K. W. NIH Image to ImageJ: 25 Years of Image Analysis. *Nat Meth* **2012**, *9*, 671–675.

Chapter V

(1) Dieringer, J. A.; Wustholz, K. L.; Masiello, D. J.; Camden, J. P.; Kleinman, S. L.; Schatz, G. C.; Van Duyne, R. P. Surface-Enhanced Raman Excitation Spectroscopy of a Single Rhodamine 6G Molecule. *J. Am. Chem. Soc.* **2009**, *131*, 849–854.

(2) Nie, S.; Emory, S. R. Probing Single Molecules and Single Nanoparticles by Surface-Enhanced Raman Scattering. *Science* **1997**, *275*, 1102–1106.

(3) Rosman, C.; Prasad, J.; Neiser, A.; Henkel, A.; Edgar, J.; Sönnichsen, C. Multiplexed Plasmon Sensor for Rapid Label-Free Analyte Detection. *Nano Lett.* **2013**, *13*, 3243–3247.

(4) Larsson, E. M.; Langhammer, C.; Zorić, I.; Kasemo, B. Nanoplasmonic Probes of Catalytic Reactions. *Science* **2009**, *326*, 1091–1094.

(5) Mendelsberg, R. J.; McBride, P. M.; Duong, J. T.; Bailey, M. J.; Llordes, A.; Milliron, D. J.; Helms, B. A. Dispersible Plasmonic Doped Metal Oxide Nanocrystal Sensors That Optically Track Redox Reactions in Aqueous Media with Single-Electron Sensitivity. *Adv. Opt. Mater.* **2015**, *3*, 1293–1300.

(6) Diroll, B. T.; Gordon, T. R.; Gaulding, E. A.; Klein, D. R.; Paik, T.; Yun, H. J.; Goodwin, E. D.; Damodhar, D.; Kagan, C. R.; Murray, C. B. Synthesis of N-Type Plasmonic Oxide Nanocrystals and the Optical and Electrical Characterization of Their Transparent Conducting Films. *Chem. Mater.* **2014**, *26*, 4579–4588.

(7) Ito, D.; Masuko, K.; Weintraub, B. A.; McKenzie, L. C.; Hutchison, J. E. Convenient Preparation of ITO Nanoparticles Inks for Transparent Conductive Thin Films. *J. Nanoparticle Res.* **2012**, *14*, 1–7.

(8) Loo, C.; Lowery, A.; Halas, N.; West, J.; Drezek, R. Immunotargeted Nanoshells for Integrated Cancer Imaging and Therapy. *Nano Lett.* **2005**, *5*, 709–711.

(9) Huang, X.; El-Sayed, I. H.; Qian, W.; El-Sayed, M. A. Cancer Cell Imaging and Photothermal Therapy in the Near-Infrared Region by Using Gold Nanorods. *J. Am. Chem. Soc.* **2006**, *128*, 2115–2120.

(10) Kumar, A.; Kim, S.; Nam, J.-M. Plasmonically Engineered Nanoprobes for Biomedical Applications. *J. Am. Chem. Soc.* **2016**, *138*, 14509–14525.

(11) Kovalenko, M. V.; Manna, L.; Cabot, A.; Hens, Z.; Talapin, D. V.; Kagan, C. R.; Klimov, V. I.; Rogach, A. L.; Reiss, P.; Milliron, D. J. Guyot-Sionnnest, P.; Konstantanos, G.; Parak, W. J.; Hyeon, T.; Korgel, B. A.; Murray, B. M.; Heiss, W. Prospects of Nanoscience with Nanocrystals. *ACS Nano* **2015**, *9*, 1012–1057.

(12) Faucheaux, J. A.; Stanton, A. L. D.; Jain, P. K. Plasmon Resonances of Semiconductor Nanocrystals: Physical Principles and New Opportunities. *J. Phys. Chem. Lett.* **2014**, *5*, 976–985.

(13) Lounis, S. D.; Runnerstrom, E. L.; Llordés, A.; Milliron, D. J. Defect Chemistry and Plasmon Physics of Colloidal Metal Oxide Nanocrystals. *J. Phys. Chem. Lett.* **2014**, *5*, 1564–1574.

(14) Agrawal, A.; Johns, R. W.; Milliron, D. J. Control of Localized Surface Plasmon Resonances in Metal Oxide Nanocrystals. *Annu. Rev. Mater. Res.* **2017**, *47*, in press.

(15) Kriegel, I.; Scotognella, F.; Manna, L. Plasmonic Doped Semiconductor Nanocrystals: Properties, Fabrication, Applications and Perspectives. *Plasmonic Doped Semicond. Nanocrystals Prop. Fabr. Appl. Perspect.* **2017**, *674*, 1–52.

(16) Kanehara, M.; Koike, H.; Yoshinaga, T.; Teranishi, T. Indium Tin Oxide Nanoparticles with Compositionally Tunable Surface Plasmon Resonance Frequencies in the Near-IR Region. *J. Am. Chem. Soc.* **2009**, *131*, 17736–17737.

(17) Gilstrap, R. A.; Capozzi, C. J.; Carson, C. G.; Gerhardt, R. A.; Summers, C. J. Synthesis of a Nonagglomerated Indium Tin Oxide Nanoparticle Dispersion. *Adv. Mater.* **2008**, *20*, 4163–4166.

(18) Choi, S.-I.; Nam, K. M.; Park, B. K.; Seo, W. S.; Park, J. T. Preparation and Optical Properties of Colloidal, Monodisperse, and Highly Crystalline ITO Nanoparticles. *Chem. Mater.* **2008**, *20*, 2609–2611.

(19) Farvid, S. S.; Dave, N.; Wang, T.; Radovanovic, P. V. Dopant-Induced Manipulation of the Growth and Structural Metastability of Colloidal Indium Oxide Nanocrystals. *J. Phys. Chem. C* **2009**, *113*, 15928–15933.

(20) Lee, J.; Lee, S.; Li, G.; Petruska, M. A.; Paine, D. C.; Sun, S. A Facile Solution-Phase Approach to Transparent and Conducting ITO Nanocrystal Assemblies. *J. Am. Chem. Soc.* **2012**, *134*, 13410–13414.

(21) Runnerstrom, E. L.; Bergerud, A.; Agrawal, A.; Johns, R. W.; Dahlman, C. J.; Singh, A.; Selbach, S. M.; Milliron, D. J. Defect Engineering in Plasmonic Metal Oxide Nanocrystals. *Nano Lett.* **2016**, *16*, 3390–3398.

(22) Mehra, S.; Bergerud, A.; Milliron, D. J.; Chan, E. M.; Salleo, A. Core/Shell Approach to Dopant Incorporation and Shape Control in Colloidal Zinc Oxide Nanorods. *Chem. Mater.* **2016**, *28*, 3454–3461.

(23) Garcia, G.; Buonsanti, R.; Runnerstrom, E. L.; Mendelsberg, R. J.; Llordes, A.; Anders, A.; Richardson, T. J.; Milliron, D. J. Dynamically Modulating the Surface Plasmon Resonance of Doped Semiconductor Nanocrystals. *Nano Lett.* **2011**, *11*, 4415–4420.

(24) Della Gaspera, E.; Chesman, A. S. R.; van Embden, J.; Jasieniak, J. J. Non-Injection Synthesis of Doped Zinc Oxide Plasmonic Nanocrystals. *ACS Nano* **2014**, *8*, 9154–9163.

(25) Gordon, T. R.; Paik, T.; Klein, D. R.; Naik, G. V.; Caglayan, H.; Boltasseva, A.; Murray, C. B. Shape-Dependent Plasmonic Response and Directed Self-Assembly in a New Semiconductor Building Block, Indium-Doped Cadmium Oxide (ICO). *Nano Lett.* **2013**, *13*, 2857–2863.

(26) Ye, X.; Reifsnyder Hickey, D.; Fei, J.; Diroll, B. T.; Paik, T.; Chen, J.; Murray, C. B. Seeded Growth of Metal-Doped Plasmonic Oxide Heterodimer Nanocrystals and Their Chemical Transformation. *J. Am. Chem. Soc.* **2014**, *136*, 5106–5115.

(27) De Trizio, L.; Buonsanti, R.; Schimpf, A. M.; Llordes, A.; Gamelin, D. R.; Simonutti, R.; Milliron, D. J. Nb-Doped Colloidal TiO_2 Nanocrystals with Tunable Infrared Absorption. *Chem. Mater.* **2013**, *25*, 3383–3390.

(28) Fang, H.; Hegde, M.; Yin, P.; Radovanovic, P. V. Tuning Plasmon Resonance of In_2O_3 Nanocrystals throughout the Mid-Infrared Region by Competition between Electron Activation and Trapping. *Chem. Mater.* **2017**, *29*, 4970-4979.

(29) Buonsanti, R.; Milliron, D. J. Chemistry of Doped Colloidal Nanocrystals. *Chem. Mater.* **2013**, *25*, 1305–1317.

(30) Johns, R. W.; Bechtel, H. A.; Runnerstrom, E. L.; Agrawal, A.; Lounis, S. D.; Milliron, D. J. Direct Observation of Narrow Mid-Infrared Plasmon Linewidths of Single Metal Oxide Nanocrystals. *Nat. Commun.* **2016**, *7*, 11583.

(31) Lounis, S. D.; Runnerstrom, E. L.; Bergerud, A.; Nordlund, D.; Milliron, D. J. Influence of Dopant Distribution on the Plasmonic Properties of Indium Tin Oxide Nanocrystals. *J. Am. Chem. Soc.* **2014**, *136*, 7110–7116.

(32) Ito, D.; Yokoyama, S.; Zaikova, T.; Masuko, K.; Hutchison, J. E. Synthesis of Ligand-Stabilized Metal Oxide Nanocrystals and Epitaxial Core/Shell Nanocrystals *via* a Lower-Temperature Esterification Process. *ACS Nano* **2014**, *8*, 64–75.

(33) Jansons, A. W.; Hutchison, J. E. Continuous Growth of Metal Oxide Nanocrystals: Enhanced Control of Nanocrystal Size and Radial Dopant Distribution. *ACS Nano* **2016**, *10*, 6942–6951.

(34) Jansons, A. W.; Plummer, L. K.; Hutchison, J. E. Living Nanocrystals. *Chem. Mater.* **2017**, *29*, *ASAP*.

(35) Tanuma, S.; Powell, C. J.; Penn, D. R. Calculations of Electron Inelastic Mean Free Paths. V. Data for 14 Organic Compounds over the 50–2000 eV Range. *Surf. Interface Anal.* **1994**, *21*, 165–176.

(36) Veamatahau, A.; Jiang, B.; Seifert, T.; Makuta, S.; Latham, K.; Kanehara, M.; Teranishi, T.; Tachibana, Y. Origin of Surface Trap States in CdS Quantum Dots: Relationship between Size Dependent Photoluminescence and Sulfur Vacancy Trap States. *Phys. Chem. Chem. Phys.* **2015**, *17*, 2850–2858.

(37) Oh, S. J.; Straus, D. B.; Zhao, T.; Choi, J.-H.; Lee, S.-W.; Gaulding, E. A.; Murray, C. B.; Kagan, C. R. Engineering the Surface Chemistry of Lead Chalcogenide Nanocrystal Solids to Enhance Carrier Mobility and Lifetime in Optoelectronic Devices. *Chem. Commun.* **2017**, *53*, 728–731.

(38) Houtepen, A. J.; Hens, Z.; Owen, J. S.; Infante, I. On the Origin of Surface Traps in Colloidal II–VI Semiconductor Nanocrystals. *Chem. Mater.* **2017**, *29*, 752–761.

(39) Boles, M. A.; Ling, D.; Hyeon, T.; Talapin, D. V. The Surface Science of Nanocrystals. *Nat Mater* **2016**, *15*, 141–153.

(40) Scotognella, F.; Della Valle, G.; Srimath Kandada, A. R.; Dorfs, D.; Zavelani-Rossi, M.; Conforti, M.; Miszta, K.; Comin, A.; Korobchevskaya, K.; Lanzani, G.; Manna, L.; Tassone, F. Plasmon Dynamics in Colloidal Cu_2–xSe Nanocrystals. *Nano Lett.* **2011**, *11*, 4711–4717.

(41) Dorfs, D.; Härtling, T.; Miszta, K.; Bigall, N. C.; Kim, M. R.; Genovese, A.; Falqui, A.; Povia, M.; Manna, L. Reversible Tunability of the Near-Infrared Valence Band Plasmon Resonance in Cu_2–xSe Nanocrystals. *J. Am. Chem. Soc.* **2011**, *133*, 11175–11180.

(42) Manthiram, K.; Alivisatos, A. P. Tunable Localized Surface Plasmon Resonances in Tungsten Oxide Nanocrystals. *J. Am. Chem. Soc.* **2012**, *134*, 3995–3998.

(43) Hamberg, I.; Granqvist, C. G. Evaporated Sn-doped In_2O_3 Films: Basic Optical Properties and Applications to Energy-efficient Windows. *J. Appl. Phys.* **1986**, *60*, R123–R160.

(44) Hamberg, I.; Granqvist, C. G. Optical Properties of Transparent and Heat-reflecting Indium Tin Oxide Films: The Role of Ionized Impurity Scattering. *Appl. Phys. Lett.* **1984**, *44*, 721–723.

(45) Agrawal, A.; Singh, A.; Yazdi, S.; Singh, A.; Ong, G. K.; Bustillo, K.; Johns, R. W.; Ringe, E.; Milliron, D. J. Resonant Coupling between Molecular Vibrations and Localized Surface Plasmon Resonance of Faceted Metal Oxide Nanocrystals. *Nano Lett.* **2017**, *17*, 2611–2620.

(46) Link, S.; El-Sayed, M. A. Spectral Properties and Relaxation Dynamics of Surface Plasmon Electronic Oscillations in Gold and Silver Nanodots and Nanorods. *J. Phys. Chem. B* **1999**, *103*, 8410–8426.

(47) Fan, J. C. C.; Goodenough, J. B. X-ray Photoemission Spectroscopy Studies of Sn-doped Indium-oxide Films. *J. Appl. Phys.* **1977**, *48*, 3524–3531.

(48) Frank, G.; Köstlin, H. Electrical Properties and Defect Model of Tin-Doped Indium Oxide Layers. *Appl. Phys. A* **1982**, *27*, 197–206.

(49) Cox, P. A.; Flavell, W. R.; Egdell, R. G. Solid-State and Surface Chemistry of Sn-Doped In2O3 Ceramics. *J. Solid State Chem.* **1987**, *68*, 340–350.

(50) Gassenbauer, Y.; Schafranek, R.; Klein, A.; Zafeiratos, S.; Hävecker, M.; Knop-Gericke, A.; Schlögl, R. Surface States, Surface Potentials, and Segregation at Surfaces of Tin-Doped In_2O_3. *Phys. Rev. B* **2006**, *73*, 245312.

(51) Liu, N.; Tang, M. L.; Hentschel, M.; Giessen, H.; Alivisatos, A. P. Nanoantenna-Enhanced Gas Sensing in a Single Tailored Nanofocus. *Nat Mater* **2011**, *10*, 631–636.

(52) Willets, K. A.; Duyne, R. P. V. Localized Surface Plasmon Resonance Spectroscopy and Sensing. *Annu. Rev. Phys. Chem.* **2007**, *58*, 267–297.

(53) Elghanian, R.; Storhoff, J. J.; Mucic, R. C.; Letsinger, R. L.; Mirkin, C. A. Selective Colorimetric Detection of Polynucleotides Based on the Distance-Dependent Optical Properties of Gold Nanoparticles. *Science* **1997**, *277*, 1078–1081.

(54) Llordes, A.; Garcia, G.; Gazquez, J.; Milliron, D. J. Tunable near-Infrared and Visible-Light Transmittance in Nanocrystal-in-Glass Composites. *Nature* **2013**, *500*, 323–326.

(55) Llordes, A.; Wang, Y.; Fernandez-Martinez, A.; Xiao, P.; Lee, T.; Poulain, A.; Zandi, O.; Saez Cabezas, C. A.; Henkelman, G.; Milliron, D. J. Linear Topology in Amorphous Metal Oxide Electrochromic Networks Obtained *via* Low-Temperature Solution Processing. *Nat Mater* **2016**, *15*, 1267–1273.

(56) Garcia, G.; Buonsanti, R.; Llordes, A.; Runnerstrom, E. L.; Bergerud, A.; Milliron, D. J. Near-Infrared Spectrally Selective Plasmonic Electrochromic Thin Films. *Adv. Opt. Mater.* **2013**, *1*, 215–220.

(57) Ilavsky, J.; Jemian, P. R. Irena: Tool Suite for Modeling and Analysis of Small-Angle Scattering. *J. Appl. Crystallogr.* **2009**, *42*, 347–353.

Chapter VI

(1) Morris-Cohen, A. J.; Malicki, M.; Peterson, M. D.; Slavin, J. W. J.; Weiss, E. A. Chemical, Structural, and Quantitative Analysis of the Ligand Shells of Colloidal Quantum Dots. *Chem. Mater.* **2013**, *25*, 1155–1165.

(2) Holmberg, V. C.; Helps, J. R.; Mkhoyan, K. A.; Norris, D. J. Imaging Impurities in Semiconductor Nanostructures. *Chem. Mater.* **2013**, *25*, 1332–1350.

(3) Sowers, K. L.; Swartz, B.; Krauss, T. D. Chemical Mechanisms of Semiconductor Nanocrystal Synthesis. *Chem. Mater.* **2013**, *25*, 1351–1362.

(4) Li, T.; Senesi, A. J.; Lee, B. Small Angle X-Ray Scattering for Nanoparticle Research. *Chem. Rev.* **2016**, *116*, 11128–11180.

(5) Newton, M. A.; Chapman, K. W.; Thompsett, D.; Chupas, P. J. Chasing Changing Nanoparticles with Time-Resolved Pair Distribution Function Methods. *J. Am. Chem. Soc.* **2012**, *134*, 5036–5039.

(6) Jensen, K. M. Ø.; Christensen, M.; Juhas, P.; Tyrsted, C.; Bøjesen, E. D.; Lock, N.; Billinge, S. J. L.; Iversen, B. B. Revealing the Mechanisms behind Sn_{O2} Nanoparticle Formation and Growth during Hydrothermal Synthesis: An In Situ Total Scattering Study. *J. Am. Chem. Soc.* **2012**, *134*, 6785–6792.

(7) Jensen, K. M. Ø.; Andersen, H. L.; Tyrsted, C.; Bøjesen, E. D.; Dippel, A.-C.; Lock, N.; Billinge, S. J. L.; Iversen, B. B.; Christensen, M. Mechanisms for Iron Oxide Formation under Hydrothermal Conditions: An in Situ Total Scattering Study. *ACS Nano* **2014**, *8*, 10704–10714.

(8) Tamang, S.; Lee, S.; Choi, H.; Jeong, S. Tuning Size and Size Distribution of Colloidal InAs Nanocrystals via Continuous Supply of Prenucleation Clusters on Nanocrystal Seeds. *Chem. Mater.* **2016**, *28*, 8119–8122.

(9) Battaglia, D.; Peng, X. Formation of High Quality InP and InAs Nanocrystals in a Noncoordinating Solvent. *Nano Lett.* **2002**, *2*, 1027–1030.

(10) Tamang, S.; Lincheneau, C.; Hermans, Y.; Jeong, S.; Reiss, P. Chemistry of InP Nanocrystal Syntheses. *Chem. Mater.* **2016**, *28*, 2491–2506.

Appendix B

(1) Zai, J., Zhu, J., Qi, R. & Qian, X. Nearly monodispersed $In(OH)_3$ hierarchical nanospheres and nanocubes: tunable ligand-assisted synthesis and their conversion into hierarchical In_2O_3 for gas sensing. *J. Mater. Chem. A* **1,** 735–745 (2013).

(2) Lin, A. W. C., Armstrong, N. R. & Kuwana, T. X-ray photoelectron/Auger electron spectroscopic studies of tin and indium metal foils and oxides. *Anal. Chem.* **49,** 1228–1235 (1977).

(3) Kim, M.-G., Kanatzidis, M. G., Facchetti, A. & Marks, T. J. Low-temperature fabrication of high-performance metal oxide thin-film electronics via combustion processing. *Nat Mater* **10,** 382–388 (2011).

(4) Berthold, T. *et al.* Consequences of plasma oxidation and vacuum annealing on the chemical properties and electron accumulation of In_2O_3 surfaces. *J. Appl. Phys.* **120,** 245301 (2016).

(5) Fan, J. C. C. & Goodenough, J. B. X-ray photoemission spectroscopy studies of Sn-doped indium-oxide films. *J. Appl. Phys.* **48,** 3524–3531 (1977).

(6) Roisnel, T. & Rodríquez-Carvajal, J. WinPLOTR: a windows tool for powder diffraction pattern analysis. in *Materials Science Forum* **378,** 118–123 (Transtec Publications; 1999, 2001).